

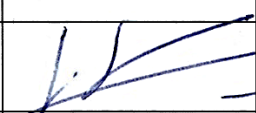
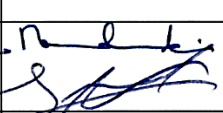
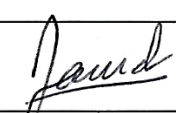
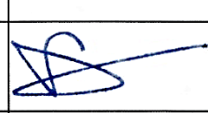
FREE DISTRIBUTION

Technical Report RT/DEHT/2016-137

MEGASTACK: D2.3
Functional and validated multi-scale and multi-phase models for PEMwater electrolyzer

Authors: G. Serre, M. Chandesris, F. Fouda-Onana, D. Brun-Buisson (CEA)
P. Skjetne, T. Bergstrøm (SINTEF)
K. Bromberger, T. Smolinka, J. Ghinaiya (FRAUNHOFER)

Project reference	13.04383
Project title	MEGASTACK
Period of the project	01/10/2014 – 31/09/2017
Nature of the report	<input type="checkbox"/> Progress Report <input type="checkbox"/> Final Report <input type="checkbox"/> Contribution to a global report <input checked="" type="checkbox"/> Work package report (WP) <input type="checkbox"/> Others : <i>specify the nature of the report</i> (ex : non included on the agreement, training report)
Appendices (to complete inevitably for « Restricted Distribution)	<input checked="" type="checkbox"/> YES <input type="checkbox"/> NO If the report include appendices, specify : Appendices XX from page XXX to page XXX

	Writer(s)	Controller	Approver	Transmitter
Name(s)	G. SERRE	M. CHANDESRIS M. GERARD	D. JAMET	S. JOUANNEAU SI LARBI
Position	Research engineer	Project Leader Head of Laboratory	Head of Service	Head of Department
Signatures				
Date	16/12/2016	16/12/2016	16/12/2016	19/12/2016.

Commissariat à l'énergie atomique et aux énergies alternatives

T. | F.

Direction de la Recherche Technologique
Département : DEHT
Service : SAMA
Laboratoire : LMP

FREE DISTRIBUTION

FOLLOW-UP OF THE REVISIONS

Index	Date	Cause and description of the modification
A	2016	Initial Document

FREE DISTRIBUTION

DISTRIBUTION LIST

CUSTOMER	P. SKJETNE, M. THOMASSEN, A. OYARCE BARNETT, T. BERGSTRØM (SINTEF)	1 ex. (email)
	K. BROMBERGER, T. SMOLINKA (FRAUNHOFER)	1 ex. (email)
	B. GREEN, F. A. L. MARCHAL (ITM-Power)	1 ex. (email)
LITEN	F. LAMBERT	1 ex. (email)
	P. DUSSOUILLEZ	1 ex. (email)
	L. ANTONI	1 ex. (email)
	T. PRIEM	1 ex. (email)
	J. MOUGIN	1 ex. (email)
	J-L. SIX	1 ex. (email)
	Financial Office	1 ex. (email)
DEPARTMENT DEHT	S. JOUANNEAU SI LARBI	1 ex. (email)
	S. MAILLEY	1 ex. (email)
	N. JOUAS	1 ex (paper)
SERVICE AND LABORATORY SAMA	D. JAMET	1 ex. (email)
	M. CHANDESRIS	1 ex. (email)
	M. GERARD	1 ex. (email)
	P. SCHOTT	1 ex. (email)
	G. SERRE	1 ex. (email)
	D. BRUN-BUISSON	1 ex. (email)
STP	L. DANIEL	1 ex. (email)
	F. FOU DA ONANA	1 ex. (email)
	P.-A. JACQUES	1 ex. (email)
	E. PINTON	1 ex. (email)
	S. ROSINI	1 ex. (email)
DTBH/SCSH/LEED	F. MICOUD	1 ex. (email)
	C. BOURASSEAU	1 ex. (email)

FREE DISTRIBUTION

RULES FOR DOCUMENT MANAGEMENT AND CONFIDENTIALITY::

Based on the privacy statement shown at the top of the page, this document must be managed according to the guidelines described below.

FREE DISTRIBUTION: This document may be distributed to other third parties as the contractors. It must be distributed unchanged and in its entirety and include the issuer's attribution and credit. This corresponds to the type of licence



defined by <http://creativecommons.org/licenses/>. However, recipients are requested to exercise sound judgement when redistributing the document.

FREE DISTRIBUTION

Table of contents

1.	INTRODUCTION.....	8
2.	MATERIAL PROPERTIES.....	8
	2.1 MESH.....	8
	2.1.1 Geometrical properties.....	8
	2.1.2 Through plane permeability (summary in Table 3).....	9
	2.1.3 Electrical properties.....	13
	2.1.4 Thermal properties.....	13
	2.2 SINTERS.....	14
	2.2.1 Roughness.....	14
	2.2.2 Porosity and pore size distribution.....	15
	2.2.3 Permeability.....	21
	2.2.4 Capillarity.....	30
	2.2.5 Contact angle.....	33
	2.2.6 Electrical conductivity – contact resistances.....	35
3.	ELECTROCHEMICAL MEASUREMENTS	41
	3.1 EXPERIMENTS PERFORMED AT CEA	41
	3.1.1 Cell description and measurements	41
	3.1.2 Water flow balance.....	42
	3.1.3 PEIS measurements	44
	3.1.4 Polarization curves.....	46
	3.2 EXPERIMENTS PERFORMED AT FRAUNHOFER	48
	3.2.1 Cell and test bench description	48
	3.2.2 Polarization curves.....	50
4.	ELEMENTARY PHYSICAL AND ELECTROCHEMICAL LAWS	53
	4.1 CAPILLARY PRESSURE MODEL.....	53
	4.1.1 General approach for modelling	53
	4.1.2 Capillary pressure model based on Porefil results.....	53
	4.1.3 Using water results.....	55
	4.2 WATER PERMEATION THROUGH THE MEMBRANE.....	56
	4.3 OHMIC RESISTANCE	58
	4.4 ELECTROCHEMICAL LAW.....	59
	4.4.1 Reversible potential.....	60
	4.4.2 Overpotential determination	61
	4.4.3 Overpotential modelling.....	62
	4.4.4 The pressure effect in the electrochemical law.....	67
5.	CHANNEL/MESH FLOW MODELLING AND SIMULATION	68

FREE DISTRIBUTION

5.1	LAB-SCALE TWO-PHASE FLOW CHANNEL MODEL	68
5.2	CELL SCALE SINGLE-PHASE STUDY	70
	<i>5.2.1 Geometry and grid ITM model description.....</i>	<i>70</i>
	<i>5.2.2 ITM Mesh configuration.....</i>	<i>71</i>
	<i>5.2.3 Flow simulation results.....</i>	<i>72</i>
6.	VALIDATION OF THE STACK-SCALE CEA MODEL.....	74
	6.1 INTRODUCTION	74
	6.2 VALIDATION AGAINST POLARIZATION CURVES	75
	6.3 LINK BETWEEN THE LIQUID SATURATION AND THE POTENTIAL.....	76
	6.4 SPATIAL EVOLUTIONS	77
7.	CONCLUSION.....	81
8.	NOMENCLATURE.....	83
9.	REFERENCES.....	84
10.	APPENDIX: LINK BETWEEN PERMEABILITY AND HYDRAULIC DIAMETER.....	85

FREE DISTRIBUTION

Summary

The main objective of the European project MEGASTACK is to develop a cost efficient stack design for Megawatt sized PEM electrolyzer and to construct and demonstrate a prototype of this stack. In the approach proposed to reach this objective, an important task is the development and use of multi-scale and multi-physics models.

The predictability of such models relies on their validity. To that end, the key components of ITM's stack (mesh, sinter and MEA) have been characterized, both ex-situ and in-situ, to analyze their physical properties. These experimental data are then used to develop several physical and electrochemical laws needed in the modelling tool which simulates the electrolyzer's performance.

The first results obtained using the simulation tools developed during the project and the validation of these results versus the experimental data are described in this report.

FREE DISTRIBUTION

1. INTRODUCTION

The main objective of the European project MEGASTACK is to develop a cost efficient stack design for Megawatt sized PEM electrolyzer. In the integrated approach proposed to achieve this objective, one of the key tasks is the development and subsequent use of multiscale and multi-physic models. The validity of such models relies on the physical laws and material properties that are provided as input parameters to the models, and also on the validation of the final model.

The stack model that will serve as an engineering tool to answer design questions has been presented in deliverable D2.2. The objective of this document is to present the different experimental techniques that have been used to determine the physical properties of the cell and stack key components and also the validation of the multi-physic stack model.

The key components of ITM's stack that have been studied are the fluid distributors, the membrane electrode assembly, and the porous transport layers (PTL). These components have been firstly characterized ex-situ (section 2) and then in-situ (section 3) at CEA, SINTEF and Fraunhofer using various experimental techniques. From these experimental results elementary physical and electrochemical laws have been developed and validated individually (section 0). In parallel, a strong effort has been devoted to the analysis of the two-phase water flow on the anode side. The flow behavior depends on the anodic distributor design, on the mesh properties and also on the nature of the flow (one-phase vs. two-phase). It has been analyzed in details at SINTEF using both two-phase flow experiments and dedicated CFD simulation tools (section 5). Finally, the physical properties and laws determined in the previous sections are implemented in the stack code developed at CEA (called PS++ code) (see D2.2) in order to validate the coupled multi-physic model and estimate its ability to predict PEMWE performance for various operating conditions (section 0).

2. MATERIAL PROPERTIES

The objective of this section is to determine ex-situ the physical properties of the fluid distributor and the PTL

2.1 Mesh

The meshes used as fluid distributor are made of titanium. Their function is to supply water, remove the produced gas, conduct electricity and transfer heat. Their main properties (geometry, electric conductivity, thermic conductivity, permeability) are given here.

2.1.1 Geometrical properties

FREE DISTRIBUTION

Mesh dimensions

Two techniques have been used to estimate the dimensions of the mesh: a caliper and measurements from picture using the free software *the Gimp*.

Dimensions that were determined were the thickness, diameter, wire thickness and the length and with of the open areas in the mesh.

Mesh porosity

The porosity is estimated using the measured mass and volume of the sample and also the known titanium density:

Mass	3.01g
Mesh volume	$V = 3.1416 \times 55.5^2 / 4 \times 0.9 = 2177.3 \text{ mm}^3$.
Mesh density	$3.01 / 2177.3 = 1.38 \cdot 10^{-3} \text{ g/mm}^3$.
Titanium density	$4.51 \cdot 10^{-3} \text{ g/mm}^3$ (Wikipedia).
Mesh porosity	$1 - \text{Mesh density} / \text{Titanium density} = 69.3\%$

Table 1: Mesh porosity

2.1.2 Through plane permeability (summary in Table 3)

Using a zoomed and contrasted picture of the mesh (such as the picture in the middle on the Figure 2) in *the Gimp* software, it is possible to obtain the number of white pixels and then of black ones. The ratio of white to black+white pixels gives the relative available section for the through plane flow.

The hydraulic diameter is calculated as the ratio of the white surface to its (internal) black perimeter using the right pictures on Figure 2. This calculation is performed using *the Gimp*.

An order of magnitude of the through plane permeability is given by the following formula (see demonstration §10 p85):

$$K \sim \frac{D_H^2}{32}$$

The TP permeability of the mesh was measured at Fraunhofer using capillary flow porometry (CFP) device from Porolux for samples with a diameter of 11.95 mm. Nitrogen gas was supplied from one side of the mesh. The pressure and flow rate of gas were measured before the mesh. The acquired result of TP gas permeability can be seen in Figure 3.

The Darcy's law writes:

$$\frac{\Delta P}{L} = -\frac{\mu}{K} V$$

To use this law, the measured pressure vs. gas flow rate should be a straight line (constant gas permeability). However, here measured pressured vs. gas flow rate is not a straight line and that leads to a different TP permeability at different pressures vs. flow rates. One more

FREE DISTRIBUTION

point to be considered while measuring TP gas permeability with the Porolux is the pressure after the mesh at the outlet. For the measurement of gas permeability using Porolux, it is assumed that the outlet pressure (pressure after the sample) is atmospheric. This can be applied satisfactorily to samples that have lower porosity and permeability, where the outlet pressure is nearly atmospheric conditions. In the case of a mesh, however, the gas flow rate is quite higher and goes through the mesh without much pressure drop. Therefore, there must be a certain pressure drop at the outlet manifolds, which is not negligible for the TP permeability measurements. All in all, it is expected that real TP permeability of mesh must be higher than the here measured ($K= 2.0 \cdot 10^{-11} \text{ m}^2$, inertial coefficient is $1.30 \cdot 10^{-5} \text{ m}$).

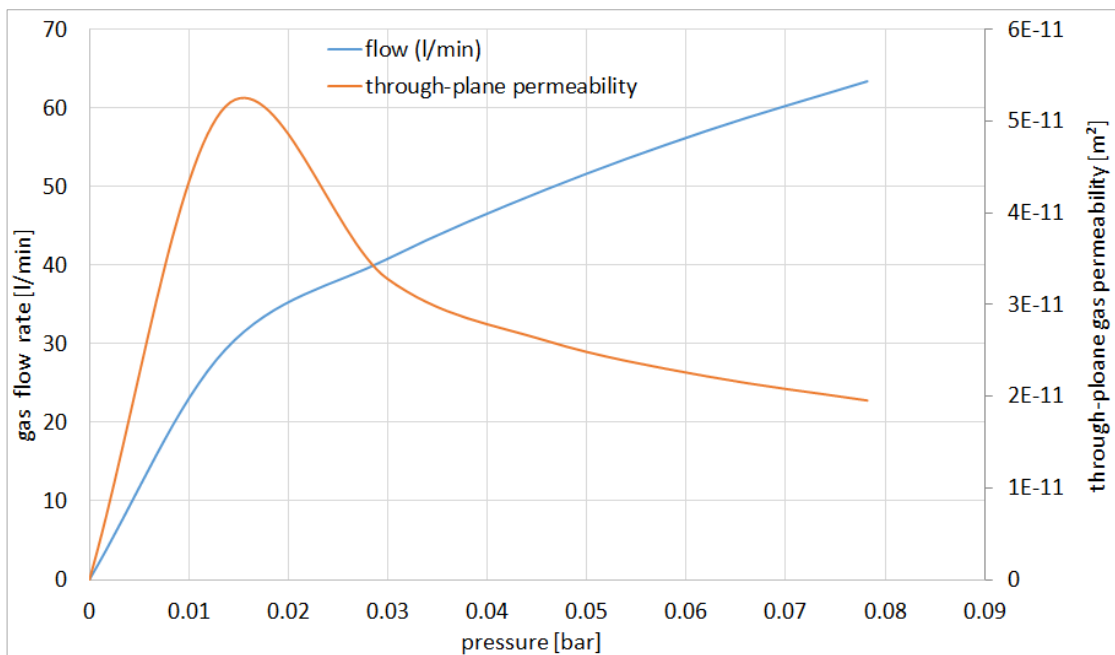


Figure 1: Result of measured TP gas permeability of the mesh using the Porolux device

relative opened section	71.2%
Wetted perimeter	143 (+/-2) pixels
Surface	1444 pixels ²
Hydraulic diameter	$Dh=4xS/Pw = 40.4 \text{ pixels} \rightarrow Dh=1.35\text{mm} \pm 0.01\text{mm}$
Permeability (picture)	$5.7 \cdot 10^{-8} \text{ m}^2$
Permeability (porometry)	$K= 2.0 \cdot 10^{-11} \text{ m}^2$, inertial coefficient: $1.30 \cdot 10^{-5} \text{ m}$

Table 2: Mesh through plane properties

In plane permeability (summary in Table 4)

It is very difficult to estimate the in-plane (IP) porosity from the current geometrical data. As a first rough estimation, we consider the mesh situated in between 2 parallel plates. The distance between the plates corresponds to the mesh thickness (0.9 mm) and since a fiber thickness is about 0.7mm, the remaining surface for fluid flow is $H=0.9-0.7=0.2\text{mm}$ multiplied by the width of the mesh (W).

FREE DISTRIBUTION

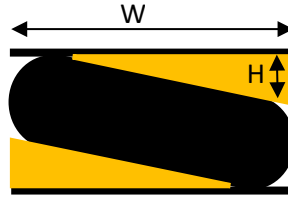


Figure 2: In plane mesh scheme to estimate the IP porosity

Thus the open surface for the fluid is:

$$S = H W$$

and the wetted perimeter is:

$$P_w = 2 (H+W) \sim 2W$$

since $H \ll W$. Thus, the hydraulic diameter is estimated as:

$$D_h \sim 4 S / P_w \sim 2 H = 0.2 \text{ mm.}$$

Since the mesh is compressed, we estimate that:

$$0.1 < D_h \text{ (mm)} < 0.2.$$

Thus, the in plane permeability is then estimated:

$$3.1 \cdot 10^{-10} < K_{ip} \text{ (m}^2\text{)} < 1.3 \cdot 10^{-9}$$

The in plane (IP) permeability of the mesh has been determined using a purpose-made permeability measurement cell at Fraunhofer ISE. For these IP measurements, the mesh sample is 49.7 mm * 49.7 mm. The orientation can be taken from Figure 5.

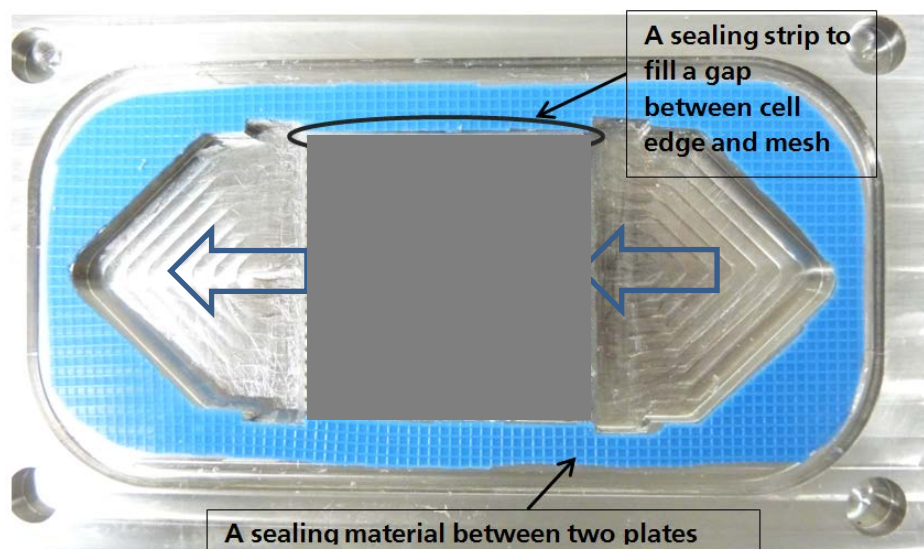


Figure 3: View on top of the open cell assembly with mesh to measure the in plane permeability

Figure 5 shows the open assembly of the purpose-made IP cell with one mesh. For the conducted mesh test, no sealing material was used except a small sealing strip as shown in Figure 5. A clamping force up to 4.8 kN was applied to avoid interfacial bypasses between

FREE DISTRIBUTION

mesh and contacting surfaces. For the gas supply the IP permeability test cell was connected to the Porometer since this CFP device is capable to deliver a wide range (1 ml/min to 200 l/min) of flow rate with high accuracy. Nitrogen gas was supplied from one side of mesh as indicated in Figure 5. Subsequently, gas flow rate and pressure difference across the mesh were measured. Results can be seen in Figure 6. Darcy-Forchheimer law was used to calculate the permeability and corresponding inertial coefficient.

The law writes:

$$\frac{\Delta P}{L} = - \frac{\mu}{K} V - \frac{\rho}{C} V^2$$

Permeability K and inertial coefficient C are determined from fitting and those are $1.22 \cdot 10^{-9} \text{ m}^2$ and $2.0 \cdot 10^{-2} \text{ m}$ respectively. The experimentally measured permeability at FhG has a very similar order of magnitude than the value estimated by CEA even it is slightly lower.

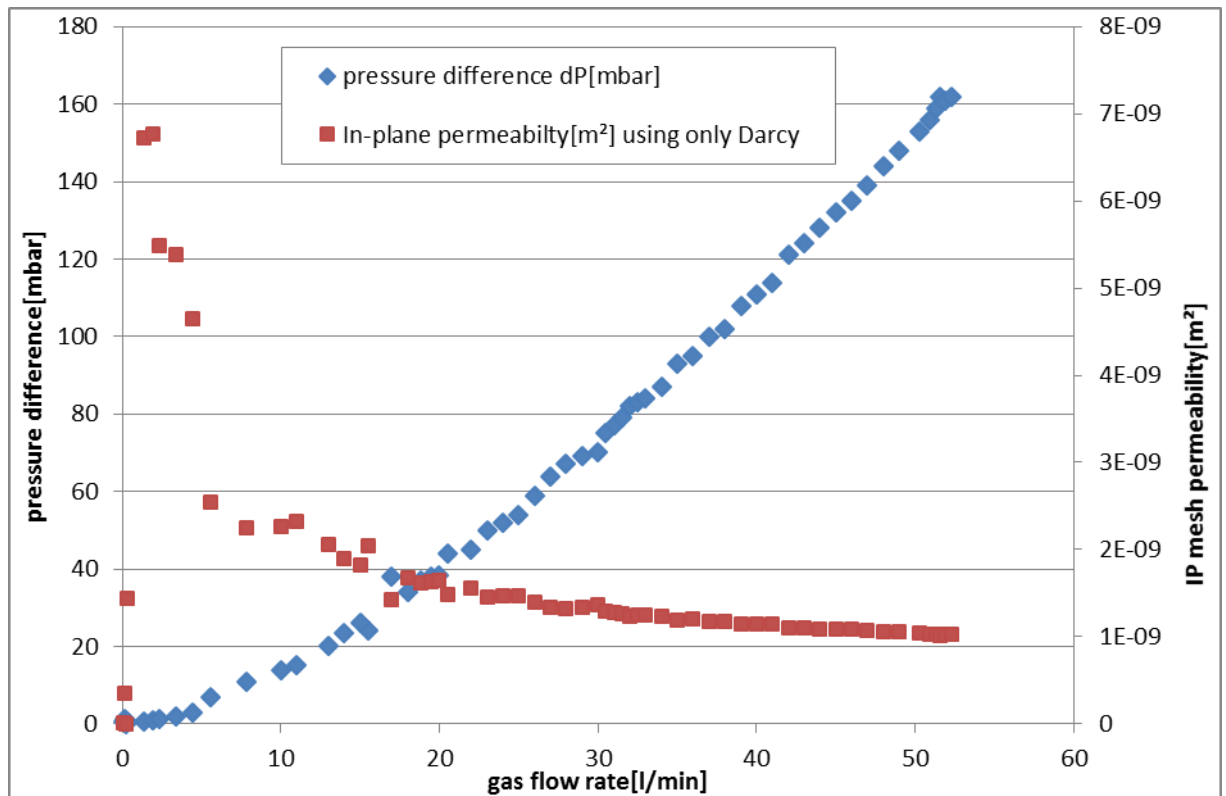


Figure 4: Result of in plane gas permeability measurements for the mesh

Hydraulic diameter (picture)	0.2mm (0.1mm if compressed ?)
Permeability (picture)	$3,1 \cdot 10^{-10} < K_{ip} \text{ (m}^2\text{)} < 1,3 \cdot 10^{-9}$
Permeability (porometry)	$K= 1.22 \cdot 10^{-9} \text{ m}^2$, inertial coefficient: $2.0 \cdot 10^{-2} \text{ m}$

Table 3: Mesh in plane properties

FREE DISTRIBUTION

2.1.3 Electrical properties

The electrical resistance of one mesh and a combination of two meshes in various orientations (see Figure 7) have been measured as function of the clamping pressure at CEA (see Figure 8). The grid stack was placed in between two Copper made electrodes and the current was applied with a chronopotentiometry method. The voltage was measured with two others cables on the same electrode and the resistance was accordingly calculated. The pressure was manually adjusted to reach the desired clamping pressure.

The resistance of two meshes stacked in parallel orientation is slightly higher than for two meshes stacked in perpendicular orientation.

Overlaid Meshes configuration



Crossed Meshes configuration

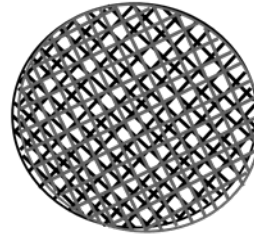


Figure 5: Different orientations of two stacked meshes. In this report, the crossed mesh configuration is denoted as “perpendicular” (P).

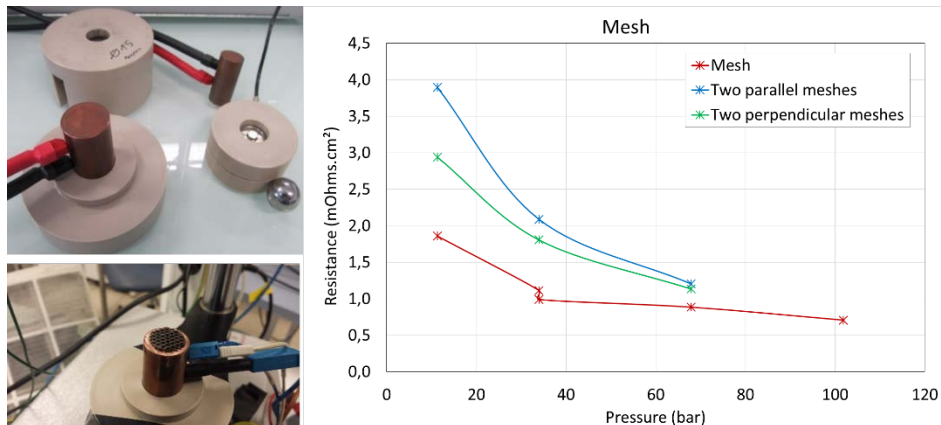


Figure 6: Electrical resistance (in plane) of the meshes

- a) Photo of the experimental set up
- b) Effect of stack grids configuration on the contact resistance

2.1.4 Thermal properties

The meshes are expected to have a good thermal conductivity and, since no experiment has been performed, an order of magnitude will use in the code: the value of the bulk Titanium conductivity: 21.9 W/m/K.

FREE DISTRIBUTION

2.2 Sinters

The porous transport layers (PTL) are located between the meshes and the catalyst coated membrane CCM (see Figure 1). Their function is to supply water, remove the produced gas, conduct electricity and transfer heat. Therefore it is necessary to characterize them, in particular their following properties: geometry, capillarity and permeability, electric conductivity and thermic conductivity. These characterizations have been performed on 4 different PTL types provided by ITM (see the table below). These 4 sinters are made from the same material but their surface treatments and coatings are different.

	Sinter 1	Sinter 2	Sinter 3	Sinter 4
Treatment and coating	no treatment	treated by oxalic acid	Pt-coating method A	Pt-coating method B
	ITM-01 	ITM-02 	ITM-03 	ITM-04 

Table 4: the 4 sinters provided by ITM

2.2.1 Roughness

The surface roughness of the sinters were measured by White Light Interferometry (WLI). WLI interferometry is a non-contact optical method for surface height measurement on 3-D structures with surface profiles varying between tens of nanometers and a few centimeters. A white light interferometer is essentially an optical microscope with a parallel mirror interferometer below the objective lens (see Figure 9). Light rays from the lamp are split at the lower mirror, some reaching the sample while others bounce between the mirrors. The rays recombine and will interfere on their way to the camera. The interference is used to determine when a point on the sample is in exact focus, since the instrument is adjusted to give maximum constructive interference at best focus. By scanning the lens towards the surface, the height of all pixels in the image can be determined with high precision, provided that enough light is reflected back into the lens from that point. This technique has a depth resolution of about 3 nm, and accuracy after calibration better than 10 nm over a 10 μm step, i.e. under 0.1%. A WYKO™ NT-2000 white light interferometer from Veeco Instruments Inc. (Arizona, USA) was used in this study

FREE DISTRIBUTION

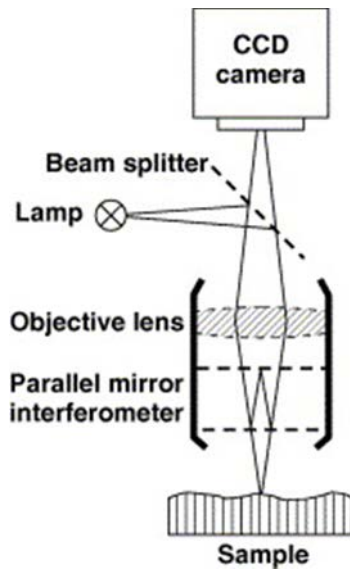


Figure 7: White Light Interferometry.

A topographic visualization of the surface roughness of the four sinters in an area of 1x1 mm² are shown in the Figure 10. The particle and pore size of the sinter close to the surface can also be seen in the figure. Taking the root mean square (RMS) of the height profile gives a representation of the overall surface roughness of the different sinters. The RMS is calculated over the entire measured array according to the following equation:

R_q

The root-mean-squared roughness calculated over the entire measured array.

$$R_q = \sqrt{\frac{1}{n} \sum_{i=1}^n (Z_i - \bar{Z})^2}$$

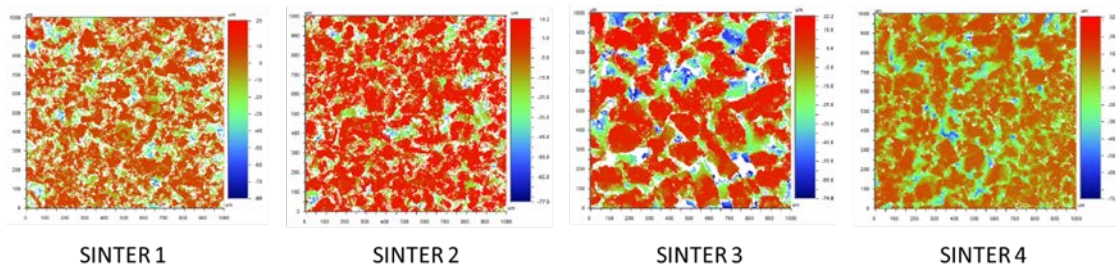


Figure 8: surface roughness of the four sinters.

As shown in Table 6 and also looking at figure 10, the sinters 1, 2 and 4 have very similar overall roughness, particle size and the pore size on the surface of the sinter, while sinter 3 clearly differentiates itself with a significantly higher roughness and larger pores with accompanying deeper "valleys" in between.

2.2.2 Porosity and pore size distribution

Several techniques have been used to measure the sinter porosities and pore size distribution.

FREE DISTRIBUTION

At Fraunhofer, a mercury porosimetry was carried out for these four different samples of porous transport layers using a Porotec PASCAL140/440 to analyse both the porosity and pore size distribution. The pore size distribution is presented Fig. 11. The geometrical information extracted from these data are given together with CEA and SINTEF ones in the Table 6.

At CEA, two techniques have been used to measure the porosity:

The first one consists in comparing the bulk Titanium density (4.51 g/cm^3) to the apparent one. It is calculated using the weight and the external volume of a sample ignoring the internal pores. Thus, the difference between bulk and apparent density is linked to the volume of all the pores of the sample. This method is non-intrusive but the closed pores are taken into account while they should not since they do not contribute to the internal flows.

The second one is the gas pycnometry using Helium. This technique compares the change in pressure caused by a measured change in a closed volume containing a reference (usually a steel sphere of known volume) with the change in pressure caused by the sample under the same conditions. The difference in change of pressure represents the volume (without the open pores) of the sample as compared to the reference sphere. Using this technique, the closed pores are ignored but the difficulty is to measure accurately the apparent volume.

The results of all techniques used are given in the following table:

Techniques	property	Sinter 1	Sinter 2	Sinter 3	Sinter 4
WLI	Roughness	11.26	10.95	19.31	11.94
Apparent volume + weight	Porosity	32.6%	33.4%	36.5%	34.4%
gas pycnometry	Porosity	33.0%	33.7%	36.8%	
Hg intrusion	Porosity	30.26%	30.68%	30.69%	30.15%
Hg intrusion	Total pore volume (mm ³ /g)	98.33	97.40	97.87	95.93
Hg intrusion	Bulk density (g/cm ³)	3.08	3.15	3.14	3.14
Hg intrusion	Total pore surface area (m ² /g)	0.052	0.084	0.032	0.196
Hg intrusion	Average pore radius (μm)	3.80	2.32	6.20	0.98
Hg intrusion	Median pore radius (μm)	5.26	4.52	10.74	4.23
Hg intrusion	Modal pore radius (μm)	5.75	4.90	11.47	4.91

Table 5: Sinter geometrical properties

The porosities measured by the three techniques are close together. It is remarkable that values obtained using helium are systematically higher than the ones obtained using mercury. The difference between helium and mercury porosity values can be interpreted as smallest pores porosity: the mercury is highly hydrophobic and thus do not enters easily the smallest pores. This is coherent with the higher dispersion of porosity values among the sinters when using helium (the sinter 3 porosity is slightly different from the others when using gas but not when using mercury). For the modelling purpose we suggest to use values from the Helium technique.

FREE DISTRIBUTION

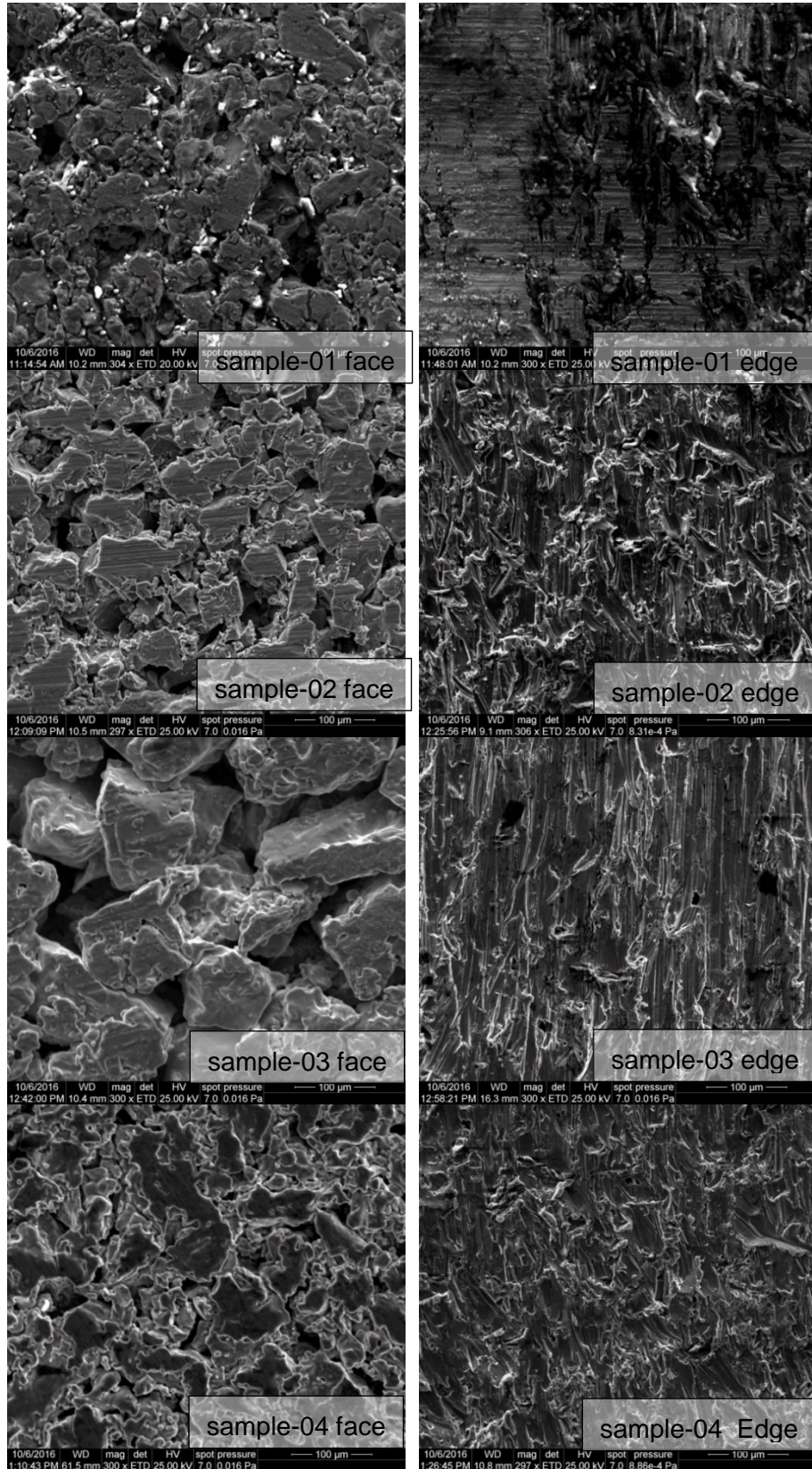


Figure 10: SEM images of all provided sinters. Left side shows “top view” images and right side shows image from the front edge.

FREE DISTRIBUTION

The SEM pictures illustrate that sinter 3 is clearly different from the others since it has larger pores and grain sizes.

X-Tomography based analysis

To investigate the properties of the different sinters and the impact of the micro-structure on their physical properties, 3D X-ray tomography reconstruction have been used. From the image analysis, we are able to analyze the geometrical properties (porosity, mean chord length and chord length distribution in each direction) and to determine the effective electrical conductivity and thermal conductivity as well as the pressure capillary curve.

X-ray tomography reconstruction is highly suited for metal current collectors as it provides excellent contrast.

Samples of the sinters 1, 3 and 4 have been X-tomographed in 3D at CEA and at Fraunhofer. The characteristics of the 2 systems are the followings:

- CEA: Phoenix Nanotom system and source voltage of 10-180 kV. The volume of the samples is 1 mm³ and the pixel size is 2µm resulting in a voxel volume of 8µm³. Example of an original X-ray image is given Figure 14.
- Fraunhofer: Skyscan 2211 from Bruker with an X-ray source of 10 - 190 kV and a nominal resolution of 600 nm is use for these measurements. The sample size is 2 cm stick with 1 mm in thickness and 1mm width.

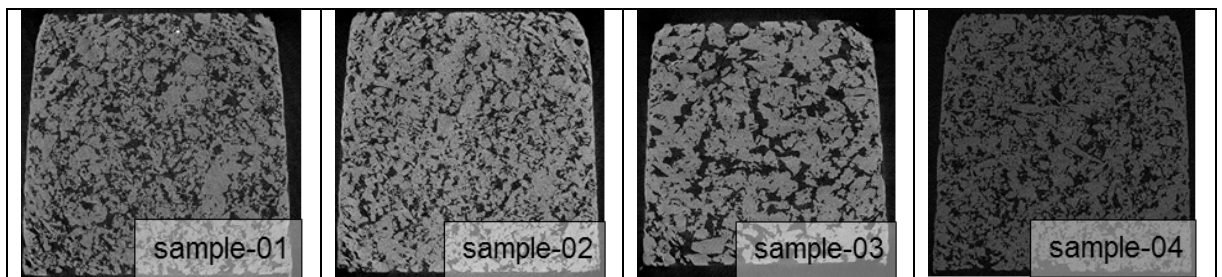


Figure 11: 2D X-ray reconstruction image for sample 1 to 4 using Skyscan 2211.
(To increase resolution, only a part of sample is shown)

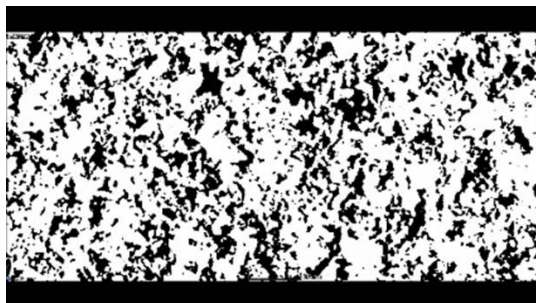


Figure 12: 2D crop of an original X-ray reconstruction image.

The segmentation threshold of the obtained images has been adjusted to recover the samples porosity obtained by apparent volume and weight measurements. Then, mean chord length, chord length distribution, effective electrical conductivity and effective thermal conductivity as

FREE DISTRIBUTION

well as pressure capillary curve were calculated on sinters 3 and 4 using CEA dedicated software. The chord length distribution for the two samples is presented Figure 15.

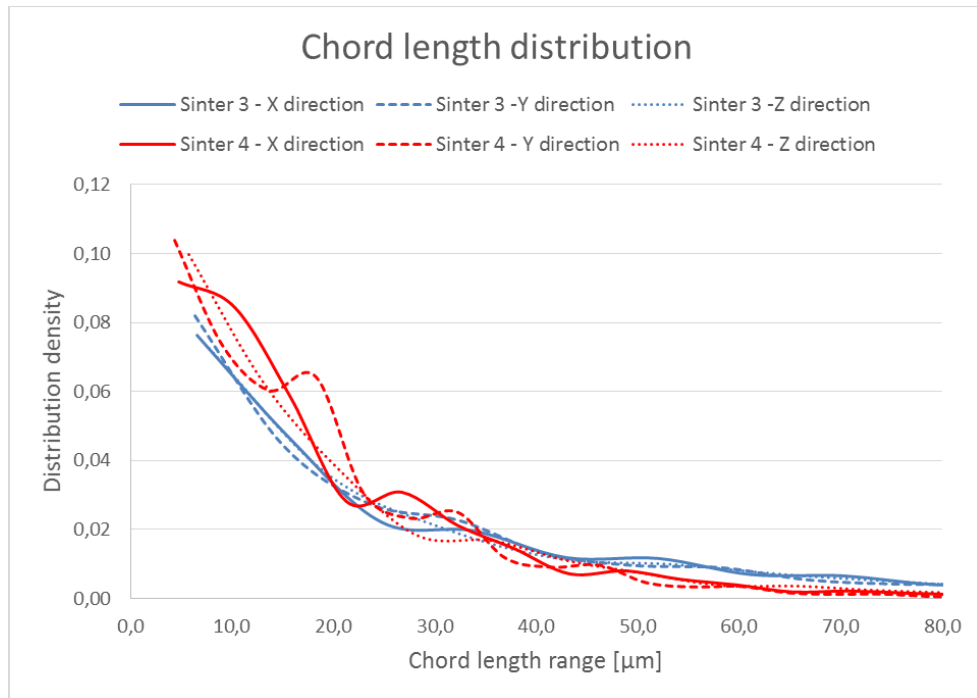


Figure 13: Sinter X-Ray image analysis: chord length distribution

For the electric conductivity, Ohm’s law is solved assuming that the only conducting phase is titanium. The effective conductivity is therefore given as a percentage of the intrinsic conductivity and the explicit value can be found by multiplying the given percentage by the bulk value given by literature. Regarding the effective thermal conductivity, it is calculated by solving Fourier’s law where both the water filled pore space and the solid titanium conduct heat. At 20°C, the bulk thermal conductivity are 0.6 W/m/K for water and 21.9 W/m/K for titanium. At 80°C, the bulk thermal conductivity are 0.67 W/m/K for water and 21 W/m/K for titanium. The obtained results are presented Table 7.

Samples	Porosity (-)	L (µm)	σ (%)	λ@20°C (W/m/K)	λ@80°C (W/m/K)
Directions		x,y,z	x,y,z	x,y,z	x,y,z
Sinter 3	36.5	28.6, 26.8, 28.9	32, 28, 38	8.3, 7.6, 9.3	8.1, 7.5, 9.1
Sinter 4	34.2	18.5, 17.5, 19.0	35, 33, 42	8.8, 8.4, 10.1	8.6, 8.3, 9.8

Table 6: Sinter’s properties obtained from X-Ray image analysis.

Capillary pressure curve have also been computed on the 3D images of sinter 3 and 4. The results obtained using Porefil properties (surface tension of $1.6 \cdot 10^{-2}$ N/m) are displayed Figure 16. The differences between sinters 3 and 4 are clearly captured and the order of magnitude is totally coherent with the experimental results that is presented in the following section. Given the resolution of the 3D images acquired at CEA (2µm), it is not possible to reach higher

FREE DISTRIBUTION

capillary pressure and study sinter 4 for low saturation values, but this could be done later with the higher resolution images acquired at Fraunhofer (600nm instead of 2 μ m)

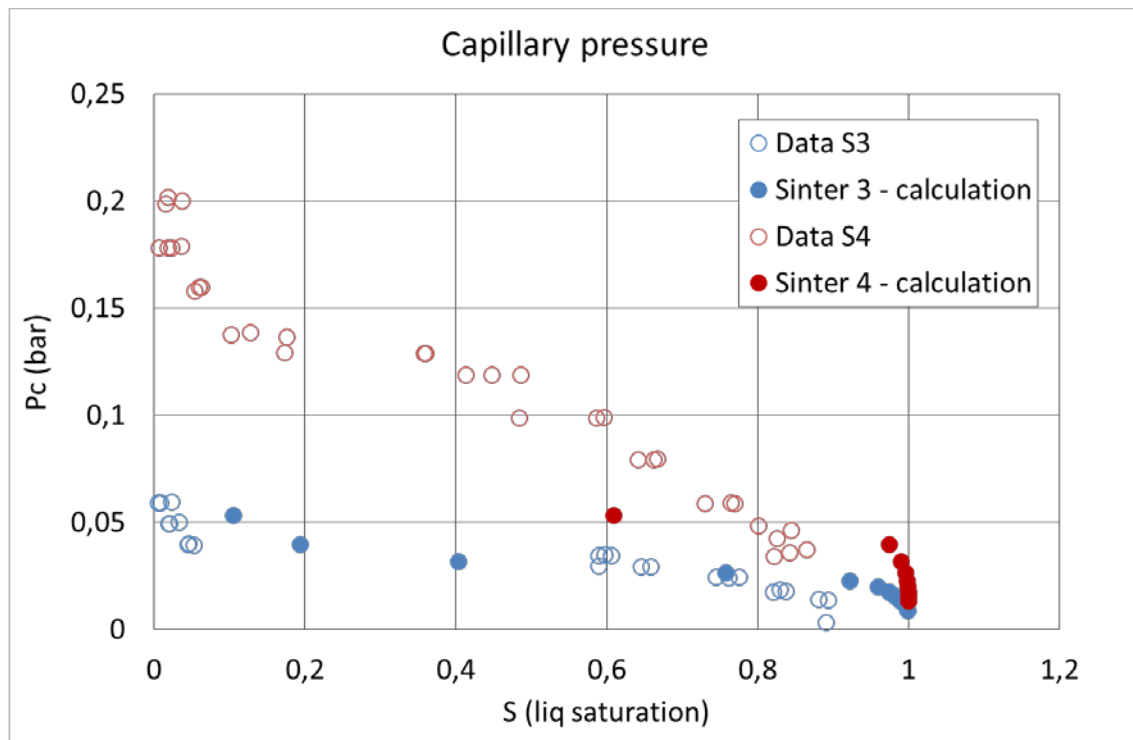


Figure 14: Capillary pressures calculated using sinter's X-Ray image analysis compared to Fraunhofer measurements with Porefil ("Data") for Sinter 3 ("S3") and 4 ("S4").

2.2.3 Permeability

Gurley through plane permeability

The first technique used at CEA to evaluate the through plane (TP) permeability of the sinters is a Gurley device. It consists in measuring the elapsed time for a specific volume of gas (300ml) to flow through a sinter sample when a pressure is applied upstream while downstream is at atmospheric pressure. Higher is this elapsed time and higher is the friction thus lower is the permeability. There is no given relation between the measured time and the permeability but the measured elapsed times give some relative information to rank the various sinter samples.

This technique has been used for the 4 sinters. The results are given in the Table 8. They are not consistent with the results obtained using the capillary porometer, thus they will not be used in the following.

FREE DISTRIBUTION



Figure 15: Gurley device

Through plane permeability by capillary flow porometry (CFP)

Through plane permeability was measured at Fraunhofer using capillary flow porometry (Porotec Porolux 1000). The samples were water jet cut to round samples with 47 mm in diameter. The gas permeability was calculated assuming Darcy’s law and the measured difference pressure (over sample thickness) versus gas flow rate. The obtained results are presented Table 8.

The porous samples were saturated using a liquid (Porefil) with very high wettability (contact angle 0°). The saturated sample was put into a sample holder and nitrogen gas flow rate was gradually increased. Flow rate and pressure were measured and bubble point, mean flow pore and smallest pore were resulting parameters. A cross section of the sample holder and measuring section and a schematic diagram of „dry and wet curve“ including characteristic pore sizes are given in Figure 18 and Figure 19, respectively.

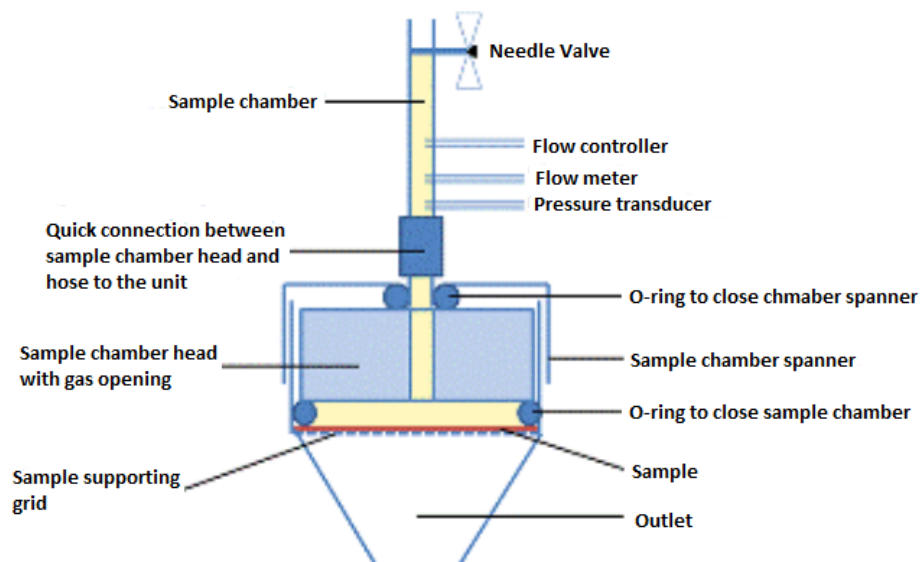


Figure 16: Schematic cross section of sample holder and measuring section of the capillary flow porometer

FREE DISTRIBUTION

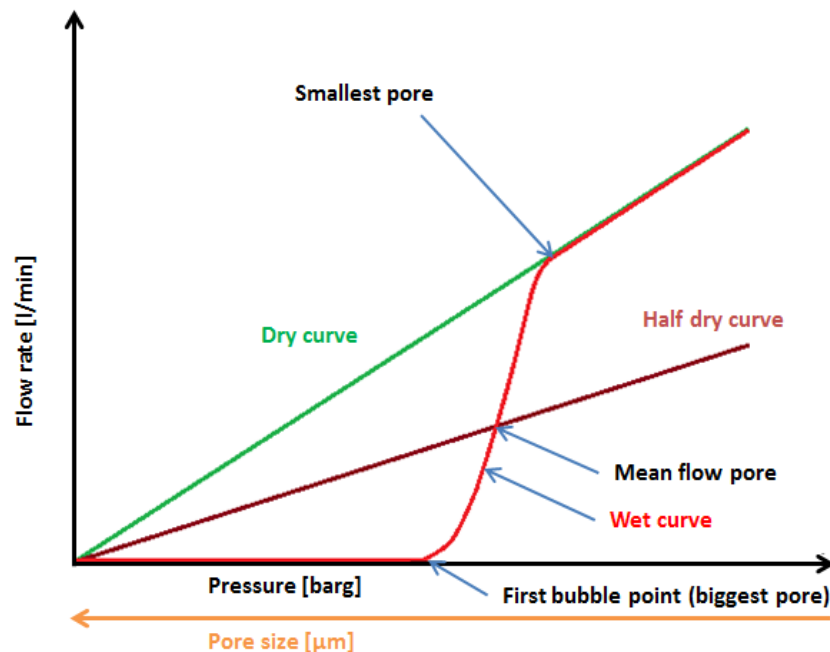


Figure 17: Schematic diagram of “dry and wet curve” with characteristic pore sizes

Techniques	Sinter 1	Sinter 2	Sinter 3	Sinter 4
Gurley	17.8 s	24.7 s	32.5 s	33.4 s
Porometry	$3.51 \cdot 10^{-13} \text{ m}^2$	$2.41 \cdot 10^{-13} \text{ m}^2$	$7.45 \cdot 10^{-13} \text{ m}^2$	$2.66 \cdot 10^{-13} \text{ m}^2$

Table 7: TP Permeability of the ITM sinters

From this table, it is clear that Gurley values are not coherent with porometry ones (the ranking is completely different) and the pore size and microstructures information. Thus, the Gurley device is not adapted for this kind of measurements and is abandoned. Further parameter extraction is based on CFP.

Largest pore size (bubble point, bp), mean flow pore size (mp) and smallest pore (sp) size were determined with the CF porosimetry at Fraunhofer. The results are given in Table 9. Sinter 1, 2, and 4 show similar results in pore size and through plane permeability. Sinter 3 shows higher pore sizes and through plane permeability.

	Sinter 1	Sinter 2	Sinter 3	Sinter 4
Bubble point pressure [bar]	0.043	0.050	0.018	0.045
Largest pore radius [µm]	7.45	6.405	17.81	7.175
Mean flow pressure [bar]	0.111	0.118	0.032	0.129
Mean flow pore radius [µm]	2.89	2.70	10.09	2.48
Smallest pore pressure [bar]	0.128	0.130	0.045	0.178
Smallest pore radius [µm]	2.49	2.46	7.19	1.80
Through plane permeability [m ²]	3.51E-13	2.41E-13	7.45E-13	2.66E-13

Table 8: Main results of CFP technique using Porefil

FREE DISTRIBUTION

A comparison of the results from mercury porosimetry and capillary flow porometry¹ is given in Figure 20. Whereas mercury porosimetry gives information about all open pores inside the sample, capillary flow porometry indicates only the effective open pores between two interfaces. Both methods show coherent results for pore sizes. Depending on the real morphology of the four samples, differences in pore sizes can be observed. Sinter 1, 2 and 4 show significant lower pore sizes compared to sinter 3.

According to mean flow pore size (MPR), measured with CFP, calculated results for gas through plane permeability is given in the same graph. The through plane permeability for sinter 1, 2 and 4 is significant lower than for sinter 3.

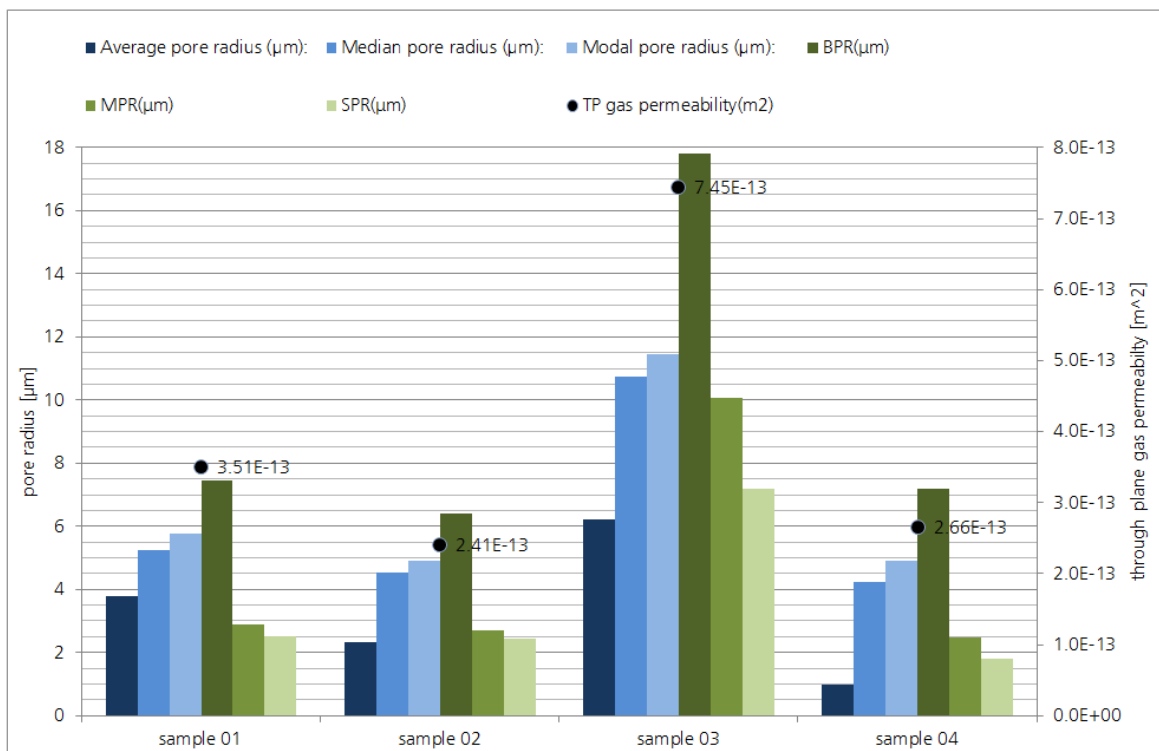


Figure 18: Comparison of all results obtained from mercury porosimetry (blue bars) and from capillary flow porometry (green bars) for Sinter 1, 2, 3, 4

To study capillary effects that are expected in real operation conditions in an electrolysis cell, water is used instead of Porefil as working liquid. All tests using CFP as described above were repeated with water and compared to measures with Porefil. Figure 21 and Figure 22 provide all measured data of the full porometry (dry curve and wet curve) using water and Porefil. It is obvious from Figure 21 and Figure 22 that water and Porefil wet curves are different for the same sinter sample. This is mainly due to the different properties of Porefil and water

¹ Porosimetry is used to name a method that is used to measure different properties of porous materials (pore size, pore volume, surface area, and porosity). It is based on the intrusion of a non-wetting liquid at high pressure into a porous material (For example Hg-porosimetry.)

Porometry is an abbreviation for capillary flow porometry and is based on the displacement of a wetting liquid from a porous sample by applying gas pressure. It is used to measure minimum, mean and maximum pore size for PTLs.

FREE DISTRIBUTION

(especially surface tension and contact angle). A complete removal of water from the sinter needs comparatively higher pressure than for the Porefil. Usage of Porefil provides accurate measurement of pore sizes and its distribution. Usage of water is closer to the real characteristics inside a PEM electrolysis cell. Therefore water was also used as a wetting liquid.

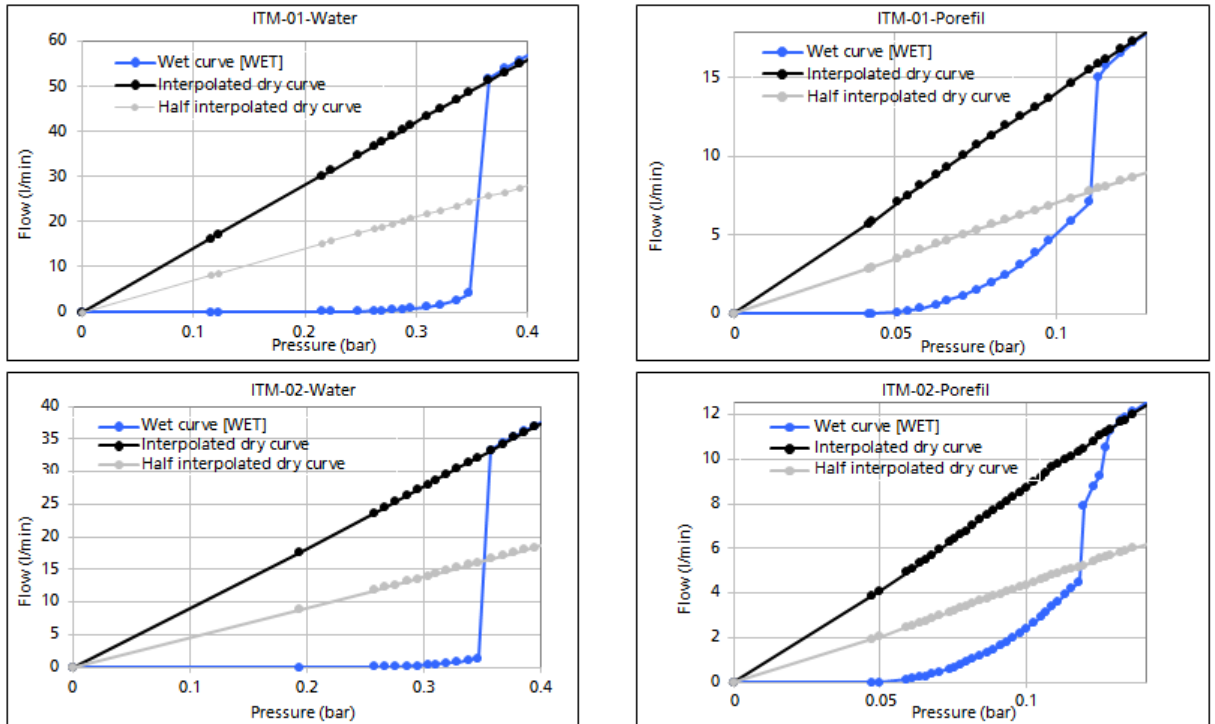


Figure 19: Full porometry for Sinter 1 (above) and Sinter 2 (below) for water (left) and Porefil (right) as working fluid

FREE DISTRIBUTION

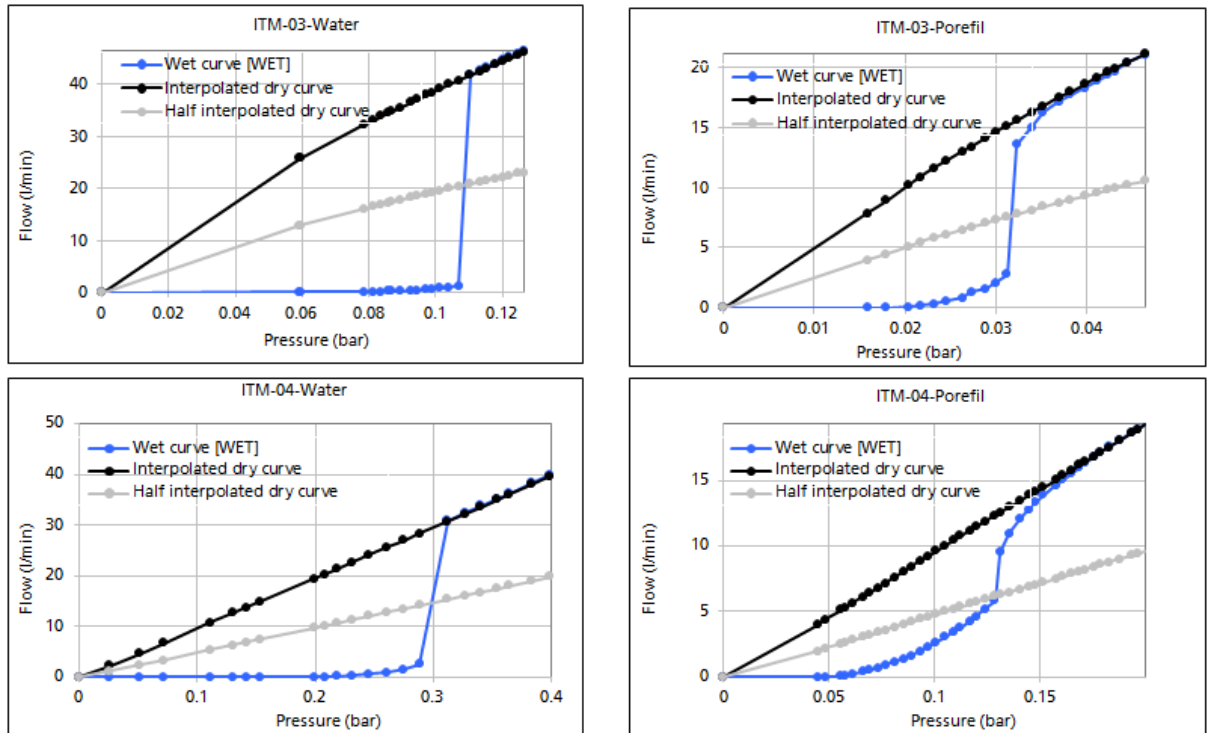


Figure 20: Full porometry for Sinter 3 (above) and Sinter 4 (below) for water (left) and Porefil (right) as working fluid

In plane permeability measures using purpose –made test set-up

The absolute in plane permeability can be measured using Darcy’s law for single-phase fluid (water and gas separately) at steady-state conditions. The required data for absolute permeability calculation can be obtained experimentally by measuring pressure drop along sample length as a function of flow rate. Darcy’s law is given as follows,

$$K = \frac{u \cdot \mu \cdot l}{\Delta P}$$

- Where,
- u [m/s] velocity of working fluid
 - K [m²] absolute permeability,
 - ΔP [bar] pressure drop across the porous media,
 - μ [Pa s] viscosity of working fluid,
 - l [m] length of porous media

Results of two-phase flow are currently not available, because of problems with getting steady state conditions for in plane water permeability (described below).

A purpose-made test cell has been designed for 50mm * 50mm square PTL at Fraunhofer ISE as already presented in Figure 5. The test cell is made of two plates. A bottom plate is made of stainless steel and contains a piston to use samples with different thicknesses. The piston

FREE DISTRIBUTION

is sealed using a silicon glue to avoid bypass through the piston. An upper plate is made of Plexiglas in order to have optical access and contains fluidic connector and pressure sensors (see Figure 23).

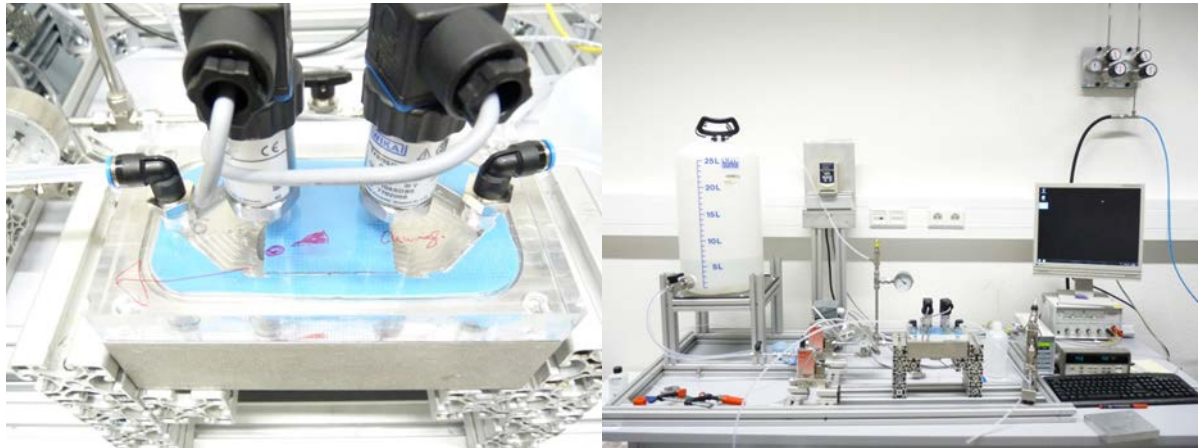


Figure 21: Purpose-made test set-up (left) and test cell (right) for in plane permeability measurements of sinters at Fraunhofer ISE

The gas flow rate is controlled by three mass flow controllers (Bronkhorst High-Tech) with flow ranges 0.16 to 30 ml/min, of 30 ml/min to 500 ml/min and 30 ml/min to 1000 ml/min. It is also possible to connect the Porolux 1000 device, to achieve flow rates up to 200 l/min. The water flow is controlled by a Cori-Flow with the flow rate range from 0.1 to 33 ml/min (Bronkhorst High-Tech). The pressure drop across sample length is measured using different pressure sensors (WIKA) with measure ranges of 0 to 250 mbar, 0 to 1.0 bar and 0 to 6 bar. To tighten both plates, manually adjustable clamps are employed. To control the applied force a force sensor (Lorenz Messtechnik, K-14) with a measure range of 0 to 10 kN is used between the cell and clamps. A sealing (blue material, see Figure 23) is used between the two plates to avoid any leakage. Additionally, the sample is covered with a special sealing material to avoid bypasses inside the cell. All measurements are performed at room temperature.

Results of in plane gas permeability

The in plane gas permeability of all sinter material were measured using a purpose-made test setup. Each sample was sealed accurately to avoid any kind of bypasses in the set-up. The sample was compressed between the two plates up to 4.15 kN. Afterward, nitrogen gas was supplied from one of the side (in an in plane direction) and corresponding pressure drops were measured across the 50 mm length of the sample. The measured pressure drop at different flow rates (scaled on the primary y-axis) and corresponding in plane permeability (scaled on the secondary y-axis) can be seen in following figure. The measurement method was optimized after measuring Sinter 01. Therefore, it is expected that Sinter 01 could have higher deviation than other sinters. Measures were done using Porolux 1000 to control gas flow rate and pressure sensors in purpose-made test cell were used to measure pressure drop.

FREE DISTRIBUTION

Measures show an increase in gas permeability with gas flow rate. To compare the in plane gas permeability a mean value was calculated in the flow range of 50 to 150 ml/min. Results are given in table below.

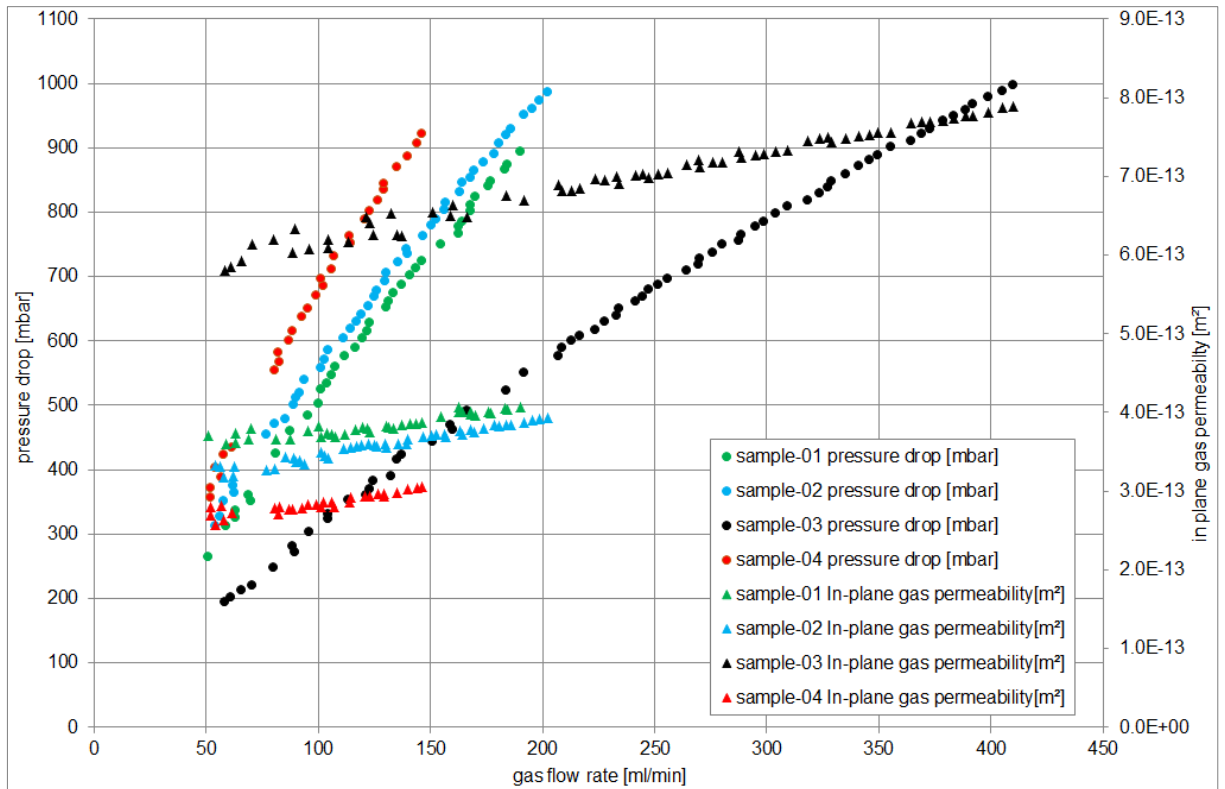


Figure 22: Measured in plane gas permeability of all four sinter materials

	sinter 1	sinter 2	sinter 3	sinter 4
K (permeability) (m ²)	3.75E-13	3.46E-13	6.17E-13	2.84E-13

Table 9: mean value of extracted absolute value of in plane gas permeability (flow range: 50 to 150 ml/min)

Besides sinter 1 and sinter 2 show similar values, sinter 3 show significant higher and sinter 4 lower values. The in plane gas permeability is compared to through plane measures and in plane water measures in at the end of this section.

Results of in plane water permeability

All samples were tested for in plane water permeability. In the course of the tests, it was observed, that for sample 1 and 2 it was not possible to reach steady state conditions. The reason for that is not clarified. Therefore, it was not possible to calculate in plane water permeability for sample 1 and 2. The tests for sample 3 and 4 were successful and the results are given in the following figure.

FREE DISTRIBUTION

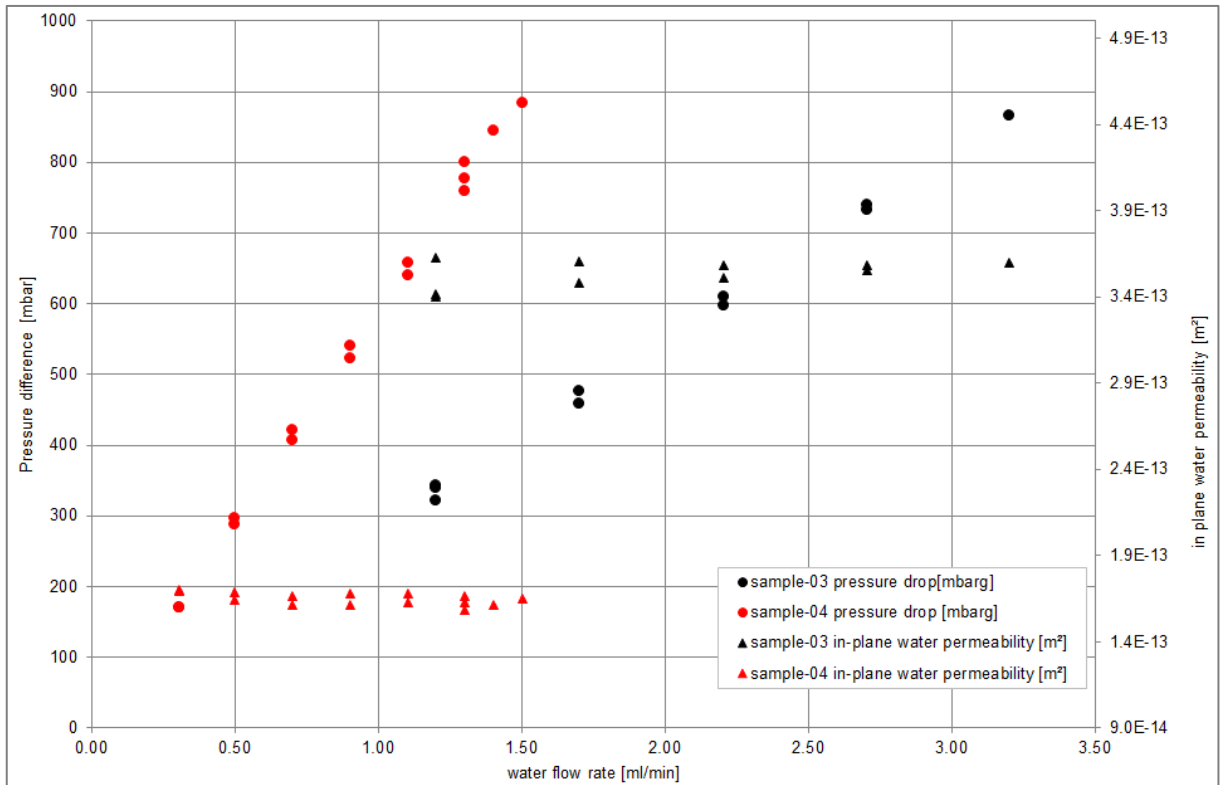


Figure 23: Measured in plane water permeability of sinter 3 and 4

As can be seen from the measuring results, water permeability keeps constant with water flow rate. The flow rate in these experiments is limited by used pressure sensors (0 to 1 barg). To compare the in plane water permeability a mean value was calculated. Results are given in the following table.

	sinter 3	sinter 4
K (permeability) (m²)	3.54E-13	1.65E-13

Table 10: mean value of extracted absolute value of in plane water permeability

It should be noted, that calculated in plane gas and water permeability is expected to be lower than stated. We assume a theoretical length of 50 mm for each PTL sample. To ensure, that channels for pressure sensors are not blocked by the sealing material, length of sealing in uncompressed state is 42.5 mm. In compressed state the length of sealing becomes higher, but keeps unknown. Consequently, the effective length in Darcy equation is smaller than sample length. Conservative estimation for expected deviation is less than 15 %. That results in a smaller permeability than given in this section.

A comparison of through plane gas permeability, in plane gas permeability and in plane water permeability is given Figure 26.

Sample 3 shows highest values for all measured permeabilities compared to other samples. This result is coherent with results of pore size from mercury porosimetry and CFP. The

FREE DISTRIBUTION

mentioned unknown accuracy for in plane measures should be taken into account for all absolute comparisons between through plane and in plane values.

A relative comparison of in plane gas and water permeability of sample 3 and 4 should be adequate, because the same sealing material was used and thus same effective length is assumed. Sample 4 shows quite similar values for in plane gas and water permeability, whereas sample 4 shows significant lower in plane water permeability compared to in plane gas permeability.

The through-plane gas permeability is lower than the in-plane gas permeability for all sinters. From a microstructure point of view, this means that the PTL material is not perfectly isotropic. The observed tendency is coherent with the measured electrical and thermal conductivities computed on 3D images for which it was the opposite behavior: the through plane conductivities (z direction) are higher than the in-plane ones.

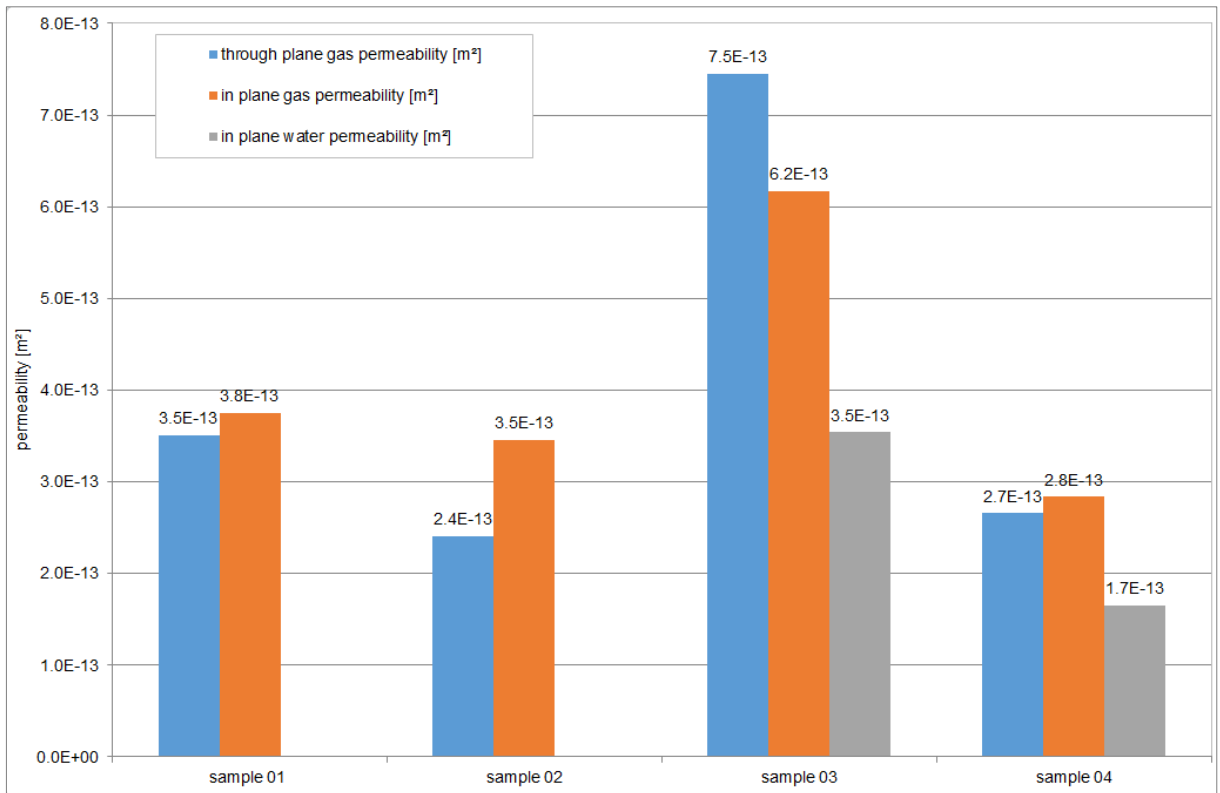


Figure 24: Comparison of through plane gas and in plane water and in plane gas permeability of all four sinter materials

2.2.4 Capillarity

To study the capillary behavior of sinters used as PTL, the CFP approach was used to extract a capillary versus liquid saturation characteristic of each sinter. Therefore, the full porometry was repeated several times for every sinter with decreasing target pressure. After each run,

FREE DISTRIBUTION

the sample weight was measured to calculate the liquid saturation by referencing to weight of dry sample and using porosity data from mercury porosimetry. Following Figure 27 explains schematically the procedure.

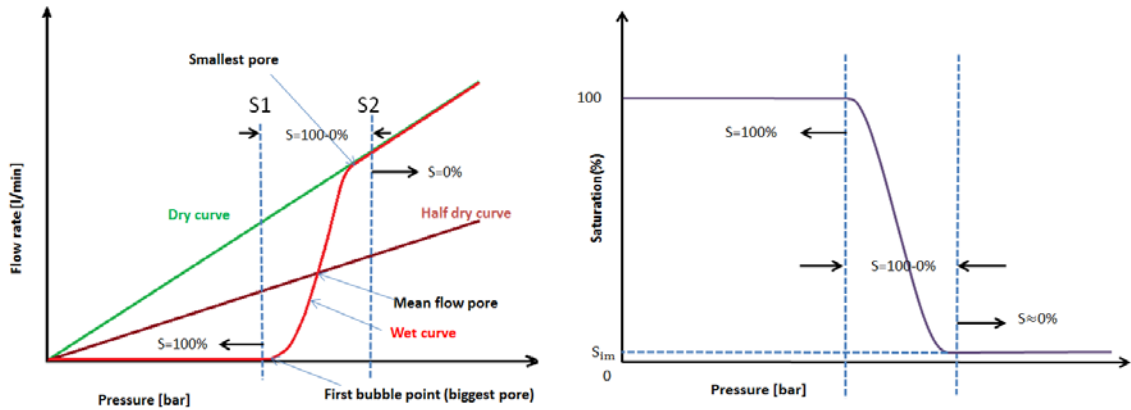


Figure 25: CFP with focus on a flow rate vs. pressure (left) and saturation vs. pressure (right)

In the deployed CFP device, different setting parameters have to be preselected. To choose the best parameters in terms of accuracy and reproducibility, a sensitivity study was performed using an available sinter (denoted as “sample-0”). This sinter 0 had been provided initially by ITM at the beginning of the project for pretesting issues. From the sensitivity analysis an optimum setting of parameters are determined, which has the lowest relative average error in pore size measurement. Following table summarizes the characteristic pore sizes, standard deviation and relative averaged error for three full porometry measures with Sinter 0.

Sinter 0	Pore diameter	Mean value [μm]	Standard deviation [μm]	Relative av. error [%]
Default case no. 3	Bubble point pore	31.19	0.05	0.15
	Mean flow pore	20.53	0.42	2.07
	Smallest pore	17.60	1.07	6.09

Table 11: Deviation in pore sizes measures and relative average error after execution of a sensitivity analysis for CFP device settings

As can be seen, the relative averaged error for bubble point pore size and mean flow pore size is low. For smallest pore size the error is higher. This result is acceptable, because the pressure region of interest is the low pressure regime near the bubble point.

FREE DISTRIBUTION

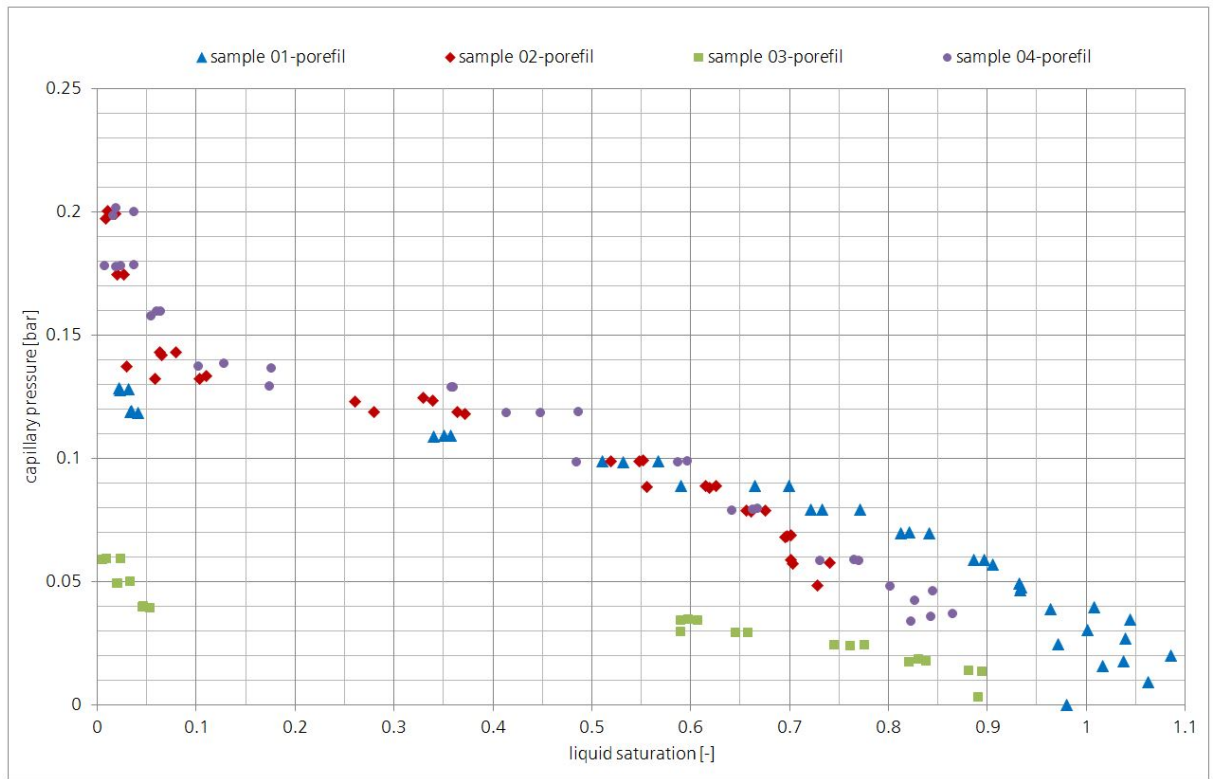


Figure 26: Capillary pressure vs. liquid saturation using Porefil as working liquid. To calculate liquid saturation, porosity of mercury porosimetry was used.

Sinters 1, 2 and 4 show a similar characteristic of capillary pressure vs. saturation. In contrary sinter 3 shows much lower capillary pressure. These findings correlate well with the results of pore size distribution from the mercury porosimetry, compare to Figure 11.

Again, the procedure was repeated with water instead of Porefil. The results are shown in following figure.

FREE DISTRIBUTION

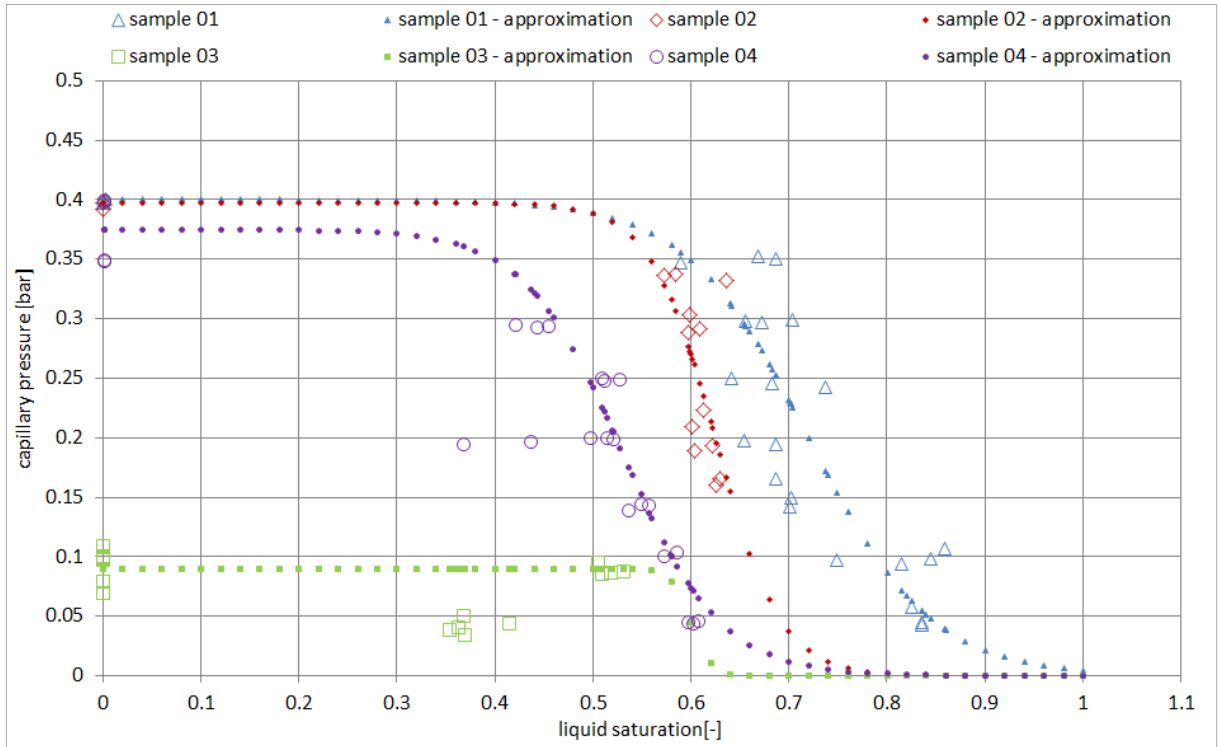


Figure 27: Capillary pressure vs. liquid saturation using water as working liquid

It is evident from Figure 29 and Figure 28 that, water capillary pressure is higher than Porefil and maximum water saturation is lower than the maximum Porefil saturation. This can be explained by higher surface tension and contact angle of water than Porefil. The characteristics are quite different compared to the Porefil results. Having a deeper look on Figure 21 and Figure 22 it becomes obvious, that the steep increase in flow rate for water results in an abrupt decrease of capillary pressure for higher saturations. Sinter 1, 2 and 4 show similar capillary pressure vs. saturation characteristic, whereas Sinter 3 shows much lower capillary pressure. Again this correlates well with the results for pore size distribution in Figure 11.

2.2.5 Contact angle

Fraunhofer ISE used a new approach to measure contact angle for water in PTL materials using CFP. As described the CFP measures are based on three different curves (dry curve, half dry curve, wet curve). Using these three different curves and Washburn's equation (1921), pore size can be obtained. It is expressed as follow,

$$D_p = \frac{4 \cdot \gamma_p \cdot \cos \theta_p}{P_p}$$

Where, D_p	[μm]	pore diameter
γ_p	[Dyn/cm]	surface tension of wetting liquid
θ_p	[Degree]	contact angle of wetting liquid with substrate
P_p	[barg]	applied pressure

FREE DISTRIBUTION

Basically, in CFP any liquid can be used with a known value of surface tension and contact angle. The measured pore sizes must be the same for the different wetting liquids. Porefil can be taken as reference liquid since the exact value of both the parameters (surface tension and contact angle) is known. Therefore Porefil is used here as wetting liquid and Washburn's equation (1921) for the Porefil liquid is expressed.

Afterward, the liquid of interest can be used as a wetting liquid to obtain the wet curve for the same porous sample. It is worthwhile to mention that for the measurement of the wet curve, the surface tension of liquid and contact angle are not required (but for the pore size calculation they are needed). Here liquid of interest is water. If water is used as a wetting liquid instead of Porefil, then the equation can be rewritten with subscript 'w'.

$$D_w = \frac{4 \cdot \gamma_w \cdot \cos \theta_w}{P_w}$$

As mentioned above, measured pore size (biggest, smallest & mean) must be same irrespective of used liquid for the same sample. Therefore, both equations, are made equal:

$$D_w = D_p = \frac{4 \cdot \gamma_p \cdot \cos \theta_p}{P_p} = \frac{4 \cdot \gamma_w \cdot \cos \theta_w}{P_w}$$

Since Porefil liquid is a special kind of liquid with a contact angle of 0° on almost all the engineering materials, it leads to term $\cos \theta_p \cong 1$.

Now, extracting θ_w from the above equation:

$$\frac{\gamma_p \cdot 1}{P_p} = \frac{\gamma_w \cdot \cos \theta_w}{P_w}$$

$$\cos \theta_w = \frac{\gamma_p \cdot P_w}{\gamma_w \cdot P_p}$$

$$\theta_w = \cos^{-1} \left[\frac{\gamma_p \cdot P_w}{\gamma_w \cdot P_p} \right]$$

The surface tension of Porefil and water are known at given temperature. The value P_w and P_p (for the same pore size) can be obtained experimentally by performing the full porometry using water and Porefil respectively.

This method could be used for expected contact angles between 0° and 90° .

In CFP standard procedure, there are three typical pore sizes available to determine the contact angle for water. An evaluation was done to find the most promising approach with lowest measurement error. It was found, that mean flow pore size provides best results. The highest relative average error was found for sample one with 5.7 % and the lowest for sinter four with 3.3% respectively.

FREE DISTRIBUTION

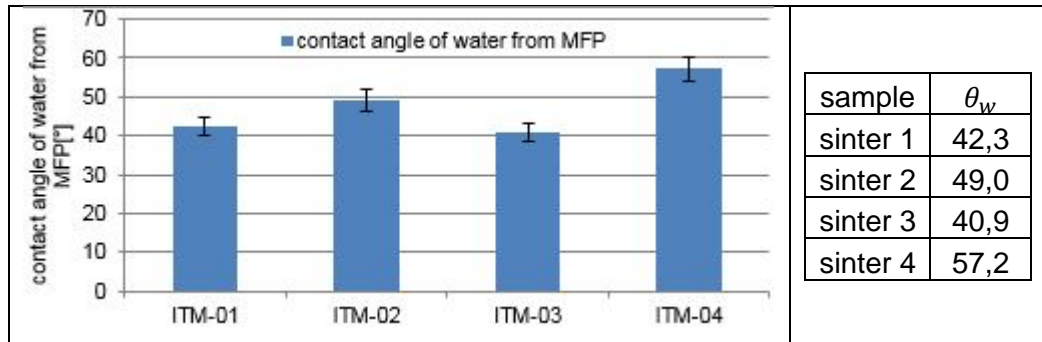


Figure 28: contact angle of water for four sinter materials.

These results indicate, that water contact angle of sample 3 is significant lower than of sample 4. Therefore, sample 3 is more hydrophilic than sample 4. Assuming same pore size, a higher capillary pressure for given saturation is expected for sample 3 compared to sample 4.

Comparing the results of capillarity in section 2.2.4, sample 3 shows the lowest capillary pressure among all samples. It becomes clear, that differences in pore sizes for sample 3 and 4 have a higher influence on capillary pressure than differences in contact angles.

2.2.6 Electrical conductivity – contact resistances

Electrical conductivity and contact resistance measurements have been performed in the three institutes using similar techniques. In principle, a 2-wire and a 4-wire set-up, respectively, can be applied, see Figure 31. The idea is to determine the electric resistance or conductivity of a sample by imposing an electrical current on both sides of the sample and then measuring the potential drop at the same contact points. The resistance is deduced using Ohm's law.

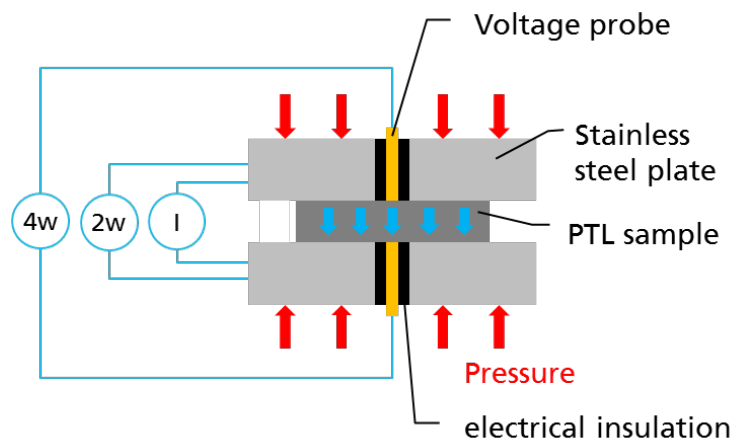


Figure 29: Scheme of the test set-up for 4-wire (for bulk resistance) and 2-wire (overall resistance including contact resistances) configurations, respectively.

Attention must be paid to the way of measuring the potentials in order to get rid of the wires resistance. To that end, different wires are used for imposing the current and measuring the

FREE DISTRIBUTION

potential difference. Another point of attention is the pressure imposed on the sample. Since the sinter is placed together with other material in the device, contact resistances are present and they depend strongly on the contact pressure.

Measurements performed at Fraunhofer

Measurements of sample thickness and (electrical) TP resistance as function of contact pressure were carried out at Fraunhofer ISE for sinter 1, 2 and 3. A contact pressure up to 6 MPa could be applied with the available set-up. Thickness measurement were performed by eddy current sensors with a resolution of 0.003 mm. Contact plates as indicated in Figure 31 were made from stainless steel. All samples had a diameter of 12 mm.

4-wires measurement of bulk resistance were not successful as the electrical resistance was too low for the measuring instruments. Therefore only 2-wire resistance measurements were carried out. All samples were measured three times with increasing and decreasing contact pressure in order to study the setting behavior. The measured values were divided by factor 2 so that only one contact between sample and SS plate had been taken into account. Bulk resistance was neglected.

All sinters showed a compression of 0.03 mm at a contact pressure of 6 MPa and a low compression setting behavior. Neglecting the bulk resistance the measured contact resistances against stainless steel at 1.5 MPa were 4 - 7 mΩ*cm² for sinter 1, 7 - 25 mΩ*cm² for sinter 2 and 3 - 27 mΩ*cm² for sinter 3. As an example the results of sinter 1 are given in Figure 32.

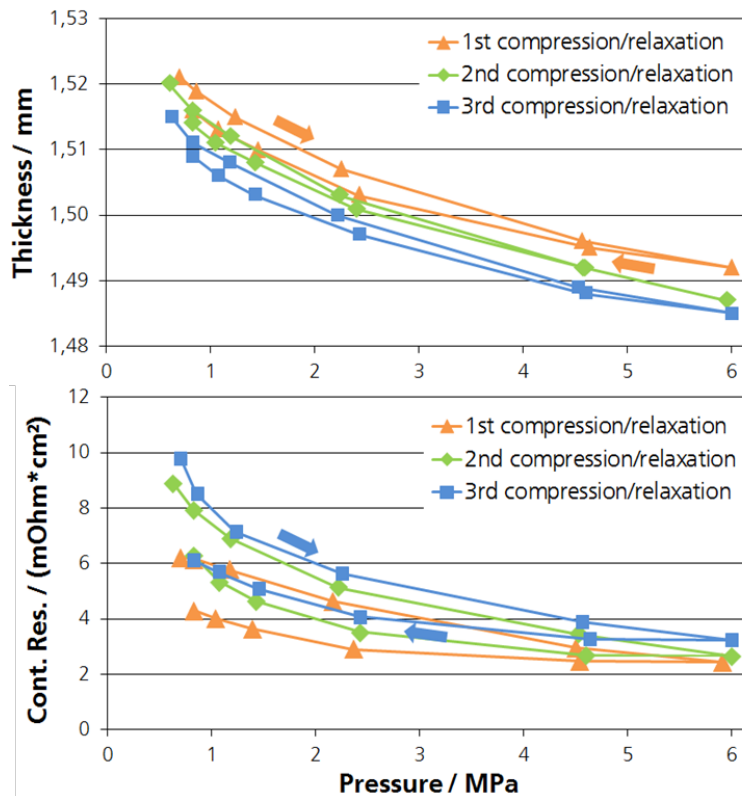


Figure 30: Results for sinter 1 measured with a 2-wire configuration

FREE DISTRIBUTION

Measurements performed at Sintef

Contact resistance measurements of the sinters were also performed at SINTEF using a setup similar to the one described in Figure 31, but with an additional carbon GDL in between the voltage probe and the Ti-sinter. The use of a carbon GDL gives values for contact resistance between a soft (GDL) material and the hard Ti-surface which does not break down the oxide layer on the Ti sinter surface. As can be seen from Figure 33 there is a large variation of the contact resistance between the sinters. Sinter 3&4 have a low contact resistance due to the conductive coating applied, while sinter 1&2 have a significantly higher contact resistance due to the presence of an insulating oxide on the surface.

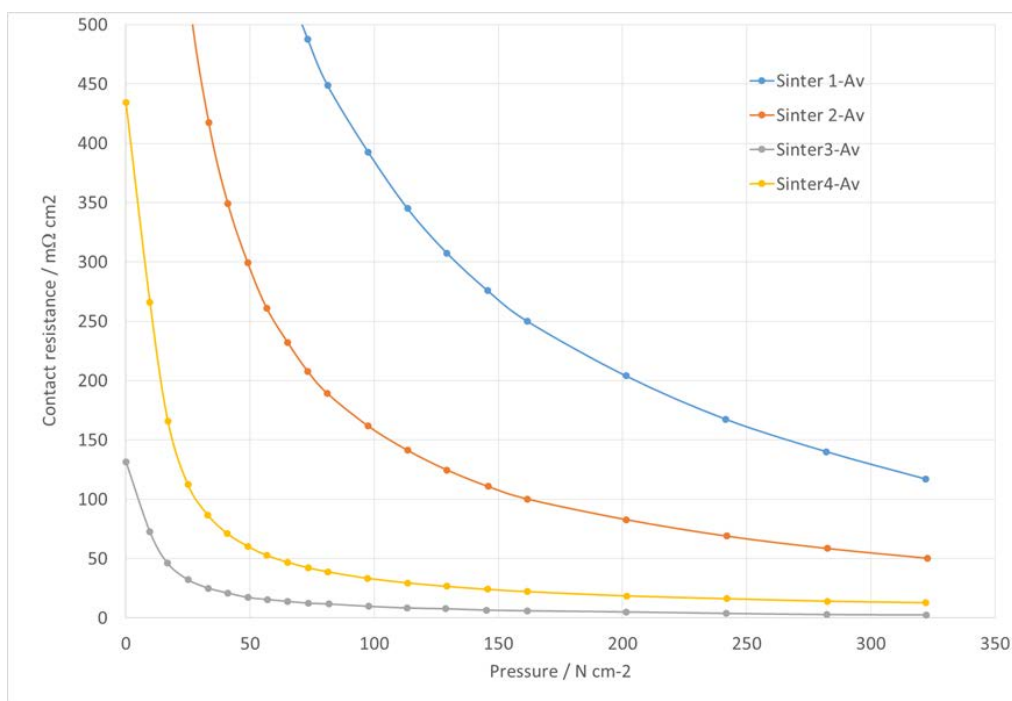


Figure 31: Contact resistance measurements of sinters in contact with a carbon GDL with microporous layer. Average values for three parallels.

Measurements performed at CEA

Various resistance have been measured at CEA: sinter alone, sinter with mesh, sinter with GDL, sinter with MPL and GDL... There are plotted on the following figures. Each measurements have been performed using at least two samples. The first number following the key word "sinter" in the legends corresponds to the number of the sinter and the second one to the number of the sample. Resistances have been measured as a function of contact pressure. The contact plates are made of copper. From the Table 7, we know that the sinter bulk resistance varies between 30 to 40% of the pure Titanium one. Thus an order of magnitude of the sinter bulk resistance is $1\mu\Omega\cdot\text{cm}^2$ which is negligible compared to the all the measured values. Therefore, the resistances given hereafter correspond to the sum of all the contact resistances.

The measured resistances of the sinters (Figure 34) give an order of magnitude of the contact resistance between one sinter and the two contact planes (in copper). Under contact pressure,

FREE DISTRIBUTION

the order of magnitude of the sinter contact resistance with copper plates is lower than $5\text{m}\Omega.\text{cm}^2$ which is very low comparing for example with membrane resistance. The sinter 3 has the lowest resistance (about 4 times less than sinter 1). There are some dispersions that are interpreted as uncertainties due to low potential values. This is why we use order of magnitude instead of precise values. The problem of dispersion has also been met by Fraunhofer that has found similar order of magnitude for the sinters.

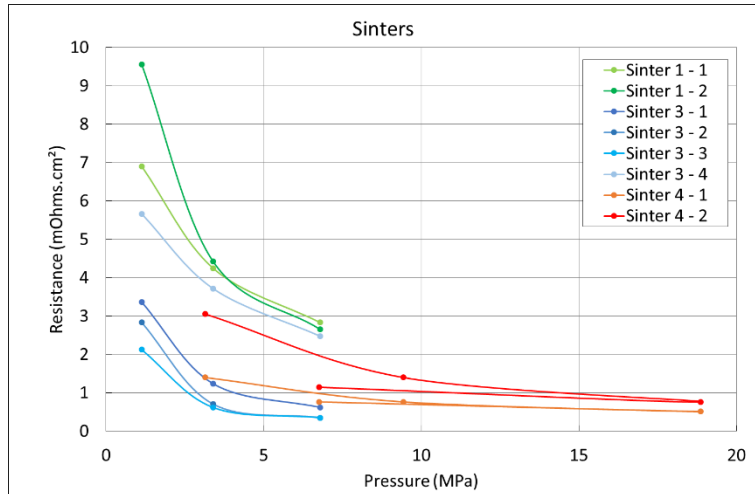


Figure 32: resistances of the sinters

The contact resistance that is more interesting is the one between the meshes and between the mesh and the sinter. From Figure 35, it is clear that the contact resistances between two meshes have an order of magnitude very low: $1\text{m}\Omega.\text{cm}^2$ (see the blue curves). The contact resistance between one mesh and one sinter is slightly higher: between 2 and $5\text{m}\Omega.\text{cm}^2$ which remains a very low value.

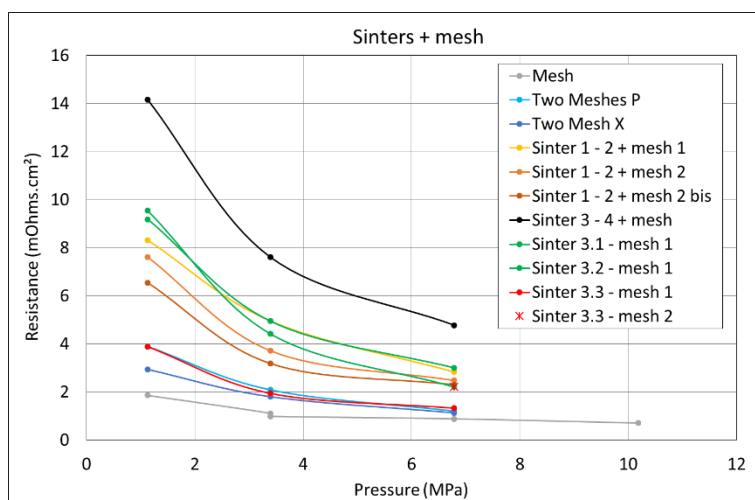


Figure 33: resistances of meshes and mesh with sinter

The contact resistances for sinter and mesh were very low due to the “hard” contact between samples. The question that arises is the contact resistance for the “soft” contact that exists

FREE DISTRIBUTION

between sinter and MEA and which could be higher. Since it is not possible to use MEA for ex-situ electrical measurements, we evaluate the soft contact resistance using a GDL instead of a MEA. As seen Figure 36, the GDL resistance itself is very low: less than $2\text{m}\Omega\cdot\text{cm}^2$. But, the contact resistance between GDL and two sinters is quite higher: between $15\text{m}\Omega\cdot\text{cm}^2$ and $30\text{m}\Omega\cdot\text{cm}^2$.

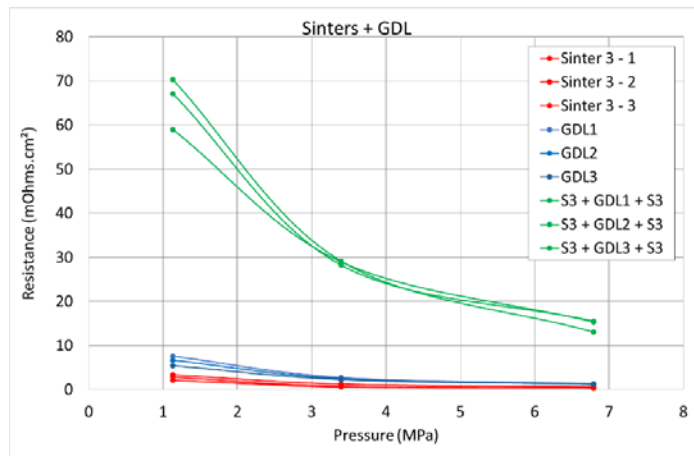


Figure 34: resistances of the sinters with GDL

Adding a MPL to the GDL in order to be more representative of the MEA structure, leads to a reduction of the soft contact resistance (see red curves on Figure 37) that remains an order of magnitude higher than hard contact: about $5\text{m}\Omega\cdot\text{cm}^2$ for one sinter with one MPL and one GDL, thus, about $10\text{m}\Omega\cdot\text{cm}^2$ considering two sinters.

Looking at the global contact resistances in a cell that include mesh, sinter, MPL and GDL (see blue curves on Figure 37) and multiplying by two (two sides of the cell), this resistance is higher than the previous one: lower than $20\text{m}\Omega\cdot\text{cm}^2$. When adding the CEA small mesh that is required to fill the CEA cell, the resistance increases significantly as seen on the green curves, reaching between 30 and $60\text{m}\Omega\cdot\text{cm}^2$ depending on the pressure (values have been multiplied by two to take both side of the cell into account).

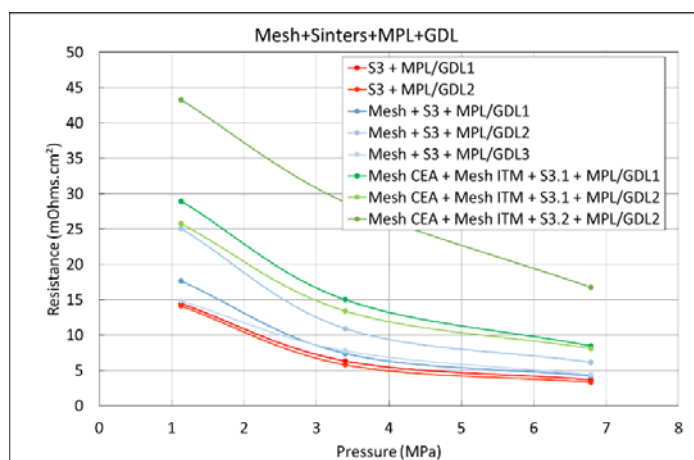


Figure 35: resistance of mesh+sinter+MPL+GDL.

FREE DISTRIBUTION

As a conclusion on the electrical resistances measured at CEA:

- Even if there are some dispersion in the values, the order of magnitude are captured.
- The contact resistances are much higher than the bulk ones (by several order of magnitude).
- Among them, the soft contact resistances (sinter/GDL) are few times higher than hard contact ones (sinter/mesh).
- All of these resistances are quite lower than the membrane one (~ 100 mΩ.cm²).

The Table 13 summarizes the order of magnitude of the measured values. From this table we estimate that the CEA cell has an ohmic resistance, not including the membrane, that is twice the values listed in the last line of the table. Thus it ranks inside [26–58] mΩ.cm² at 35MPa and [16–34] mΩ.cm² at 70MPa. The total ohmic cell resistance measured in-situ (including MEA) using EIS (see section 3.1.3) ranks between 160 and 280 mΩ.cm².

Components in between to copper electrodes	~ 35 MPa	~ 70 MPa
1 Sinter (2 hard contacts)	< 5	< 3
1 mesh (2 hard contacts)	1	1
2 meshes (P or X) (3 hard contacts)	2	< 2
1 mesh + 1 sinter (3 hard contacts)	[2 – 8]	[2 – 5]
1 GDL (2 soft contacts)	< 3	< 2
2 sinters + 1 GDL (2 hard contacts + 2 soft contacts)	30	15
1 sinter + 1 MPL/GDL (1 hard contact, 2 soft contact)	6	4
1 mesh + 1 sinter + 1 MPL/GDL (2 hard contacts + 2 soft)	[7 – 12]	[4 – 6]
1 CEA mesh + 1 ITM mesh + 1 sinter + 1 MPL/GDL (3 hard + 2 soft)	[13 – 29]	[8 – 17]

Table 12: Order of magnitude of the cell components contact resistances.
Resistance values are given in mΩ.cm².

From the measured values it is possible to evaluate the ohmic resistances of the CEA cell used for the electrochemical tests described in the following section. This cell, described in section 3.1.1, includes a CEA mesh, two ITM meshes, a sinter on the anode side, a membrane and on the cathode side a sinter, one ITM mesh and a CEA mesh. Excluding the membrane resistance that is calculated in section 4.3, the global contact resistance of the CEA components has been calculated as a function of contact pressure and plotted on Figure 38 for 2 meshes configurations with sinter 3. The mesh configuration has no effect on the total contact resistance of the cell.

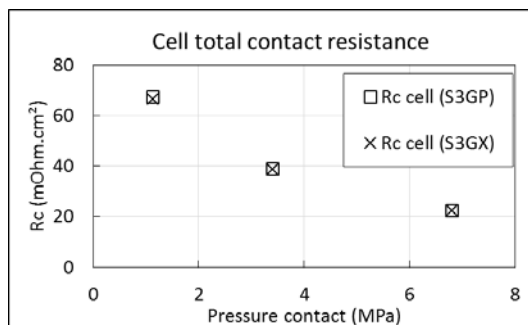


Figure 36: Total contact resistance of the cell

FREE DISTRIBUTION

3. ELECTROCHEMICAL MEASUREMENTS

The objective of this section is to determine in-situ the physical and electrochemical performance of ITM's key components (meshes, MEA and sinter). To that end small surface single cells with ITM's key components have been assembled and tested at various temperatures and pressures at both CEA and Fraunhofer.

3.1 Experiments performed at CEA

3.1.1 Cell description and measurements

Starting from the anode side, the 25cm² surface homemade cell is made of 1 Ti plate flow field-free (CEA), a small Ti mesh (CEA) used to fill the cell, 2 large Ti meshes (ITM), 1 Platinum coated porous Titanium current collector, the MEA (ITM), the same current collector that was used on the anode, 1 large Ti mesh (ITM), 1 small Ti mesh (CEA) and 1 Ti plate. A representation of the cell is depicted on the Figure 39.

After a MEA hydration protocol that lasts 3 days, the MEA is conditioned for 16h. The polarization curves are performed with hot water at (40 – 60- 80°C) with an injected water flow rate of 200 g/h at the anode. No water is provided to the cathode side, like in ITM design. The cell is also thermostated with heating mats placed on the end plates of the cell. The experimental tested operating conditions are gathered Table 14.

Inlet water flowrate at anode (g/h)	200
Inlet and internal temperatures (°C)	40 / 60 / 80
Anode – Cathode pressures (bar)	(1-1) / (1-8) / (6,5-8)

Table 13: experimental conditions for the CEA cell



Figure 37: Flow field-free PEM WE cell picture

FREE DISTRIBUTION

The sinters 3 and 4 have been alternatively used. On the anode side, the 2 main ITM meshes have been either set parallel or perpendicular. The 3 configurations that have been studied are summarized in Table 15.

Configurations	Denominations on figures and tables
Sinter 3 and parallel meshes	S3GP
Sinter 3 and perpendicular (crossed) meshes	S3GX
Sinter 4 and parallel meshes	S4GP

Table 14: cell configurations for electrochemical measurements studied at CEA

3.1.2 Water flow balance

Since liquid water is injected only on the anode side, the measured water flowrate at the cathode outlet corresponds to the water flowrate through the membrane. It is used to validate the diffusion and electro-osmosis laws together. Moreover, measuring flowrate at both the cathode and the anode outlet, knowing the inlet and the consumed flowrates of water, gives the water flowrate errors.

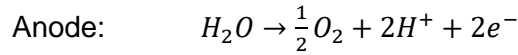
The experimental protocol is the following. During the polarization curves measurements performed at 1 bar on both sides, the water flowrates are measured at both the cathode and the anode for several current values. To do this, the outgoing water from anode and cathode are collected during a certain time and weighted. Then the averaged flowrate for this elapsed time is calculated. Since the water flowrate through the membrane is an increasing function of the current and thus varies significantly along a polarization curve, the collecting times were very high for low currents and smaller for higher ones.

On Figure 40, the mass flowrates versus current density have been plotted for 40°C, 60°C and 80°C in the configuration sinter 3 and crossed meshes. The left column correspond to all the liquid water flowrates: injected at the anode side, measured at the anode and cathode sides, the consumption and finally the balance error. These graphs clearly show the evolution of liquid flowrates against current and that the committed error is quite low, giving an accurate water balance. On the right column, only the cathode and error flowrates have been plotted. The reason is that the liquid flowrate is very low at cathode for low current density and therefore, an important time is requested to measure a very small amount of water; leading to a potential important error, evaporation being possible during this elapsed time. For example at (60°C, 0.1 A/cm²), (80°C, 0.1A/cm²) and (80°C, 0.2A/cm²) the committed errors are as important as the measured values at cathode. Thus, these values must be eliminated for the water permeation analysis. This analysis has been performed also for the two other configurations (sinter 3 parallel meshes and sinter 4 crossed meshes, not shown here) in order to eliminate the doubtful data. Fortunately only few number of data has been eliminated.

The water transfer is plotted versus current density for each temperature and for each cell configuration. The water transfer is defined here as the ration of the cathode water flowrate to

FREE DISTRIBUTION

twice the water consumed flowrate in order to take reaction stoichiometry into account: for 1 molecule of water consumed, 2 protons are released and are involved in the electro-osmosis flux as illustrated on the following equation on the anode side:



Therefore if the diffusion was zero and the electro-osmosis coefficient was a constant, then the water transfer curve should be a horizontal line whose amplitude would be equal to this electro-osmosis coefficient. Thus, the deviations from this simplified vision have to be interpreted as the result of the diffusion flux and the electro-osmosis coefficient variations.

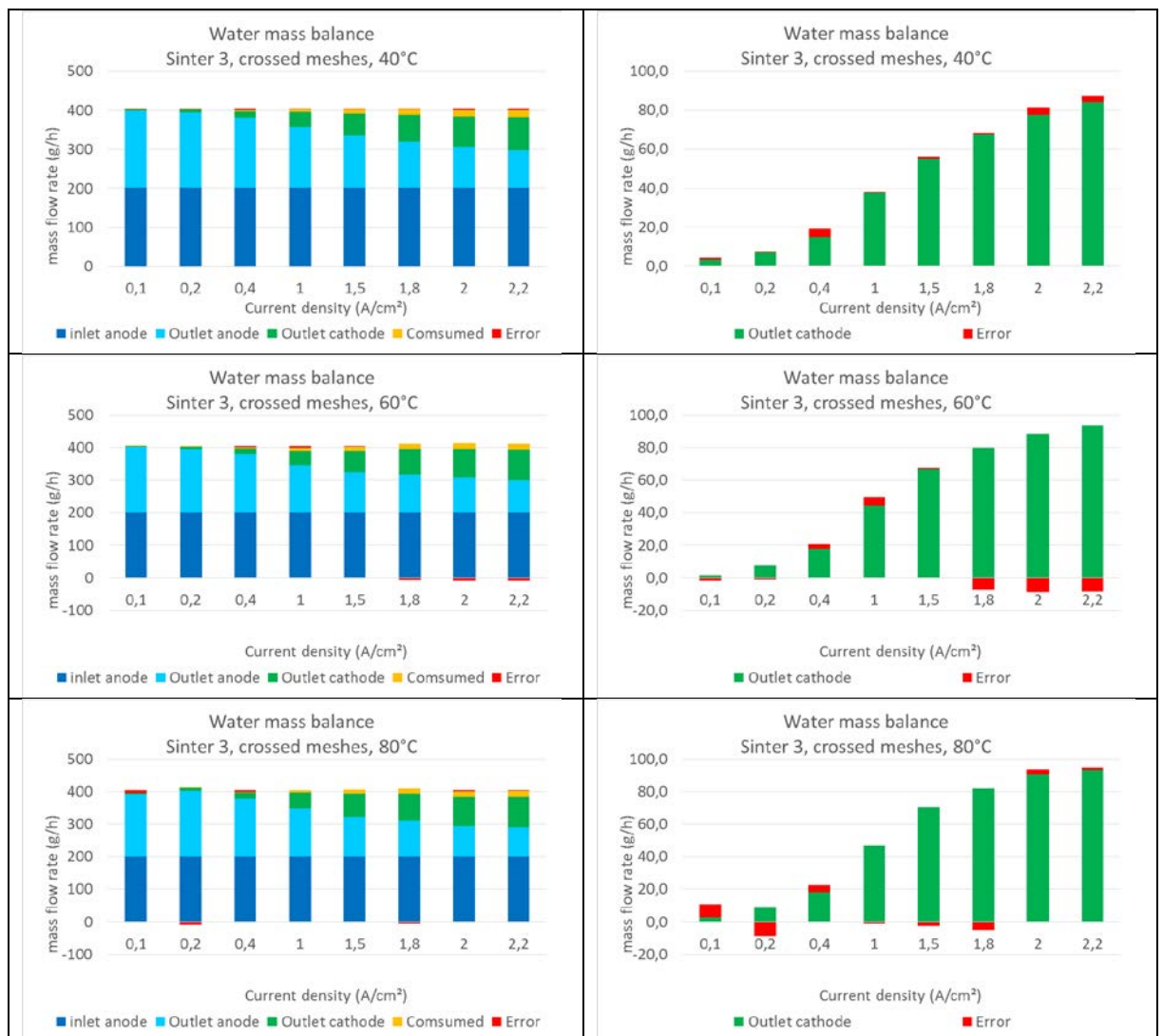


Figure 38: Water mass balance for sinter 3 and crossed meshes.

FREE DISTRIBUTION

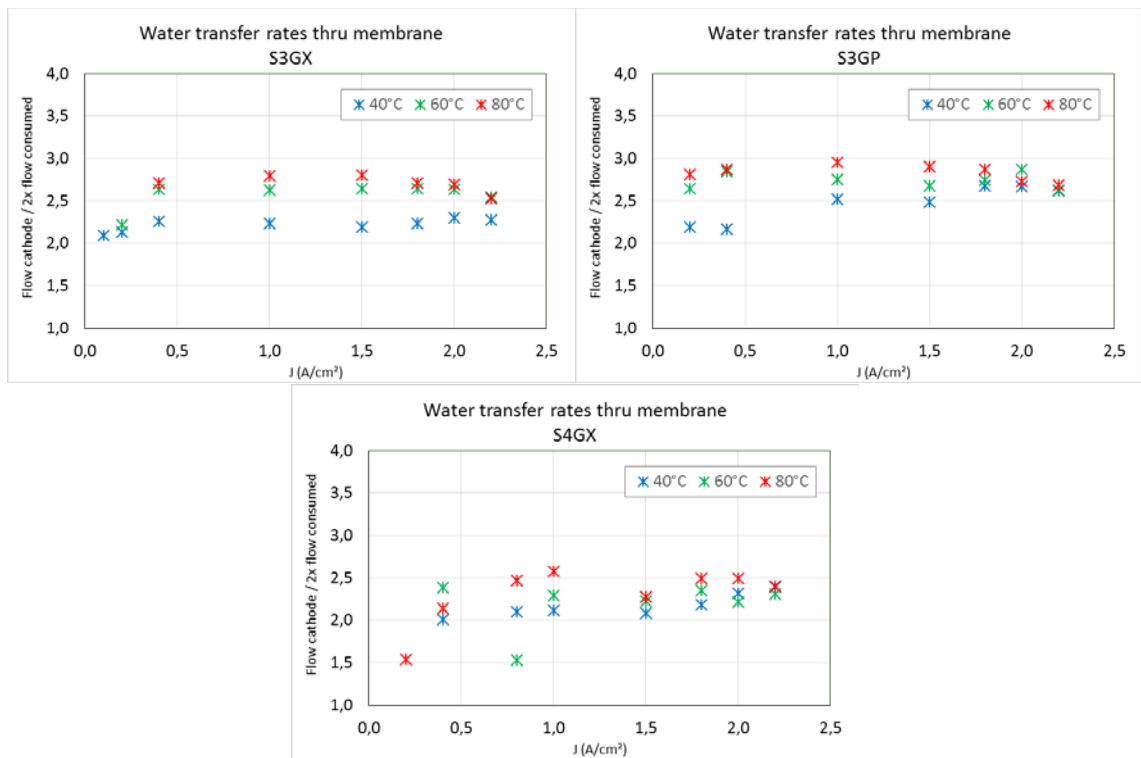


Figure 39: Water transfer rate for sinters 3 and 4 at different temperatures and with different meshes configurations.

We can observe on these figures that:

- The water transfer rates increase slightly with the current density until 0.5A/cm². Then, they roughly remain constant.
- The averaged amplitudes of these plateaus depend on the temperature: higher is the temperature, higher is the transfer rate.
- It depends also on the cell configurations:
 - o Using the sinter 3, the transfer rate is slightly higher when the meshes are parallel than when they are perpendicular.
 - o The transfer rate is lower for sinter 4 compared to sinter 3.

We can conclude that the diffusion process plays a role and/or the electro-osmosis coefficient varies. But it is not possible to discriminate between these 2 mechanisms at this step. The use of models can help to analyze deeper these results, as will be done further (see 4.2).

3.1.3 PEIS measurements

Potentiostatic impedance spectroscopy were performed at various potential. The frequency range was set from 100 mHz to 100 kHz with 12 points/dec. The amplitude was varied from 10 mV for the low voltage range (1.4 V < E < 1.6 V) then 50 mV in the mid voltage range (1.6 V < E < 1.8 V) and 100 mV in the high voltage range (> 1.8V). The PEIS have been performed for the 3 cell configurations, for the 3 temperatures, for various pressures and for various imposed potential. Figure 42 gives an example of the obtained result.

FREE DISTRIBUTION

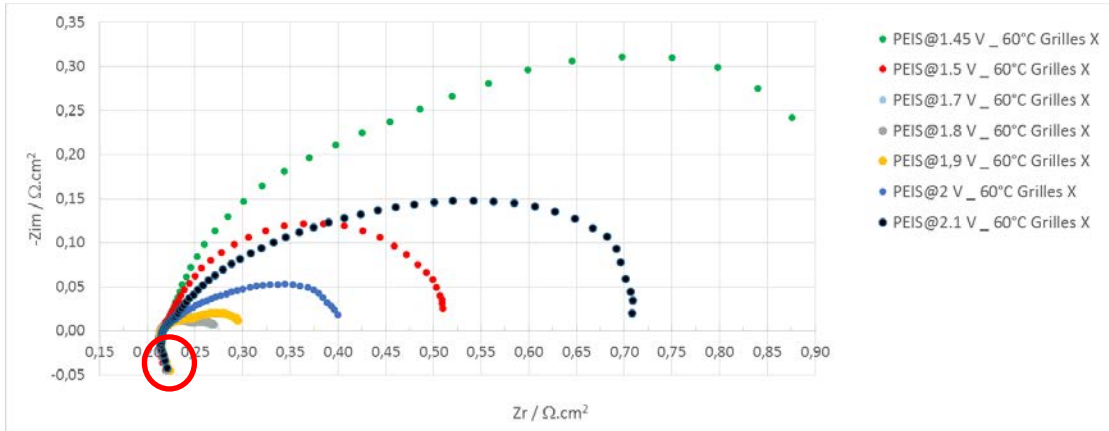


Figure 40: PEIS at 60°C, 1 bar on both sides with sinter 3 and perpendicular meshes.

The total cell ohmic resistance can be extracted from each curves. It corresponds to the intercept on X-axis of the Nyquist representation of the impedance spectra (real axis). This resistance includes ionic membrane resistance, electric resistance such as interface contact resistance and bulk component resistance. The ohmic resistances have been plotted versus current density for the 3 cell configurations and the 3 temperatures (Figure 43).

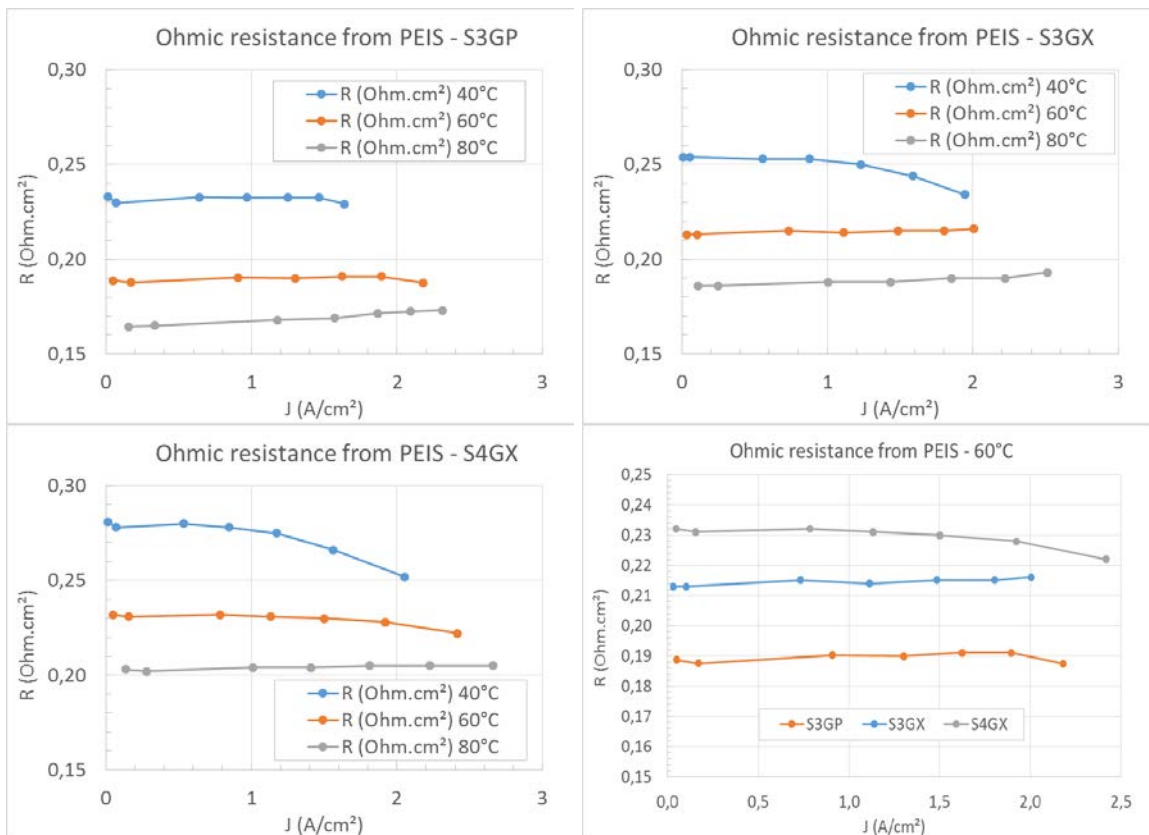


Figure 41: Ohmic resistances from PEIS.

From these graphs several conclusions can be drawn:

FREE DISTRIBUTION

- As expected, the ohmic resistance decreases significantly when temperature increases (the membrane resistance decreases with temperature increase).
- The resistance is roughly constant when the current density increases except at 40°C where a significant decrease is observed above 1A/cm². It is probably due to an internal temperature increases induced by the reaction generated heat. This phenomena is not observed at higher temperatures since the generated heat is then not sufficient to increase the temperature to the wanted value and an electrical heater is used for this purpose.
- The resistance values depend strongly on the cell configuration as shown on the last figure Parallel meshes with sinter 3 configuration has the lowest resistance then, comes the sinter 3 with perpendicular meshes and finally the sinter 4 with perpendicular meshes configuration has the higher resistance. This observation is coherent with the electrical resistance measurements (section 2.2.6): the sinter 3 has a lower resistance than the sinter 4 and the perpendicular meshes have a lower contact resistance than the parallel one (Figure 8).

3.1.4 Polarization curves

The first results have been obtained at 1bar for 3 temperatures: 40°C, 60°C and 80°C. Then some preliminary results have been obtained at slightly higher pressure values: until 8 bar at 60°C. The pressure is actually limited to this value on the bench but this limit will be enhanced soon.

Atmospheric pressure results

The 9 polarization curves are plotted on Figure 44 using the following convention: blue curves correspond to 40°C, green ones to 60°C and red ones to 80°C. Light colors correspond to parallel meshes (P) and dark ones to cross mesh position (X). Solid lines correspond to sinter 3 and dashed lines to sinter 4.

FREE DISTRIBUTION

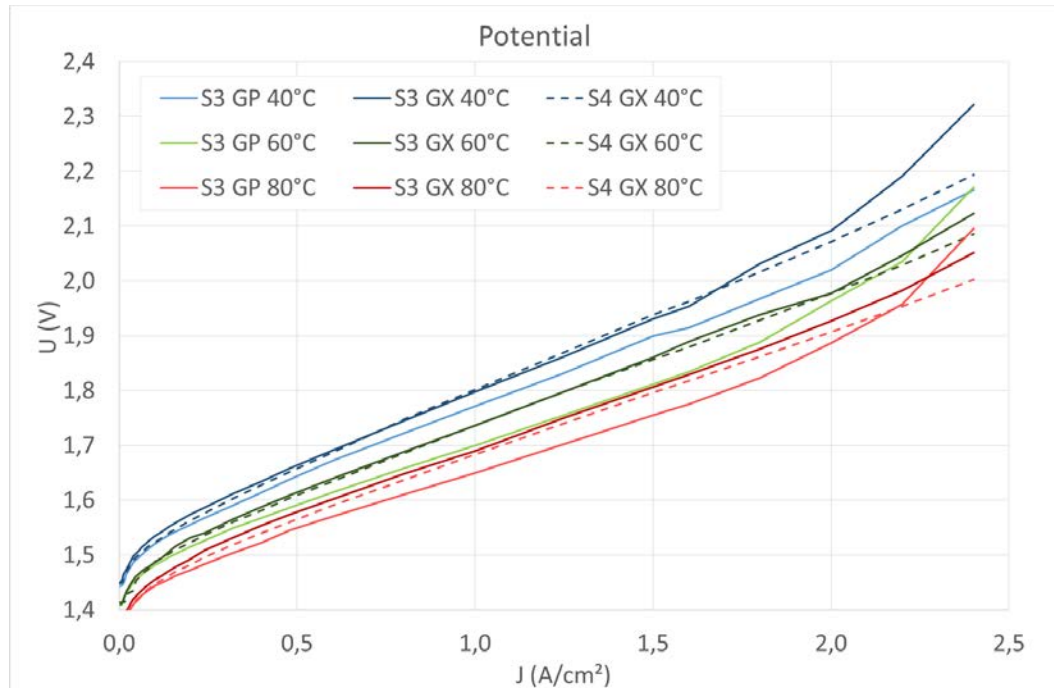


Figure 42: polarization curves at 1bar and 40°C, 60°C and 80°C for the 3 cell configurations

The conclusions that can be drawn from these curves are:

- The increase of temperature leads to decrease the cell potential as expected. This is coherent with the decrease of the membrane ohmic resistance with increasing temperature.
- The sinter 3 with parallel meshes on the anode side has a lower potential than the 2 other configurations for current densities lower than 2A/cm² at given temperature.
- The sinters 3 and 4 with cross meshes have very close values of potential for current densities lower than 2 A/cm².
- For current densities higher than 2A/cm², most of the curves, except the sinter 4 ones (dashed lines), highly increase. This sudden change in their slope is known as the limit of mass transfer: the energy requested to perform the reaction has a sudden increase that comes from the increasing difficulty to provide enough water to the catalyst layer.
- The limit of mass diffusion depends strongly on the cell configuration. It is especially visible with the parallel meshes configuration with sinter 3. It is less important for the cross meshes and sinter 3. It is negligible, at least below 2.4 A/cm², for the sinter 4.
- The sinter 3 with parallel meshes, which is the more efficient configuration, has a degraded behavior at high current densities due to the limit of mass transfer that is reached earlier than for the other configurations.

Higher pressure results

On the figures, Pa stands for anode pressure in bar and Pc for cathode pressure.

FREE DISTRIBUTION

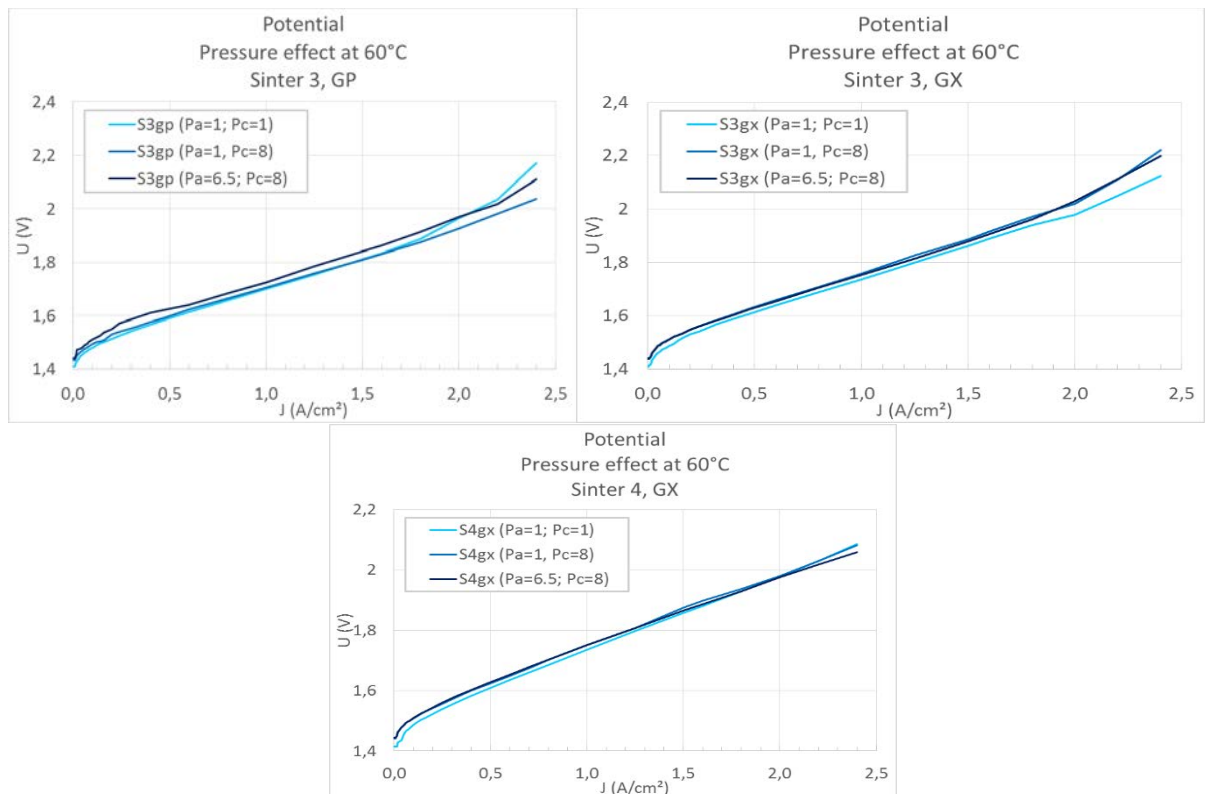


Figure 43: Effect of pressure on the polarization curves.

The effect of increasing pressure at current density lower than 2A/cm^2 is clearly a slight increase of the potential that is coherent with, at least, the reversible potential dependence on pressures (see 4.4.1). Then at higher current, except for the sinter 3 with cross meshes, the mass transfer limit is shifted to higher current density values. The classical explanation in literature is the bubble size reduction due to the pressure increase. But this phenomena is expected to occur essentially at the anode where bubbles can impeded the water distribution. In the present situation, the pressure effect seems to be similar on both anode and cathode. Moreover, on the sinter 3 with parallel meshes configuration, the shift of mass diffusion limit is higher when pressure is increased at the cathode. These observations lead us to consider that mass transfer limitation is not a problem located only on the anode side where counter-current flow can occurs in the sinter. This point should be revisited with higher pressures tests.

3.2 Experiments performed at Fraunhofer

3.2.1 Cell and test bench description

For the in-situ measurement a high-pressure electrolysis test cell was used with an active area of 25cm^2 . The cell is made of titanium material and designed to test different components of an electrolysis cell such as MEAs, sinters and meshes. In these measurements the investigated sinters are placed at the anode and cathode side of the cell between one mesh and the MEA.

FREE DISTRIBUTION

The provided sinter 3 and sinter 4 are characterized in a fully automated test bench. Using this test setup, electrolysis cell can be operated at temperature of 20 °C to 80 °C, at balanced pressure of 0.5 to 50 barg and at water flow rate from 0.2 to 1.5 l/min through each half cell. The power electronics are able to deliver a maximum current of 200 A, which corresponds to a maximum current density of 8 A/cm² for an active cell area of 25cm². The test bench contains two water circulation loops on either side. The anodic water circulation corresponds to blue and cathode to red in Figure 46. These loops are heated by an additional heating system which is shown in green in Figure 46.

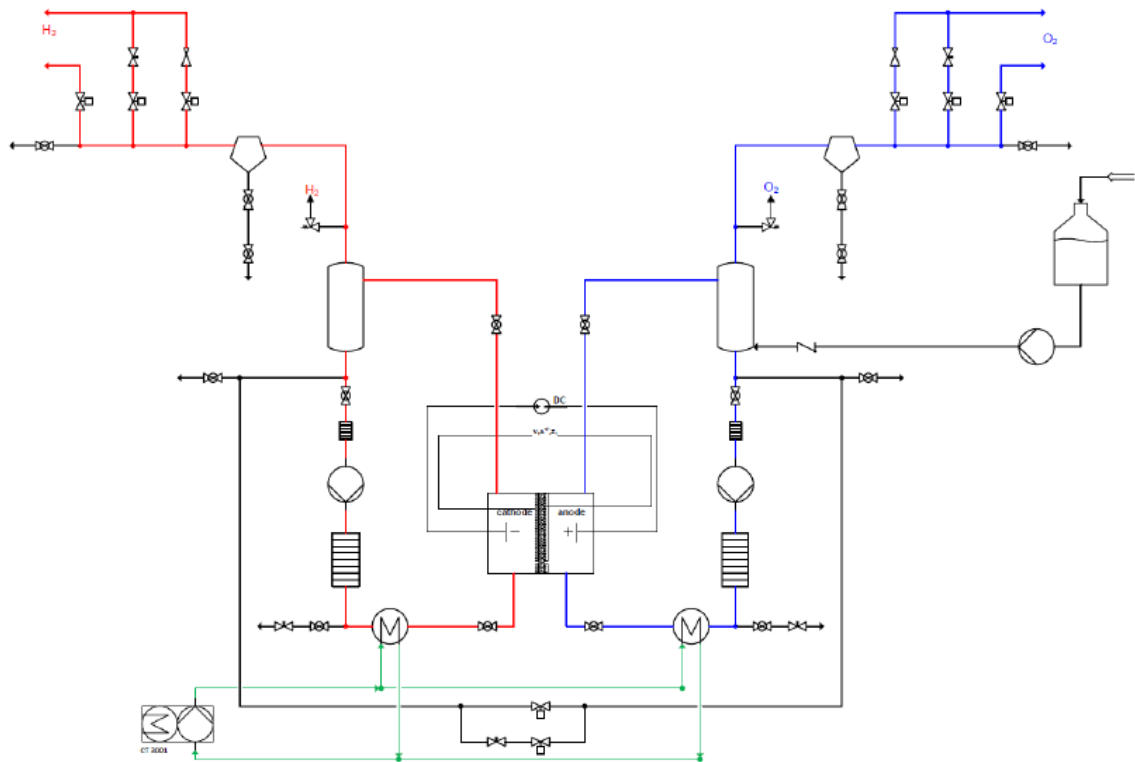


Figure 44: Simplified P&ID of the high pressure PEM electrolysis test bench

Active cell area	25cm ²
Cathode/anode	ITM sinter
MEA	Commercial CCM based on N117
Mesh configuration	One mesh

Table 15: Fraunhofer cell configuration

Pressure (barg)	1/2/5/10/30
Water flow rate (l/min)	0.2/0.3/0.4/ 0.5 /0.6/0.8
Temperature (°C)	40/ 60 /80

Table 16: used testing conditions at Fraunhofer (bold letters indicate the base line)

FREE DISTRIBUTION

3.2.2 Polarization curves

Polarization curves for the sinter 3 and sinter 4 are acquired after performing an internal break-in protocol for MEA conditioning. The conditioning process was conducted at 80 °C, 1 barg and 0.5 l/min at 1 A/cm² and 2 A/cm² by holding at each current density for 30 minutes (repeating this alteration 12 times). Polarization curves are obtained at different pressures, temperatures and water flow rates.

Pressure dependency

Pressure dependency on polarization curves of sample-03 (sinter 3) and sample-04 (sinter 4) are shown in Figure 48 at constant water flow rate of 0.5 l/min and temperature of 60 °C the circular marker in graph corresponds to sample-03 and triangular to sample-04; each color indicates same condition for both samples. In general sample-03 performs better than sample-04, which is confirmed by ex-situ results of through plane permeability and pore size measures. Since sample-03 has comparatively bigger pore sizes and higher through plane permeability than sample-04, gas removal process from the catalyst layer to the mesh is improved and consequently mass transport limitation is reduced. An increase in pressure from 1 to 2 barg affects the polarization curve negatively as expected from Nernst equation. However, any further increase in pressure after 2 barg reduces the cell voltage slightly for both the samples, but still 30 barg polarization curves remain at higher cell voltage than the 1 barg polarization curve. (Please keep in mind here that maximum allowed cell voltage is 3.5 volts). For sample-03, mass transport limitation starts to dominate from 3.25 A/cm². For sample-04, it seems that contribution of ohmic resistant is significant. However, there could also be a mass transport limitation.

Temperature dependency

Polarization curves measured at different temperatures are presented in Figure 49 (at 0.5 l/min of flow rate and 1 barg of pressure). As expected, an increase in temperature reduces the cell voltage. The conclusion made in pressure dependency is valid here as well that the sample-03 works better than sample-04.

FREE DISTRIBUTION

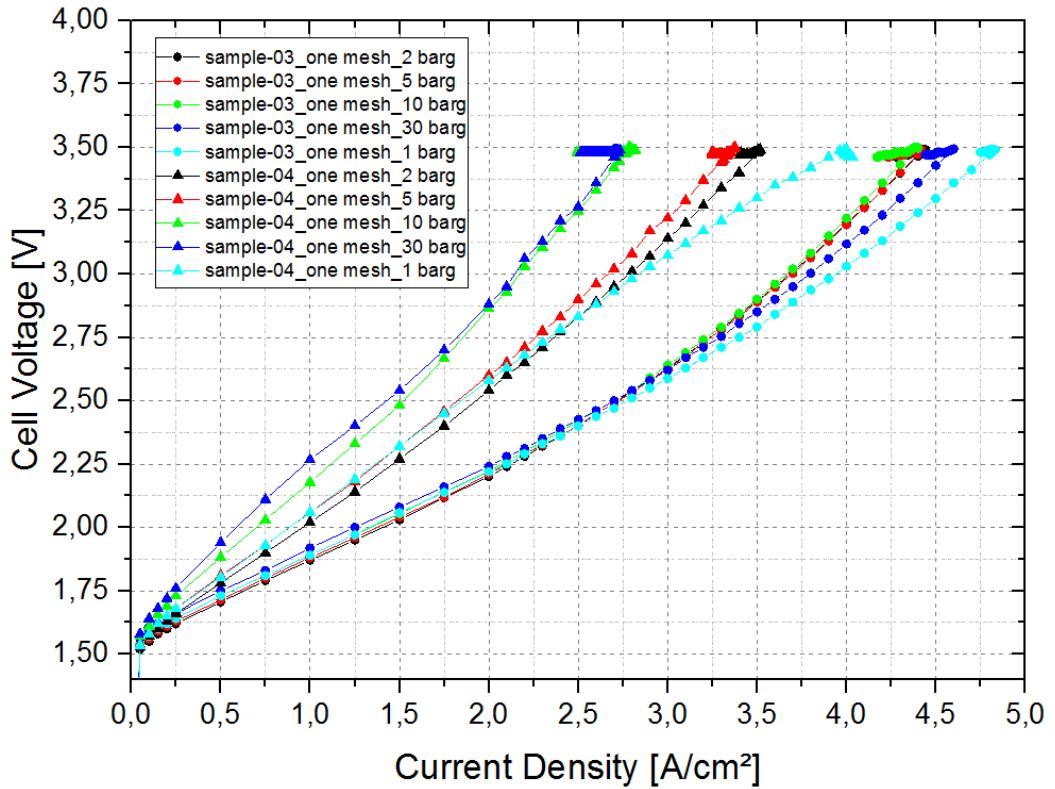


Figure 45: Polarization curve of sample-03 (sinter 3) and sample-04 (sinter 4) at different pressure

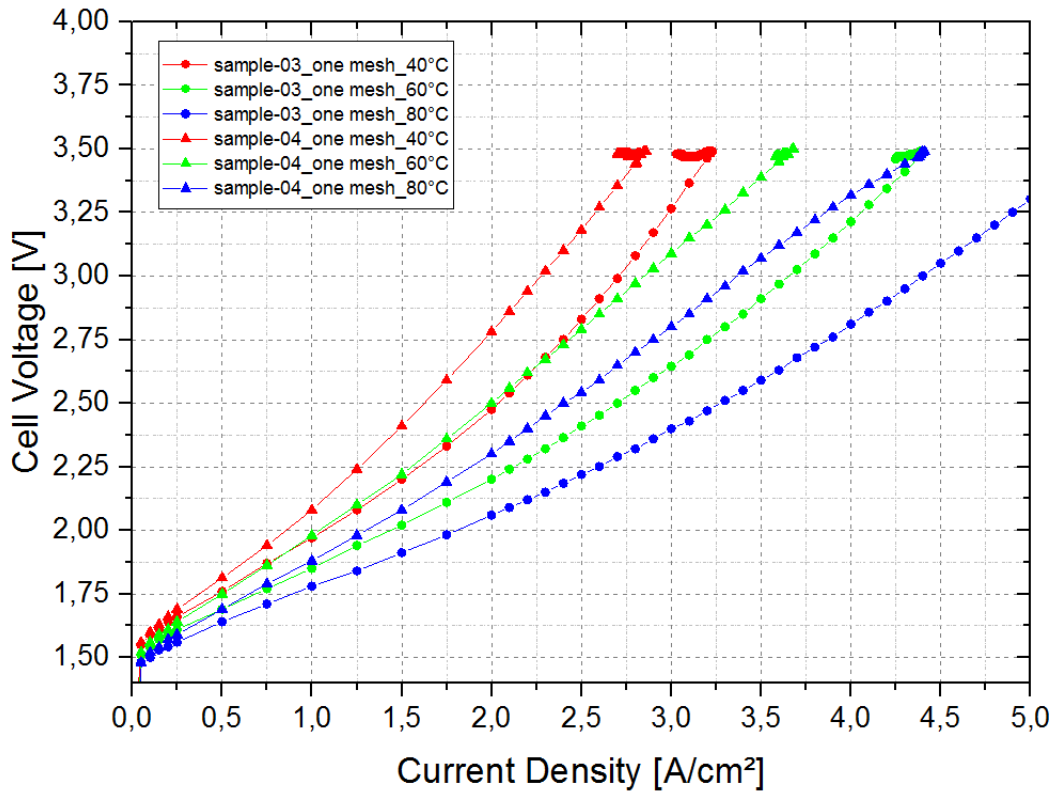


Figure 46: Polarization curve at different temperatures for sample-03 and sample-04

FREE DISTRIBUTION

Flow rate dependency

The acquired polarization curves at different flow rates (at 60°C and 1 barg) are shown in Figure 50. For sample-03 an influence of different flow rate cannot be observed. Whereas, for sample-4, a negative influence of increasing flow rate is recorded.

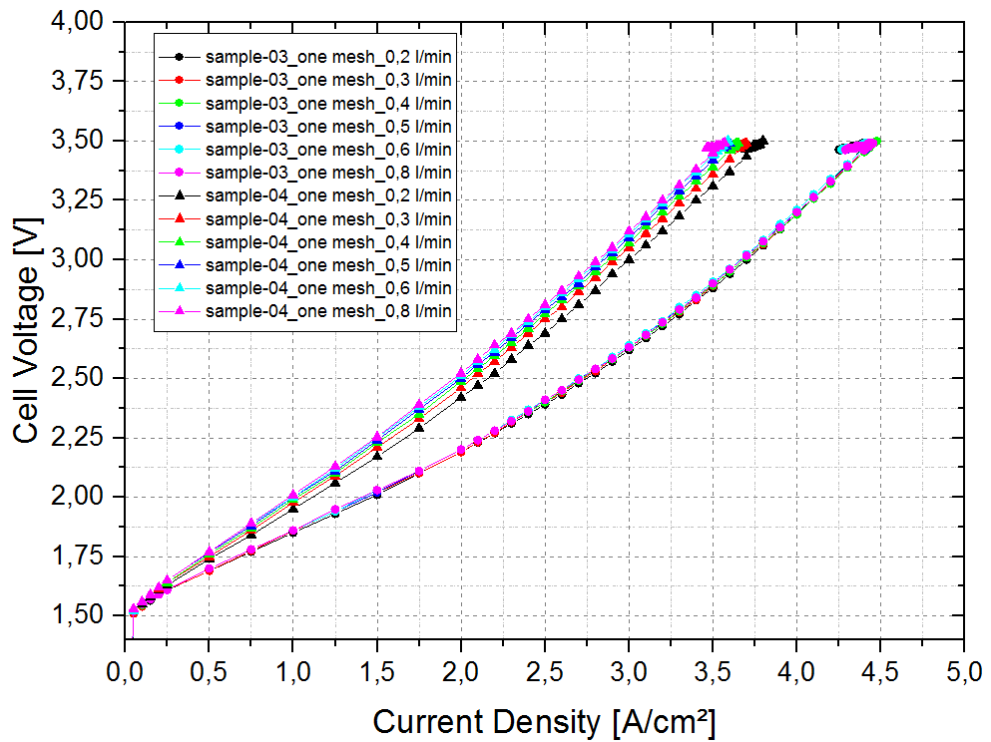


Figure 47: Polarization curves for sample-03 and sample-04 at different flow rates.

FREE DISTRIBUTION

4. ELEMENTARY PHYSICAL AND ELECTROCHEMICAL LAWS

This chapter describes the elementary laws deduced from experimental results that will be implemented in the simulation stack code (chapter 0).

4.1 Capillary pressure model

The liquid water motion in porous media such as the sinters, is driven essentially by the capillarity. Thus a capillary pressure law is requested for the model. Capillary pressure measurements have been performed at Fraunhofer using ITM sinters and two different liquids: water and Porefil (2.2.4). In this paragraph two different models have been developed: at CEA using the Porefil data and at Fraunhofer using the water data. They are described in the following sections.

4.1.1 General approach for modelling

The capillary pressure of a bubble writes:

$$P_C = \frac{2\gamma}{R}$$

Where γ is the surface tension and R the curvature radius of the bubble.

In more complex situations with porous solid, this expression has been generalized using additional parameters:

- the microstructure of the porous media that is characterized by a length scale L linked the pore size,
- the interaction between the liquid and the gas using the surface tension γ ,
- the interaction between the liquid and the surface of the porous medium that is characterized using the contact angle θ ,
- The quantity of liquid inside the porous medium that is characterized using a function of the liquid saturation s that is called the Leverett function J(s). This function highly depends of the porous medium microstructure and has to be fitted using experimental data.

The capillary pressure is expressed as follows:

$$P_C = \frac{\gamma \cos \theta J(s)}{L}$$

Where L and J(s) have to be determined empirically. L is related to the pore size and J(s) is built from the measured capillary pressures that are non dimensionnalized using the following expression:

$$J_{exp} = \frac{P_C L}{\gamma \cos \theta}$$

J(s) is thus a function that fits J_{exp} .

4.1.2 Capillary pressure model based on Porefil results

The measurements obtained using Porefil liquid at Fraunhofer are numerous and seem to be more accurate than water ones, thus, they are used to build a Leverett function at CEA.

For Porefil, the properties are presenter on Table 18:

FREE DISTRIBUTION

Chemical nature	perfluoroether
Surface tension	16 mN/m
Contact angle	~ 0

Table 17: Porefil properties found on www.porometer.com/porometers/wetting-liquids

For granular porous media the length scale is generally defined as: $L = \sqrt{\frac{K}{\epsilon}}$

Where K is the permeability (m²) and ε the porosity.

For the studied sinters (which are not granular media) this length scale leads to widely dispersed data as illustrated on Figure 51.

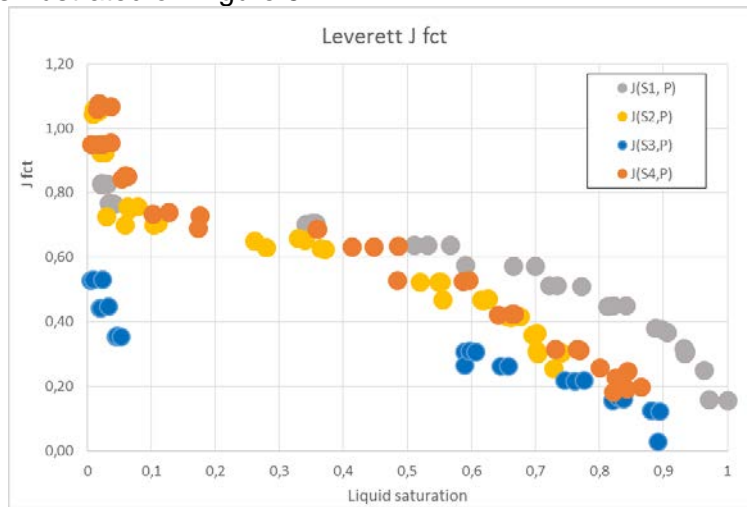


Figure 48: Leverett J-function using classical length scale

Since the median and the mean radius pore are known (See Table 6), one of them can be used as a length scale. Both have been tried and only the median one gives good results. The complete expression of the new length scale is:

$$L = \frac{R_{mp} \epsilon}{2}$$

Where R_{mp} is median radius pore and ε the porosity (obtained using the gas pycnometer – see Table 6).

Plotting J_{exp} leads to a cloud of data points that are aligned along a single curve: the experimental Leverett function as illustrated on the Figure 52. Then it is easy to build an analytical J-function that fits the J_{exp} data: this is the black solid line on the same graph. The analytical expression for the fitting J-function has been obtained using three terms. Each of them gives the trend for a part of the curve. The final expression writes:

$$J_{model}(s) = \left[\frac{2,2 - 1 + \exp(-16s)}{2.2} \right] \exp \left[-\frac{3}{2} s^5 \right] [2 - 0.65 \exp(s^{10})]$$

Where s is the liquid volumetric fraction also called liquid saturation.

To build this function, the first step consists in developing an expression that fits the first part the curve: **the left sharply decreasing part for low s values on the left**, then it is multiplied by

FREE DISTRIBUTION

another expression that modify the shape of the plateau in the middle and finally a third expression is found for the final slowly decreasing part for high s values on the right. This is of course an iterative process. Several attempts to use a more simple polynomial expression have failed.

Using the J_{model} function and the new length scale L it is now possible to calculate the capillary pressure in our models as a function of the liquid fraction s :

$$P_c = \frac{\gamma \cos \theta}{L} J_{model}(s)$$

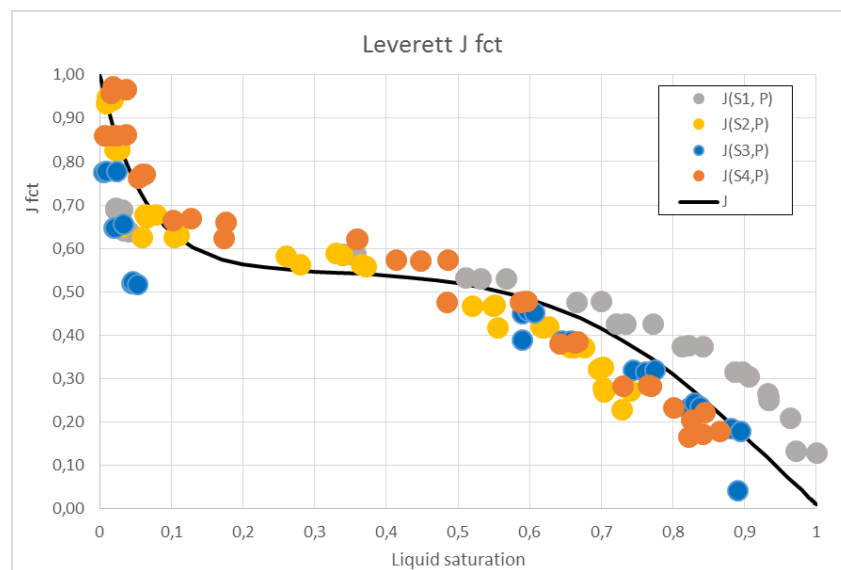


Figure 49: Leverett J-function with new length scale

4.1.3 Using water results

The experimental results for water were used at FRAUNHOFER to calculate an approximation curve using following equation and parameters given in table below:

$$p_{cap} = p_{max} * (0.5 - 0.5 * \tanh(a * (s_{measured} - s_{mid})))$$

p_{cap}	[Pa]	capillary pressure measured in full porometry
p_{max}	[Pa]	maximum value of p_{cap} at low saturation
a	[-]	fitting factor
$s_{measured}$	[-]	liquid saturation measured in full porometry
s_{mid}	[-]	liquid saturation at measured $p_{cap} = 0.5 * p_{max}$

	sinter 1	sinter 2	sinter 3	sinter 4
p_max [Pa]	40.000	39.750	9.000	37.500
s_mid [-]	0.72	0.625	0.6	0.53
a	8	15	50	10

Table 18: Parameters used to calculate approximation curve

FREE DISTRIBUTION

The used equation fits the experimental data well. The fitted curves are given in Figure 29. In spite the equation is no common capillary model it is used in the modeling work at MEA scale (at Fraunhofer) because of quite good convergence behavior.

4.2 Water permeation through the membrane

The water flow through the membrane is induced by two mechanisms:

- the electro-osmosis drag that is proportional to the current but with an uncertain coefficient that might depend on the membrane water content
- the diffusion flux that depends on both a coefficient that involves temperature and membrane water content, and the water content gradient through the membrane.

The measurements that have been performed during the project give the total flowrate through the membrane (see 3.1.2) thus, it is not possible to validate independently the models for these two mechanisms. Using the experimental data from the Novel project at the beginning of the project, two models have been identified for these phenomena (Serre, 2016):

- Zawodzinski (1995) law for electro-osmosis coefficient a_{eo} :

$$\text{Electro-osmosis flux: } F_{H_2O} = \frac{J}{F} a_{eo}$$

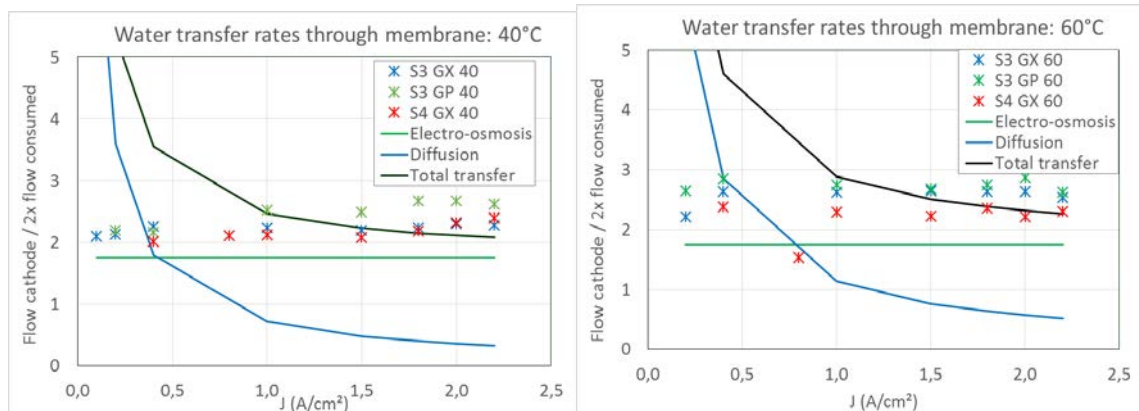
$$\text{Coefficient: } a_{eo} = \begin{cases} 1 & \text{if } \lambda \leq 14 \\ 0.1875 \lambda - 1.625 & \text{if } \lambda > 14 \end{cases}$$

- The Zawodzinski *et al.* (1991) law for the water diffusion coefficient D_{H_2O} :

$$\text{Diffusion flux: } F_{H_2O} = D_{H_2O}(\lambda, T) \frac{Q_{sec}}{EW} \nabla \lambda$$

$$\text{Diffusion coefficient: } D_{H_2O} = (6.707 \cdot 10^{-8} \lambda + 6.387 \cdot 10^{-7}) \exp\left(-\frac{2416}{T}\right)$$

On the following graphs, the red stars correspond to the experimental data, the green line to the electro-osmosis flux, the blue one to the diffusive flux and the black one to the sum of the two contributions. The membrane water content that is unknown for this experiment has been fixed to constant values: 22 on the membrane anode side and to 14 on the cathode side. Thus only temperature varies on the curves for model on the following figures. The cell configuration is not taken into account in these models.



FREE DISTRIBUTION

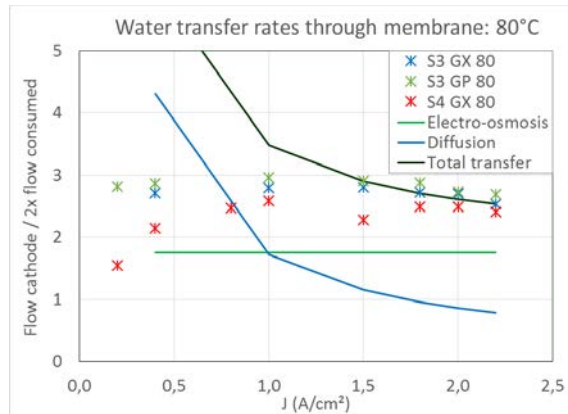


Figure 50: Water transfer rate through membrane: model validation.

From these graphs, we can conclude that the Zawodzinski laws for electro-osmosis and diffusive flux give accurate results when the current density is higher than 1A/cm² but overestimate the flux at lower currents. This overestimation could come from several origins:

- Errors in the measurements at low current as already mentioned.
- A not accurate diffusion model.
- A wrong choice of the water content values (λ) for evaluating the coefficients and gradients. If the membrane water content gradient is lower than expected, the diffusion will become quite less important. A complete calculation with the code will give more precise values of the water content everywhere in the cell and thus, the flux calculations will be more realistic. As an example, we have calculated the water flux assuming a water content constant through the membrane and equal to 22. It leads to the following curves (Figure 54) that are surprisingly very close to the experimental ones. Thus it is as if there were no diffusion and a high value of water content on both side of the membrane which was not expected a priori.

FREE DISTRIBUTION

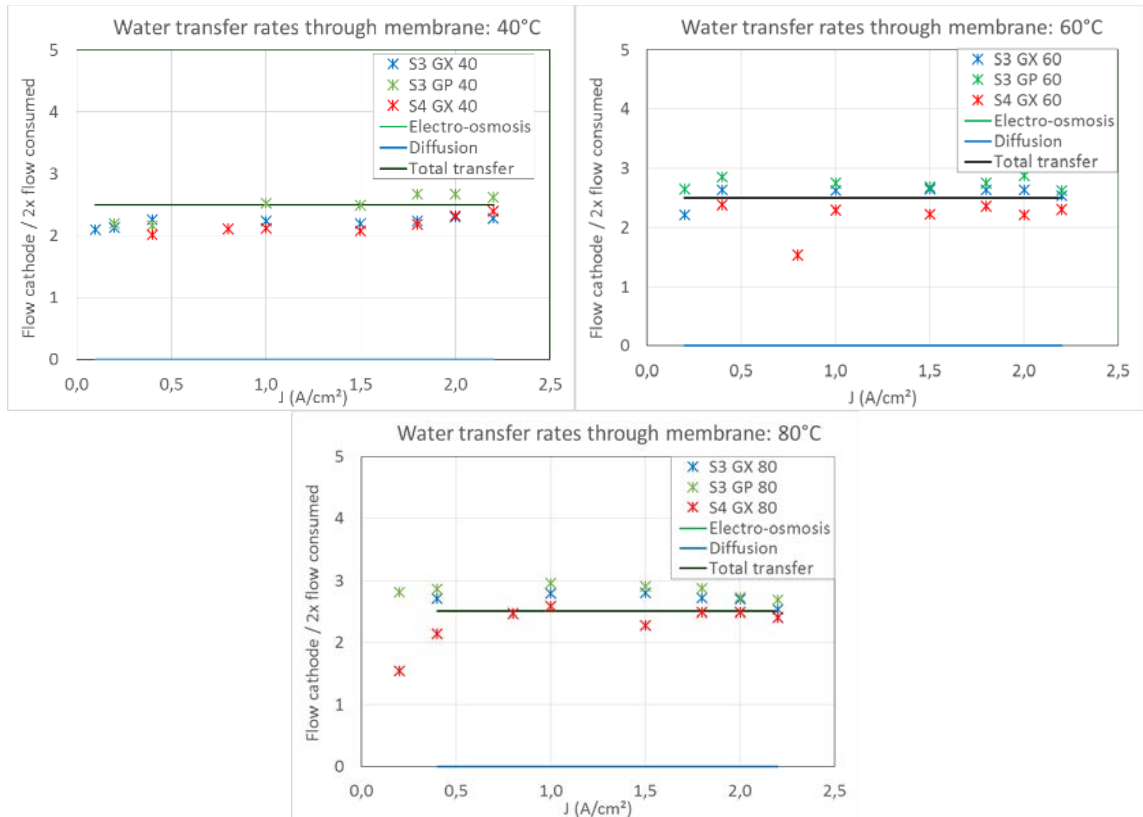


Figure 51: Water transfer rate through membrane for a hypothetical constant membrane water content equal to 22.

4.3 Ohmic resistance

The ohmic resistance R_{Ω} of the cell is the sum of contact resistances which have been measured as function of contact pressure (see 2.2.6) and of the membrane resistance that can be calculated using the Springer model (1996). The bulk resistances of mesh and sinter can be neglected since contact resistances are several order of magnitude larger (see 2.2.6). The total ohmic resistance has been measured using PEIS (see 3.1.3). These three data sets allow to check the coherence of the various data.

The Springer model (1996) writes:

$$\sigma_m = (33.75 \lambda - 21.41) \exp\left(-\frac{1268}{T}\right)$$

In order to estimate the cell contact resistance using data from section 2.2.6, the value of the contact pressure of the CEA must be known. Since it is not measured we estimate it from the torque $T=8\text{N.m}$, the screw size $d=6\text{mm}$, the friction coefficient: $C_f=0.2$ for steel and the total cell surface $S=11^2 \text{ cm}^2$. The contact pressure P_c is then estimated to be 0.55 MPa from the expression:

$$P_c = \frac{T}{C_f d S}$$

FREE DISTRIBUTION

We must keep in mind that the friction coefficient might not be very accurate since it depends on the screw wear.

The membrane resistance values calculated using the Springer model (with water content set to 22 since this value gives accurate membrane water flux, see Figure 54) are subtracted from the PEIS ohmic resistances. The resulting values are then averaged for the three temperatures, giving the contact resistances of the cell at 0.55 MPa for the three geometrical configurations (colored circles). The values are plotted together with the data given in section 2.2.6 (black squares and crosses), on the Figure 55. From this figure it is clear that the values obtained from EIS and Springer model are coherent with the electrical measurements of the contact resistances. The difference found between these two methods concerns the difference of the contact resistances linked to the two different assembling positions of the meshes (parallel, or crossed). This difference is clearly negligible when measured with electrical device while it is not using EIS. Both methods have uncertainties especially the electrical one, as observed on the various figures of the section 2.2.6. Thus, the EIS resistance values will be used for the model development. This is coherent with the use of the Springer model in the code.

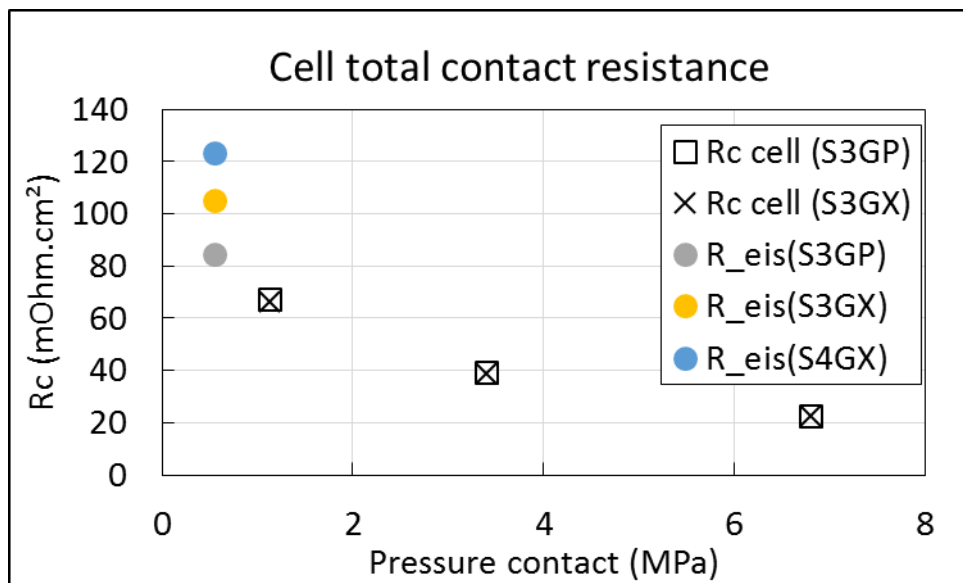


Figure 52: Ohmic resistances: comparison

4.4 Electrochemical law

The total potential of one electrolyzer's cell writes:

$$U = E_{rev} + \eta_A + \eta_C + R_{\Omega} J$$

Where E_{rev} is the reversible potential, η_A and η_C are the anodic and cathodic overpotentials, R_{Ω} is the total ohmic resistance (electric and protonic) and J the current density.

FREE DISTRIBUTION

To obtain the overpotential $\eta_A + \eta_C$ in order to develop an electrochemical model we first determine the reversible potential E_{rev} using Nernst law and then, we subtract from the measured cell potential, the reversible potential and the ohmic potential $R_\Omega J$ using the ohmic resistance determined thanks to PEIS.

4.4.1 Reversible potential

The reversible potential is a function of enthalpy variation ΔH , entropy variations ΔS , perfect gas law constant R , number of electron $n=2$, Faraday constant F , temperature T and activities a :

$$E_{rev} = \frac{\Delta H - T\Delta S}{nF} + \frac{RT}{nF} \ln \left[\frac{a_{H_2} a_{O_2}^{1/2}}{a_{H_2O}} \right]$$

Since, we want to be able to capture pressure effects on the electrochemical performance, we do not neglect anymore the contribution related to water and gas activities. The gas activities are defined as the gas partial pressure divided by the reference pressure at which the enthalpy of the reaction has been determined, 1 bar in the present case:

$$a_{H_2} = \frac{P_{H_2}}{P_{ref}} \text{ and } a_{O_2} = \frac{P_{O_2}}{P_{ref}}$$

Where the gas partial pressures are expressed in Pa and $P_{ref} = 10^5 \text{ Pa}$. The hydrogen and oxygen partial pressures are lower than 10^5 Pa since vapor is present. Preliminary calculations have shown that vapor partial pressure is very close to saturation. Thus $P_{vap} = P_{sat}(T)$.

For the water, the definition of the activity is more complex:

$$a_{H_2O} = \begin{cases} 1 & \text{for liquid} \\ \frac{P_{vap}}{P_{sat}} & \text{for vapor} \end{cases}$$

This definition of the activity is coherent with an enthalpy variation determined for a reaction at 1 bar.

When calculating the water activity over a certain surface (a grid mesh in the simulation tool), we must take into account the local variations of water along this surface (see an example of on Figure 56). For example it is possible that this surface includes liquid water, vapor water and pure gas (oxygen or hydrogen). Thus the liquid fraction/saturation must be included in the previous formula. As a first approximation we suggest:

$$a_{H_2O} = \text{Min} \left\{ 1, f \left(s, \frac{P_{vap}}{P_{sat}} \right) \right\}$$

Where $f \left(s, \frac{P_{vap}}{P_{sat}} \right)$ is a function that will integrate spatially over one grid mesh the local variations of vapor and liquid water content.

FREE DISTRIBUTION

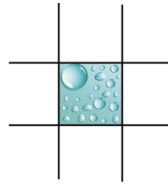


Figure 53: example of the possible spatial distribution of liquid water and vapor

4.4.2 Overpotential determination

The reversible potential and the ohmic potential obtained from the PEIS ohmic resistance determination are subtracted from the measured cell potential in order to obtain the overpotential. The following figures give the overpotential for the 3 cell configurations and the 3 temperatures at 1 bar.

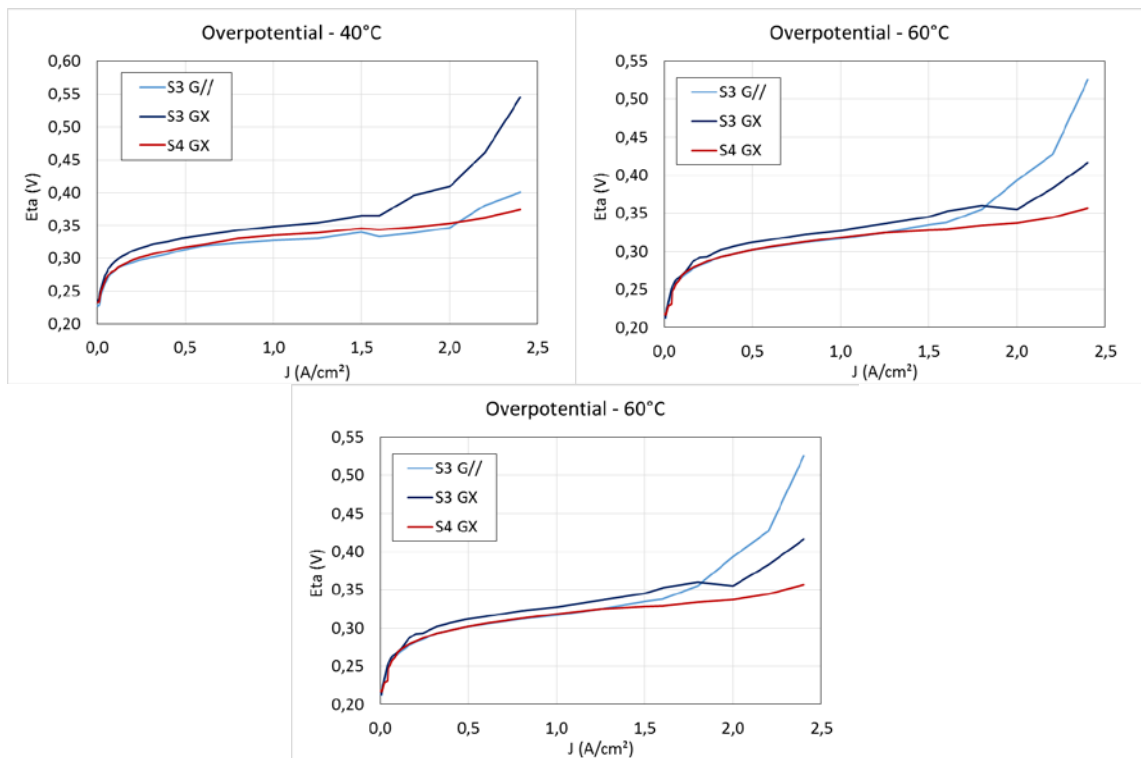


Figure 54: overpotentials for 3 cell configurations and 3 temperatures.

All the curves plotted above have been obtained with the same MEA. The differences of cell configuration (sinters and meshes) that induce different ohmic resistances are no more present here since ohmic resistance have been subtracted. Therefore, the differences observed in the curves above correspond inevitably to differences in local species concentration, which are strongly visible at high current density where mass diffusion limit is reached. These differences in local species concentration are due to the different cell configurations (both meshes and sinters).

FREE DISTRIBUTION

4.4.3 Overpotential modelling

The overpotentials are estimated thanks to a simplification of the Butler-Volmer equation at high current:

$$\eta_A \approx \frac{RT}{\alpha_A n F} \ln \left[\frac{i}{i_{0A} \gamma_A} \right] \quad \eta_C \approx \frac{RT}{\alpha_C n F} \ln \left[\frac{i}{i_{0C} \gamma_C} \right]$$

Where α_A and α_C are the transfer coefficients, γ_A and γ_C the rugosity factors and i_{0A} and i_{0C} the exchange current densities:

$$i_{0A} = n F k_{0A} T e^{-A_{0A}/RT} \quad i_{0C} = n F k_{0C} T e^{-A_{0C}/RT}$$

Where k_{0A} and k_{0C} are the rate parameters per unit surface of the reactions and A_{0A} and A_{0C} the associated activation energies.

A semi-empirical electrochemical law is used in the stack simulation tools. It depends on 5 empirical parameters that can be obtained by a classical regression methodology:

$$\eta = \eta_A + \eta_C = \beta_1 + \beta_2 T + \beta_3 T \ln(T) + \beta_4 T \ln(J) + \beta_5 J \exp\left(\frac{A_{0C}}{RT}\right)$$

The theoretical expressions of the β_i parameters have been derived from the above formulae, in the high current approximation and treating the cathodic contribution as a correction of the main anodic contribution. They write:

$$\beta_1 = \frac{1}{n F} \frac{A_{0A}}{\alpha_A} \quad \beta_2 = \frac{-R}{n F} \frac{\ln(n F \gamma_A k_{0A})}{\alpha_A} \quad \beta_3 = \frac{-R}{n F} \frac{1}{\alpha_A} \quad \beta_4 = -\beta_3 \quad \beta_5 = \frac{R}{\gamma_C k_{0C} n^2 F^2}$$

Electrochemical parameters

To obtain the electrochemical parameters requested in the beta expressions, we first assume that the cathodic overpotential is negligible in first approximation. Then, plotting the overpotential as a function of the logarithm of the current at low current values (Figure 58) straight lines are obtained whose slopes give the anodic transfer coefficient values α_A . Attention must be paid to the choice of the points that are used since the slope and thus the transfer coefficient value are very sensitive to this choice: only those that are aligned are kept. The quantitative criterion was the limit value of the correlation coefficients for a fitting straight line: this limit was set to 0.997 for the present curves.

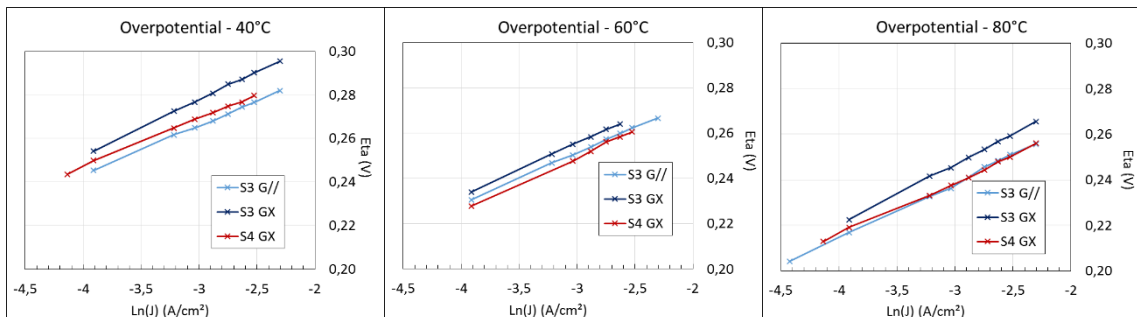


Figure 55: overpotential at low current densities.

FREE DISTRIBUTION

The obtained anode transfer coefficient is plotted versus temperature for the 3 configurations:

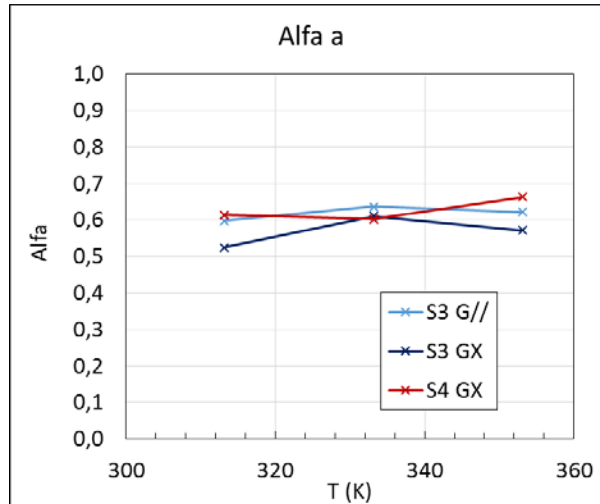


Figure 56: anode transfer coefficient.

This coefficient should be constant since it characterizes the MEA and not the other cell components. The curves show a small dispersion of its values:

$$\alpha_A = 0.60 \quad \sigma_{\alpha_A} = 0.04$$

The two last parameters that have to be determined for the anode are: k_{OA} and A_{0A} . They are determined using the same curves (Figure 58) from the values at origin for the lines which gives the exchange current density times the rugosity: $i_{0A} \gamma_A$. This product depends on the temperature since we have:

$$\frac{i_{0A} \gamma_A}{T} = \gamma_A n F k_{OA} e^{-A_{0A}/RT}$$

Starting with the following expression:

$$\ln\left(\frac{i_{0A} \gamma_A}{n F T}\right) = \ln(k_{OA} \gamma_A) - A_{0A}/RT$$

We plot the experimental values of $\ln\left(\frac{i_{0A} \gamma_A}{n F T}\right)$ as a function of the inverse of the temperature. Then we plot on the same graph the function $\ln(k_{OA} \gamma_A) - A_{0A}/RT$ looking for the couple of values of k_{OA} and A_{0A} that gives the best fit. Fortunately, the two parameters play very differently on the function so there is a unique (or nearly) couple of values that gives a good fitting.

$$k_{OA} \gamma_A = 9.8 \cdot 10^{-5} \quad A_{0A} = 36420 \text{ J/mol}$$

FREE DISTRIBUTION

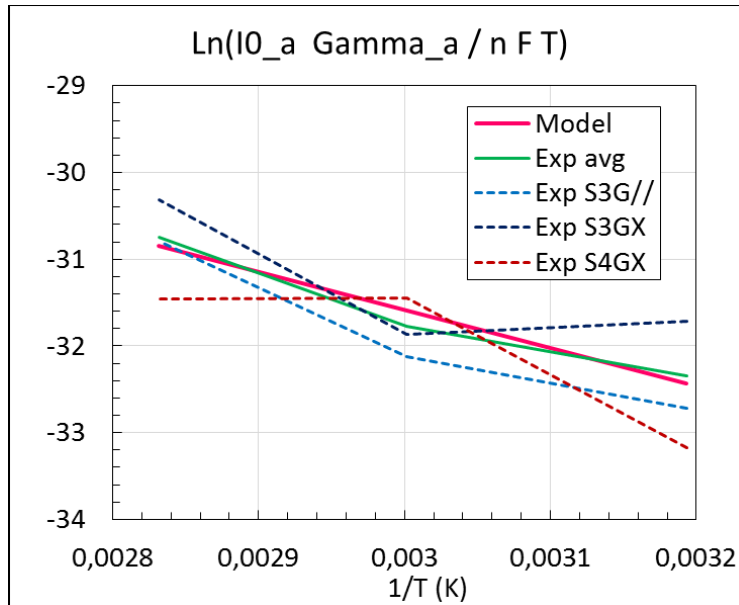


Figure 57: k_{0A} and A_{0A} determination

To determinate the cathode parameters, we first calculate the anode overpotentials using the anodic determined parameters in the previous Butler-Volmer expression. Then, we subtract these values to the global overpotential already calculated and we obtain the remaining part of the overpotential interpreted as the cathode overpotential. In fact plotting these value of the so called cathode overpotential it is clear that it can be easily neglected as illustrated on the Figure 61: the absolute value of this remaining part of the overpotential is lower than 10mV for current density lower than 1A/cm². Above this current density mass transfer limitation is known to play a significant role which is not yet taken into account. Therefore, the parameters determined previously and assumed to characterize the anode overpotential are sufficient to capture the total overpotential for low and moderate current densities. Thus the β_5 parameter is set to zero. The mass diffusion effect will be studied latter.

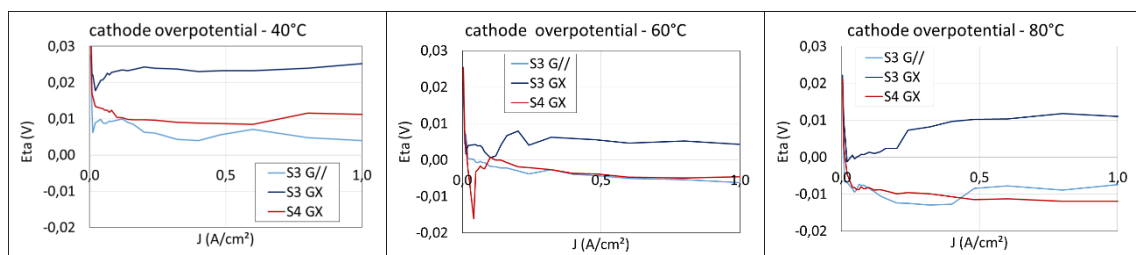


Figure 58: cathode remaining overpotential

The table below summarizes the obtained parameters:

	α_A	$k_{0A} \gamma_A$	A_{0A}
Megastack	0.6	$9.8 \cdot 10^{-5}$	36420

Table 19: Electrochemical parameters

FREE DISTRIBUTION

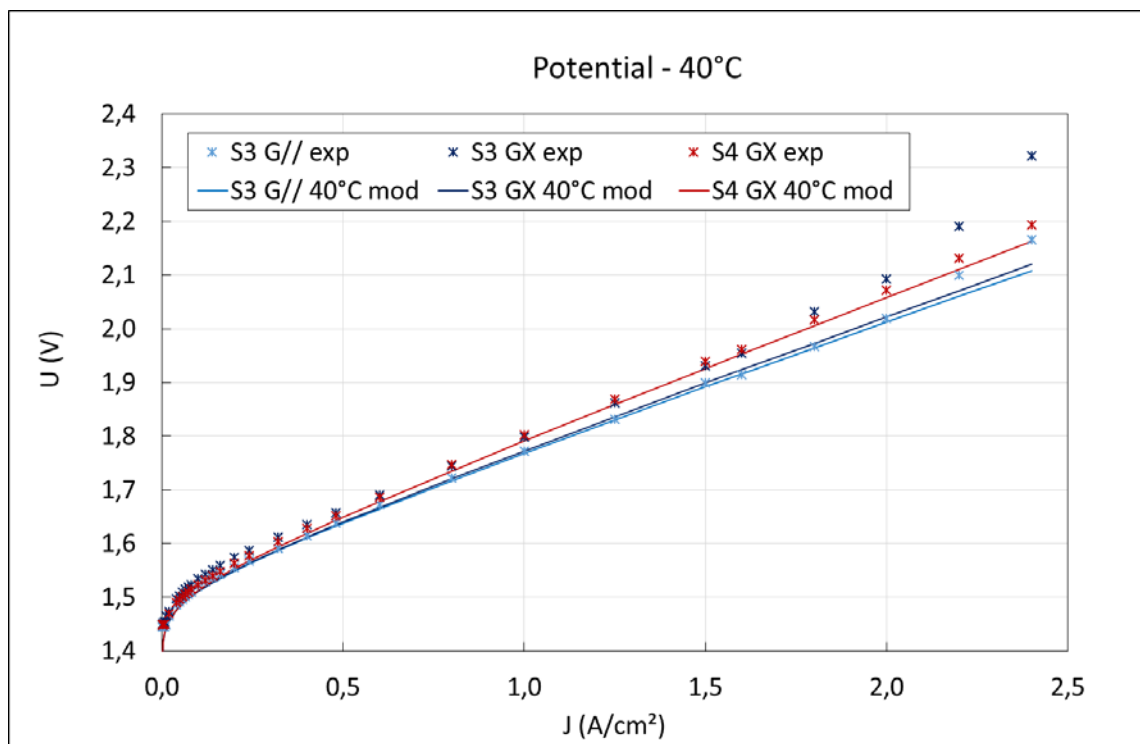
The *beta* parameters are then calculated and compared to those obtained from the Novel project and used in deliverable D2.2:

	β_1	β_2	β_3	β_4	β_5
Novel	0.501	$-7.785 \cdot 10^{-4}$	$-6.628 \cdot 10^{-5}$	$6.628 \cdot 10^{-5}$	$1.488 \cdot 10^{-10}$
Megastack	0.312	$-2.094 \cdot 10^{-4}$	$-7.122 \cdot 10^{-5}$	$7.122 \cdot 10^{-5}$	0

Table 20: beta parameters

The comparison with the values obtained using Novel's data show that the parameters are of the same order of magnitude. We also remark that the parameter β_5 was already very small for the Novel's data.

For a final validation, we compare the total measured potential to the one obtained using the measured ohmic resistance, the reversible potential assuming gas activities equal to one and the overpotential model. The plots show that the model is globally in good agreement with the data until the mass diffusion limit is reached. This is not surprising since this effect has not been modelled yet.



FREE DISTRIBUTION

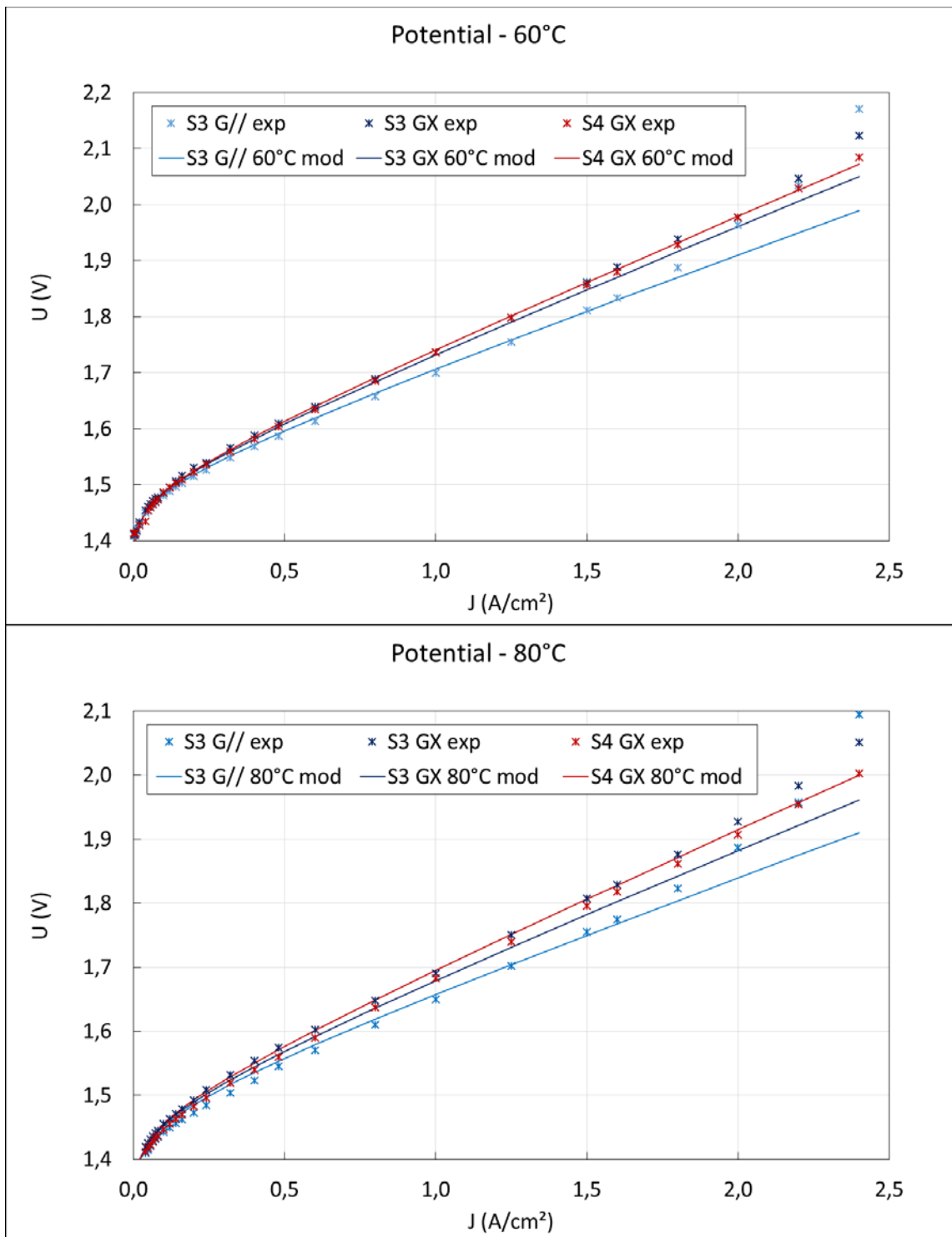


Figure 59: Validation of the electrochemical model on the experimental polarization curves at atmospheric pressure, for the three studied temperatures and the different configuration cells.

FREE DISTRIBUTION

4.4.4 The pressure effect in the electrochemical law

The pressure effect on the cell voltage appears in two parts of the electrochemical law: in the reversible potential through the activity term as already taken into account via Nernst law (see section 4.4.1) and in the overpotential term, for which a relation has to be proposed.

The overpotential of the polarization curves obtained under pressurized conditions (see Figure 45) have been calculated subtracting the reversible potential (including the pressure term) and the ohmic resistance deduced from PEIS. All the overpotential have been plotted on the same graph (see below).

The blue lines correspond to the sinter 3 with solid lines for the perpendicular meshes and the dashed lines for the parallel meshes. The green solid lines correspond to the sinter 4 with perpendicular meshes.

The pressure effect is visible on all the configurations and for all pressures on the overpotential. The sinter 4 gives the lowest overpotential. Then the sinter 3 with parallel meshes gives higher values and finally the sinter 3 with perpendicular meshes gives the highest ones (except at 1 bar). These effects have to be modelled. It will be achieved when new data at higher pressures will be available.

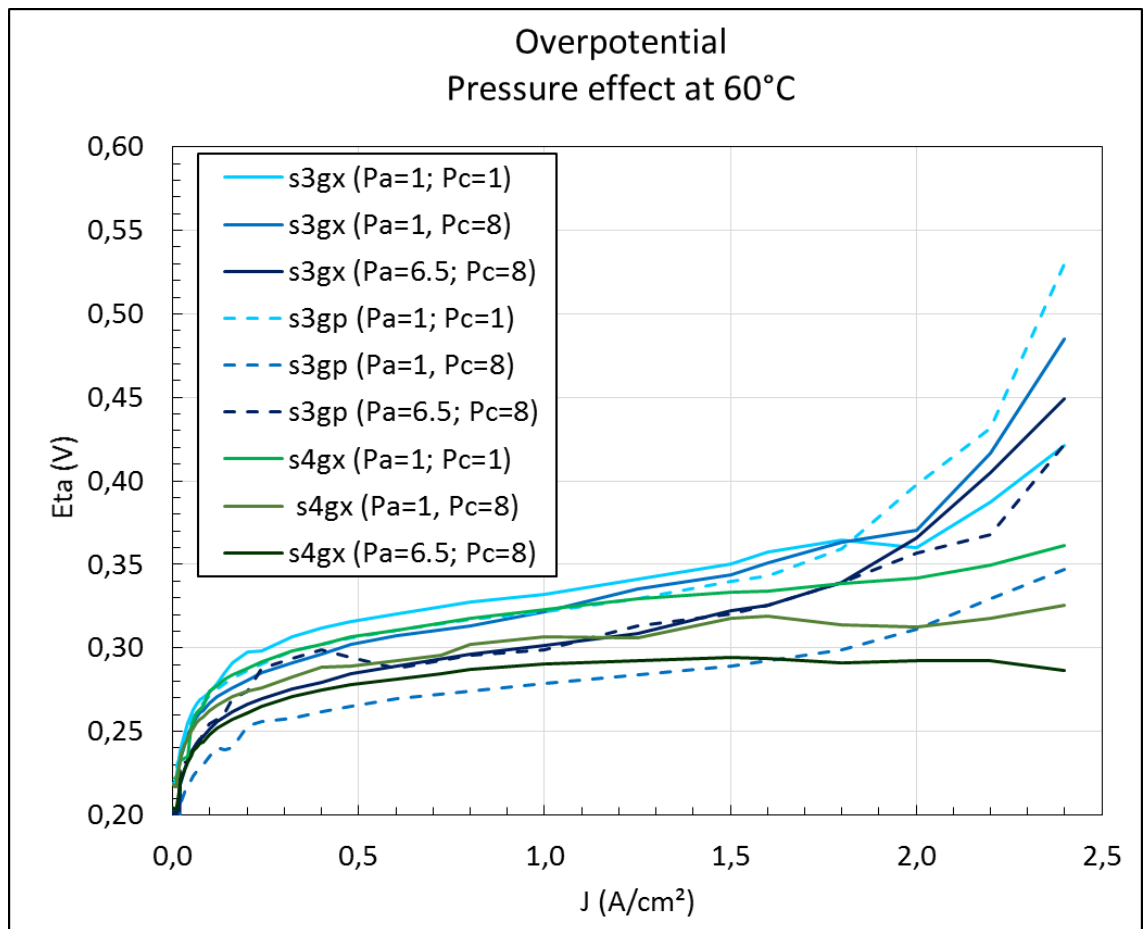


Figure 60: pressure effect on the overpotential at 60°C.

FREE DISTRIBUTION

5. CHANNEL/MESH FLOW MODELLING AND SIMULATION

5.1 *Lab-scale two-phase flow channel model*

The two-phase model developed at local scale for simulating gas-liquid flows inside the anode channels during water electrolysis has been described in deliverable D2.1 (Chandesris, 2015). Results from numerical simulations of a lab-scale setup are shown at two different current densities in Figure 64.

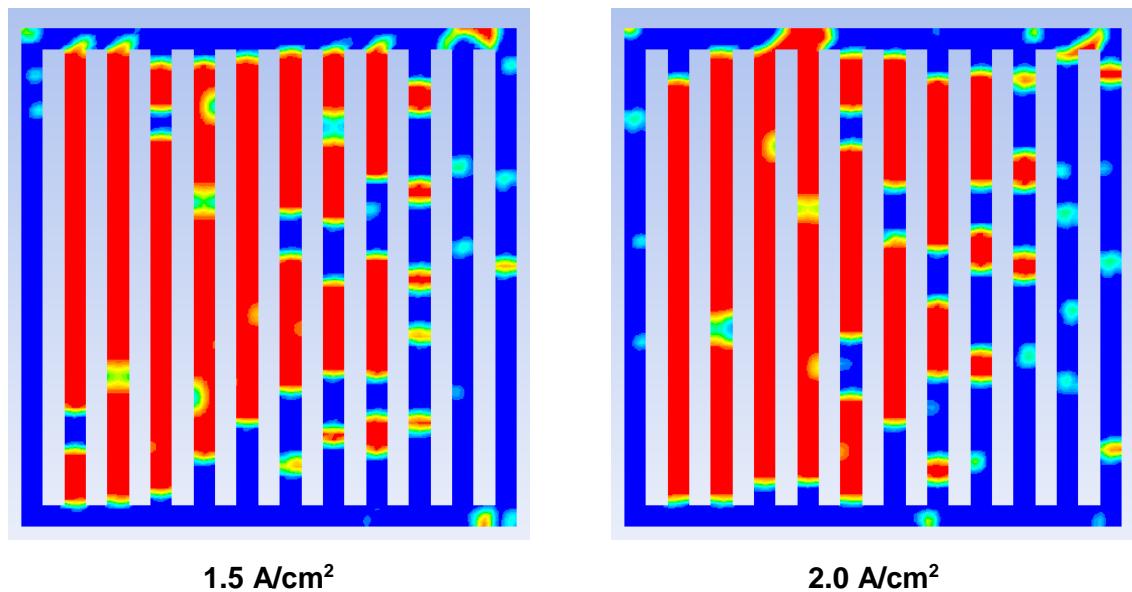
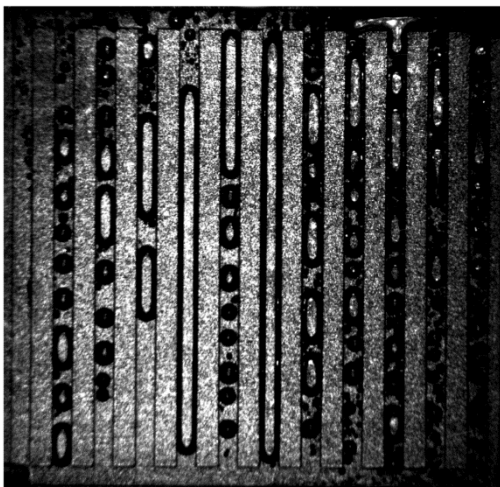


Figure 61: Gas volume fraction.

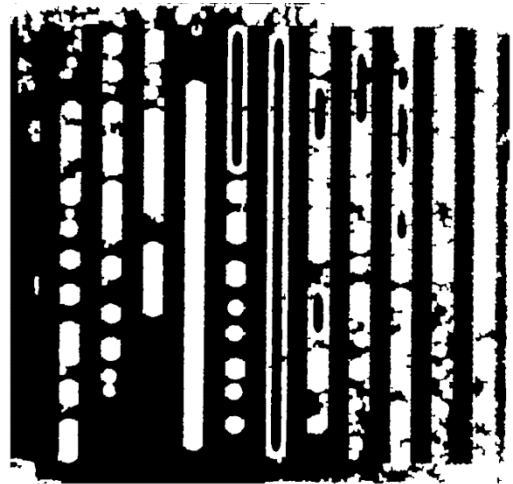
Relevant cold flow experiments have been designed for the purpose of validating this two-phase flow model. High speed camera is used during the experiments. Gas bubbles are supplied evenly through a porous plate at certain flow rates related to actual current densities. Water flowing at the other side of the porous plate comes in contact with the gas resulting in the bubbles moving with the water. The bubbles are captured and analyzed by means of image processing of high resolution camera pictures (see Figure 65). Bubble properties, such as equivalent bubble size, bubble velocity, bubble number, and gas distribution, are then determined using a Digital Image Analysis technique. The results from the numerical simulations are processed in a similar way (see Figure 66 for a comparison).

Comparison of instantaneous snapshots from experiments and simulations highlighted a well distinct spatial partition of the cell between large and small bubbles; large bubbles are located on the left side starting from the second vertical cell channel to cover the whole left side, while the right side is occupied by small and medium size bubbles. This flow structure was found in both experiments and simulations. This dissymmetry has been assigned to the particular design of the experimental cell for which the water is injected and removed not in a symmetrical way (injection is on the bottom left/removal on the top right on the figures).

FREE DISTRIBUTION

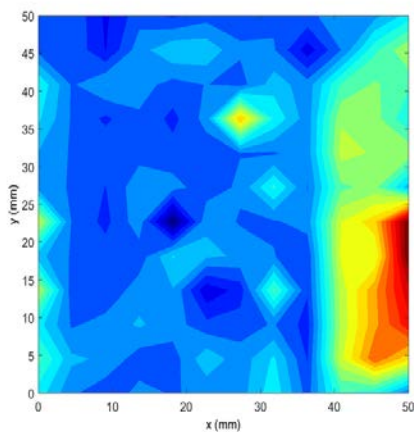


Original image

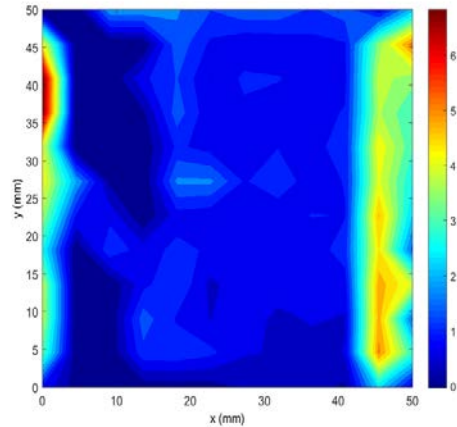


Processed image

Figure 62: Image processing of bubbles from cold flow lab-scale setup.



Experiments



Simulations (middle plane)

Figure 63: Average axial bubble velocity (in mm/s)

A good agreement was found between experiments and simulations for the different bubble properties. It can therefore be concluded, that the model predicts adequately the cold two phase flow in this cell configuration. The population balance model for oxygen bubbles is applied in the simulations with the volume-of-fluid (VOF) concept. Although the grid resolution in the simulation model are fairly coarse the overall flow picture seems to be captured. To get more details in the flow a better resolution of the cell geometry is needed.

This model can be considered as a quasi-3D approach, which can provide reference results regarding the two-phase flow properties. Such information can then be used to build correlations based on the knowledge of two-phase flow structures, to be used in more averaged two-phase flow models such as the one used at cell and stack levels by Fraunhofer and CEA.

FREE DISTRIBUTION

5.2 Cell scale single-phase study

5.2.1 Geometry and grid ITM model description

A geometry and grid model of the mesh part of the anode side of the ITM electrolysis cell with inlet and outlet channels/manifolds has been built in ANSYS Gambit. This comprise one half of the real geometry as the symmetry of the cell is exploited (see Figure 67). The thickness of the mesh region is 1.8 mm. To properly improve on the flow resolution a total of about 478 k grid cells are applied in the computational domain (Figure 68). The vertical resolution is $\Delta z=0.15$ mm in the mesh region. The grid cells are imported to ANSYS Fluent v17 for creating a full numerical model when defining boundary conditions and physical properties for the phases considered.

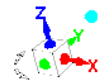
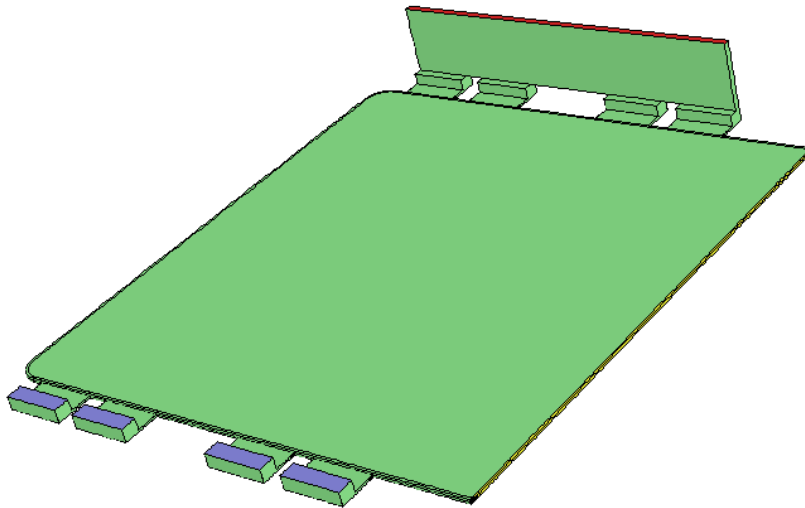


Figure 64: Geometry of mesh in the anode part of the ITM cell configuration with flow inlets and outlets

FREE DISTRIBUTION

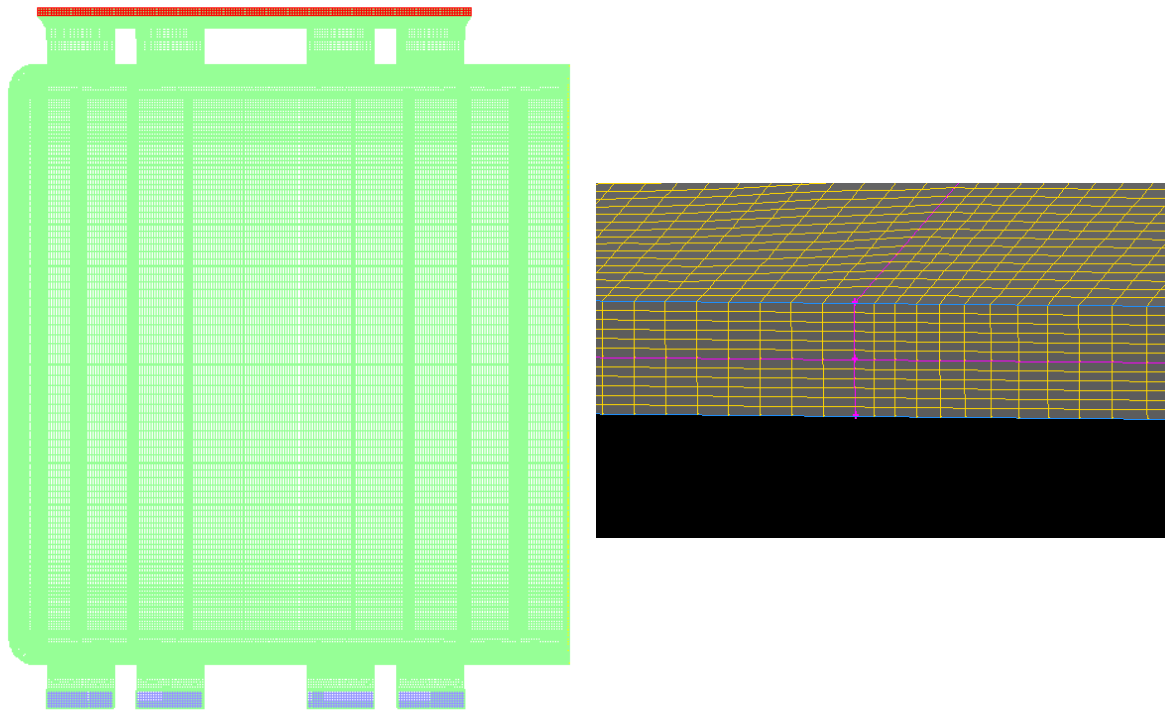


Figure 65: Grid cells applied in the Fluent computational fluid dynamics simulations. Left: Horizontal view, Right: Blow up showing vertical resolution

5.2.2 ITM Mesh configuration

In the computational domain the flow distributor is divided into two porous regions where the inertial/viscous resistances can be defined independently (see Figure 69). The values for inertial and viscous resistances applied in the simulations have been measured by ITM and supplied to the partners.

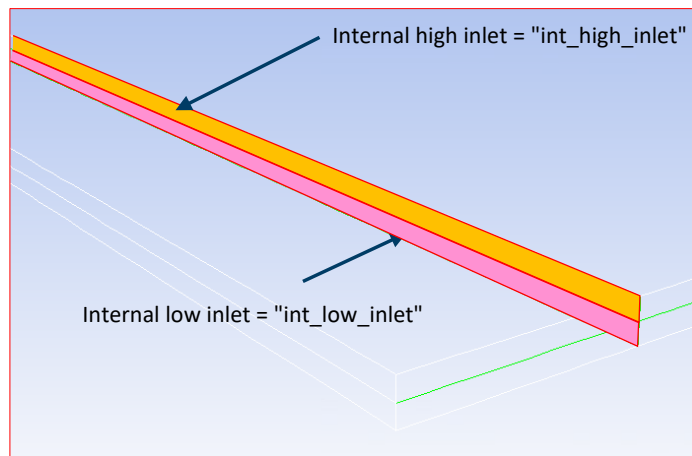


Figure 66: Close up view showing the two layers in the mesh region

FREE DISTRIBUTION

At the inlets water with a constant flow velocity is specified. At the outlet a gauge pressure of zero is applied, while the walls are stationary specified as no-slip.

Different configurations have been simulated to see the effect on the pressure drop through the cell. For specific configurations the pressure drop as function of water flow rate is also presented.

5.2.3 Flow simulation results

We have looked at the pressure drop through the cell when only water is flowing for different configurations of the mesh. The computational fluid dynamic (CFD) simulations are performed in a transient mode although the water flow in this geometry could be regarded as stationary. The next step will be to include the effect of the oxygen bubbles which will be released at the bottom of the model, at the interface between the sinter and the mesh.

Table 23 summarizes the simulation results for different mesh configurations for pressure drop when the water flow rate is 4 l/min. Graphically this is shown in Figure 70.

'Inlet 1' is nearest to the symmetry plane of the cell, while 'Inlet 4' is closest to the side wall. In all of the simulations we see that the pressure drop from 'Inlet 4' to the outlet is higher than the pressure drop from 'Inlet 1' to the outlet. Stdev is a measure of the standard deviation between the pressure drops from the four inlets. The error bars in Figure 70 show \pm Stdev value.

Pressure drop inlet-outlet [Pa]						
Mesh	Inlet 1	Inlet 2	Inlet 3	Inlet 4	Mean	Stdev
L2H1	7104.9	7246.3	7426.7	7474.4	7313.1	170.04
L2H1	7510.4	7653.2	7890.8	7979.6	7758.5	215.30
L2H1	7591.4	7744.2	7979.3	8071.4	7846.6	218.91
L2H1	7855.3	8013.0	8249.0	8341.4	8114.7	221.39
L1H2	7012.6	7153.6	7336.4	7387.7	7222.6	172.32
L1H2	7235.5	7375.9	7615.0	7703.0	7482.3	214.90
L1H2	7279.7	7431.0	7666.7	7758.8	7534.1	218.66
L1H2	7407.0	7560.3	7798.7	7888.8	7663.7	220.22

Table 21: Computed pressure drop for single phase (water) flow through the anode mesh part of the cell

FREE DISTRIBUTION

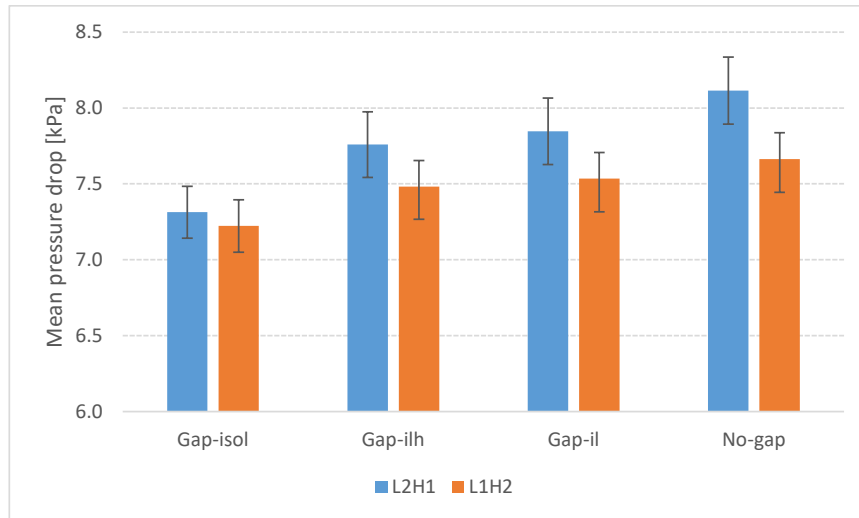


Figure 67: Mean pressure drop from inlet to outlet in anode mesh part of the cell

As seen from Table 22 mesh orientation 1 has lower inertial and viscous resistances in the flow direction. This is reflected in Figure 70 with lower pressure drop for L1H2 compared to L2H1 configurations. These results show also that the pressure drop decreases as the size of the porous mesh region decrease.

In Figure 71 the mean pressure drop is shown as a function of water flow rate for different configurations of the mesh.. It is seen that a flow rate variation in this range has a major impact on the pressure drop.

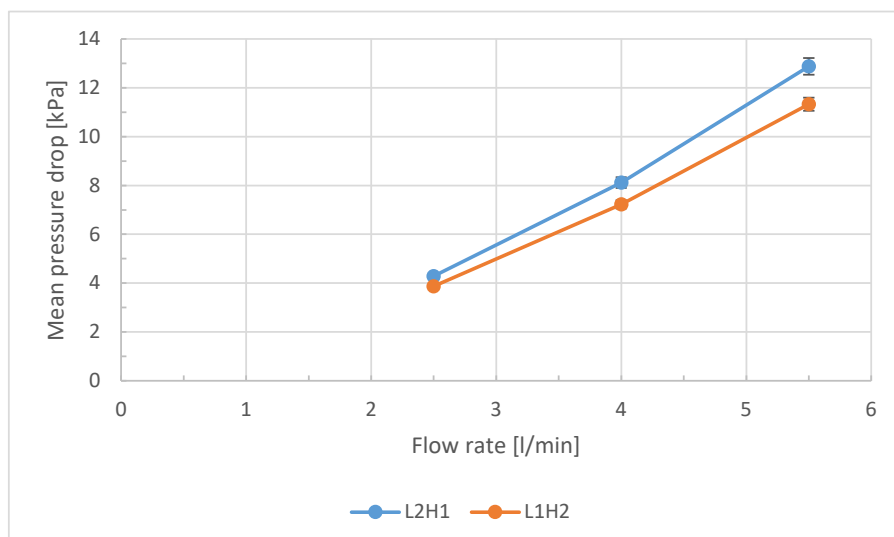


Figure 68: Mean pressure drop as function of water flow rate for different configurations of the mesh

FREE DISTRIBUTION

6. VALIDATION OF THE STACK-SCALE CEA MODEL

6.1 Introduction

The PEMWE stack code developed at CEA aims at simulating large cells or stack describing the multi-physic phenomena that occur in the electrolysis cell using simple laws and coarse meshing (PS++ code (Robin et al., 2015)). The code is fast enough to perform sensitivity calculations that can be used to help in the design process. The stack code has been described in a previous report (D2.1). It is based on bond-graph approach and developed in the Matlab/Simulink platform. It is the receptacle for the elementary models and laws developed by the partners and validated using experimental data or highly accurate simulations that can be considered as numerical experiments.

An illustration of the code interface is given on the Figure 72. It provides some information such as the mass balance of water and gases including the hydrogen production, the energy balance, the state of the membrane and the potential for a given current. The data presented on the interface are not exhaustive: many others can be plotted.

New physical and chemical laws have been developed in the previous sections based on the characterization work performed on ITM's key components. These new laws have been implemented in the PS++ PEMWE stack model and the objective of this section is to validate the behavior of the code when all these different laws are coupled but also to analyze the evolution of the different local quantities computed by the code.

FREE DISTRIBUTION

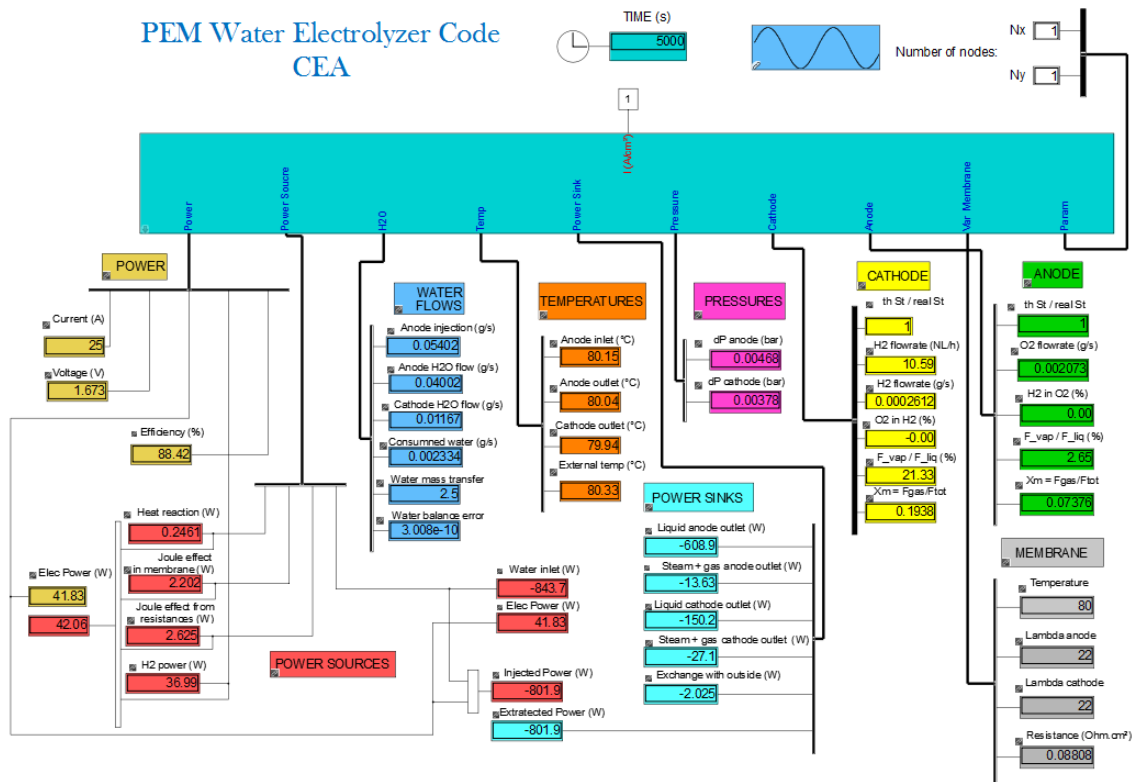


Figure 69: Stack code interface

6.2 Validation against polarization curves

Nine polarization curves have been calculated with the code using a coarse meshing of 1x1 node. They correspond to the 3 temperatures: 40/60/80°C and the 3 geometrical configurations: sinter 3 with parallel and crossed meshes, sinter 4 with crossed meshes. The contact ohmic resistances that are used in these calculations are deduced from the difference between EIS results and the Springer model for membrane resistance. They have been averaged for the 3 temperature EIS measurements.

The comparison between experimental and calculated polarization curves are given on Figure 73. The calculated curves fit quite well the experimental ones. One can notice small differences (less than 15mV) at low density current (lower than 0,5A/cm²) that corresponds to dispersion in the measured resistances and to small deviations obtained in the electrochemical law derivation process. At higher current (above 1.5 or 2 A/cm²), the electrochemical law that does not yet stand for mass transfer limitation, underestimates the potential. This point will be considered later. These first results of the code obtained with only 1 node are quite satisfactory since they give quantitatively good results.

FREE DISTRIBUTION

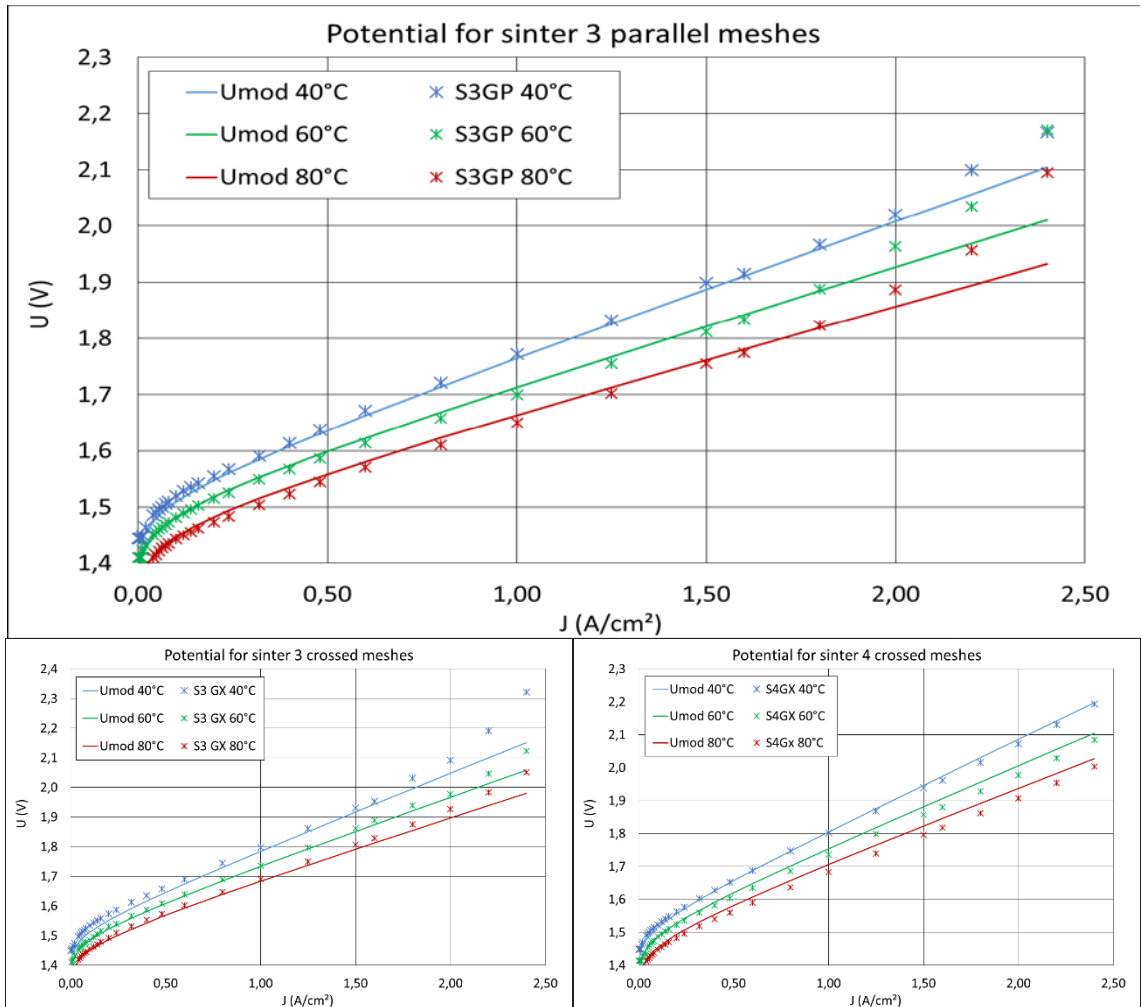


Figure 70: Polarization curves obtained with the code (solid lines) compared to the experimental ones (stars).

6.3 Link between the liquid saturation and the potential

As mentioned in paragraph 4.4.1, the water activity is expected to depend strongly on the liquid saturation (liquid volumetric fraction) in the catalyst layer. The code provides the liquid saturation calculated in the catalyst layer. Thus we have plotted both the potential and the liquid saturation as a function of current density on Figure 74 for the sinters 3 and 4 with crossed meshes at anode. These graphs show that the liquid fraction curves are qualitatively similar for the two sinters but quantitatively different at high current density: the sinter 4 gives lower potential than sinter 3 with lower liquid fraction. The mass transfer limit is reached when using sinter 3 but not when using sinter 4 (until 2.4 A/cm²) while the amount of liquid water available for the reaction is slightly lower with sinter 4 than sinter 3.

Another conclusion of these calculations is the decrease of liquid saturation with the increasing temperature. This is due to the saturation pressure increase with temperature. Liquid and steam being at saturation.

FREE DISTRIBUTION

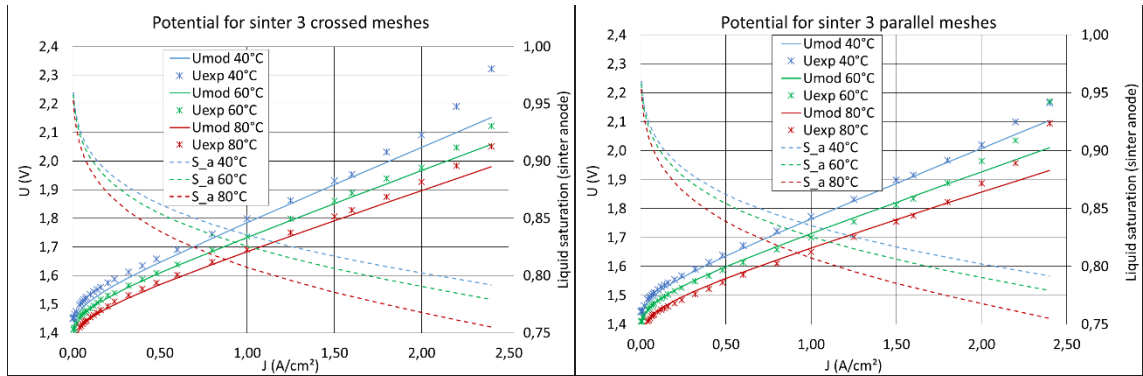


Figure 71: potential (left scale) and liquid fraction (right scale) (calculated at sinter on anode side) function of current density

6.4 Spatial evolutions

The flow model inside the mesh domain is 1D so it is possible to calculate the spatial evolution of the main variable of the electrolyzer such as concentration of species, temperature, pressure...

The CEA cell is discretized using 10 nodes in the mean flow direction along the Y axis (see Figure 75) and 1 node in the perpendicular direction along the X axis.

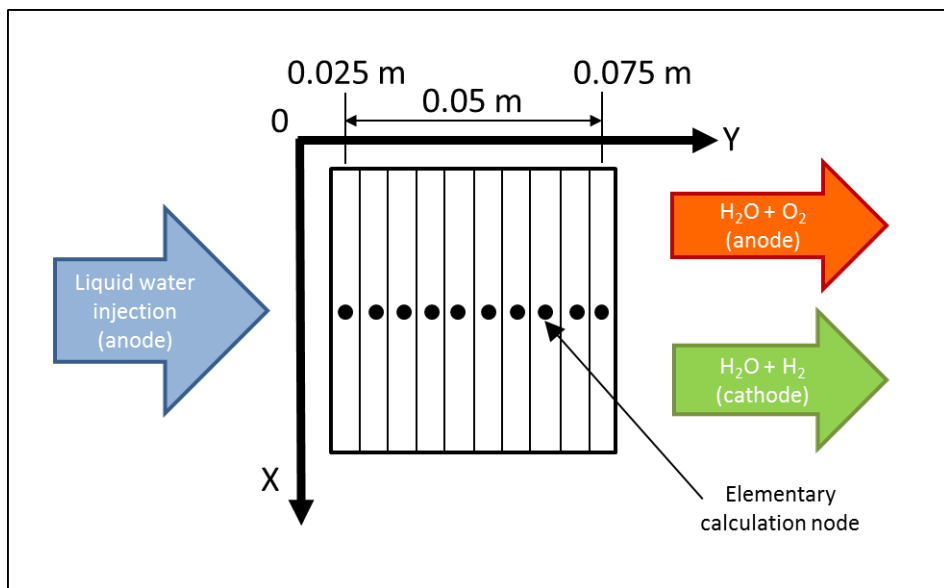


Figure 72: calculation domain.

In the example detailed below, the current density is equal to 2A/cm², the temperature is set to 60°C and the mass flow rate is 200g/h (like in the CEA protocol).

FREE DISTRIBUTION

- The calculation is performed on 5000s for the physical time which is quite enough to reach stationary state as illustrated on Figure 76-a. All the following figures consist in profiles along the Y direction, i.e. the main flow direction in the CEA cell.
- The Figure 76-b give the various contributions to the total potential. Their values are calculated thanks to the ohmic resistance calculation and the electrochemical law described in sections 4.3 and 4.4.
- The pressure gradients along the mean flow direction are given on the Figure 76-c. As expected, head loss makes the pressure decreasing from inlet to outlet.
- The temperature profile in the cell heart and the bipolar plate are given on the Figure 76-d. The internal temperature is imposed, so due to exchange with outside, the bipolar plates have lower temperature.
- The local density current slightly increases from inlet to outlet (Figure 76-e). This linked to the reversible potential decreases (not shown).
- The membrane water content is constant everywhere along the membrane and through the MEA: same value on the anode and cathode sides (Figure 76-f).
- Thus, diffusion through the membrane is negligible and the water flux through the membrane is only due to the electro-osmosis (Figure 76-g).
- The water flux through membrane divided by the consumed water is constant and equal to 5.
- On Figure 76-i, on the anode side, the molar flux of liquid water is of course oriented from mesh to anode. It is relatively important compared to the consumed water, which is also displayed for comparison. Oxygen is flowing from anode to mesh together with a small amount of steam.
- Figure 76-j, hydrogen with a small amount of steam and liquid water are flowing from cathode to the mesh.
- The liquid and gas water are at saturation and thus the liquid evaporates as the pressure decreases making the molar concentrations of steam increase along the Y axis as illustrated on Figure 76-k.
- The liquid fractions decrease going downstream (consumption-l). These decreases are small in the electrodes but very important in the anode mesh due to the consumption and the electro-osmosis.
- Due to the steam molar fractions increase, the hydrogen and oxygen molar fractions decrease along the cathode and anode meshes (consumption-m).
- But effectively the number of hydrogen and oxygen moles increase going downstream (consumption-n).

FREE DISTRIBUTION

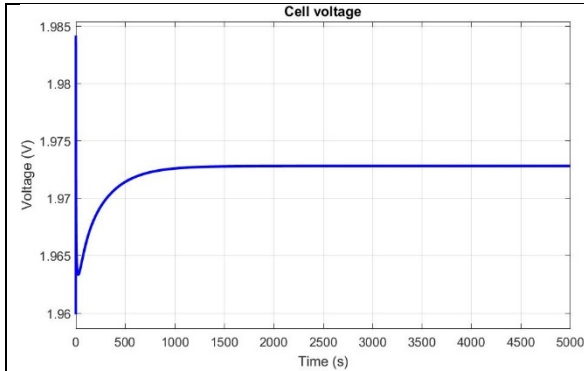


Figure 76-a: temporal evolution of the potential

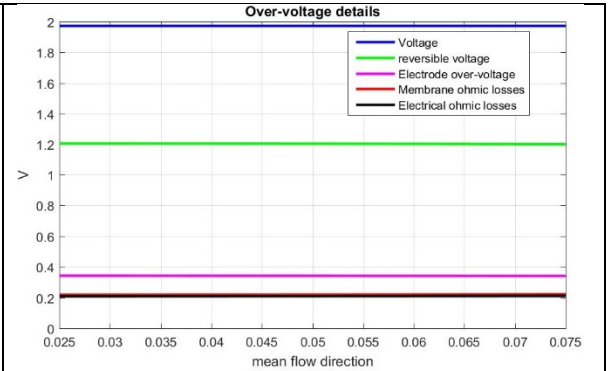


Figure 76-b: the various contributions to the potential

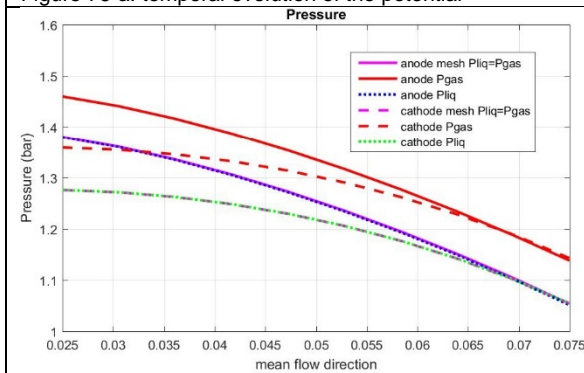


Figure 76-c: Pressure evolution along the Y axis in the meshes and the electrodes on both sides.

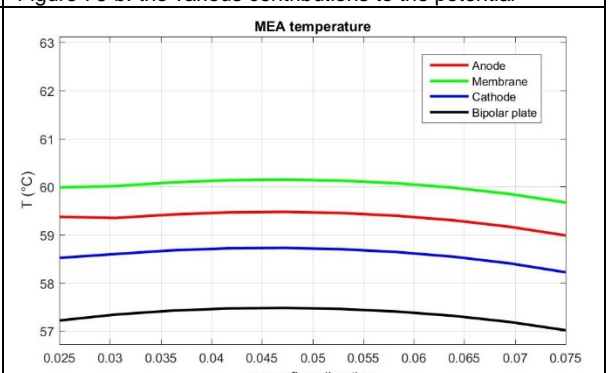


Figure 76-d: Temperature profiles.

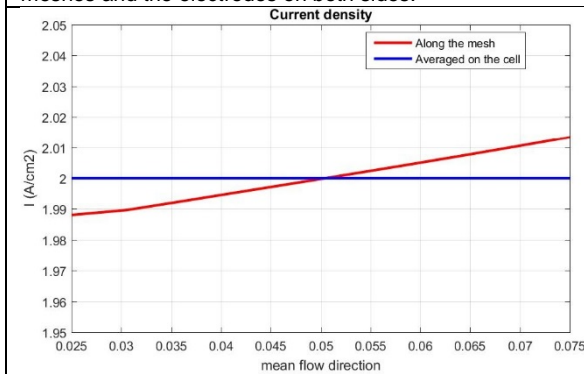


Figure 76-e: current density

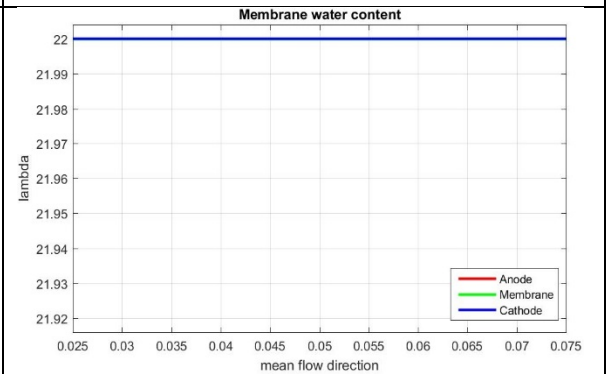


Figure 76-f: Membrane water content

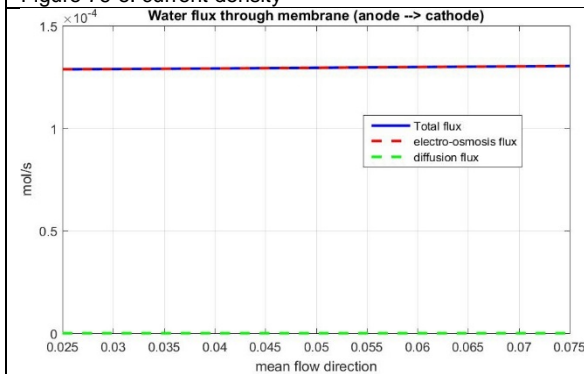


Figure 76-g: water flux through membrane

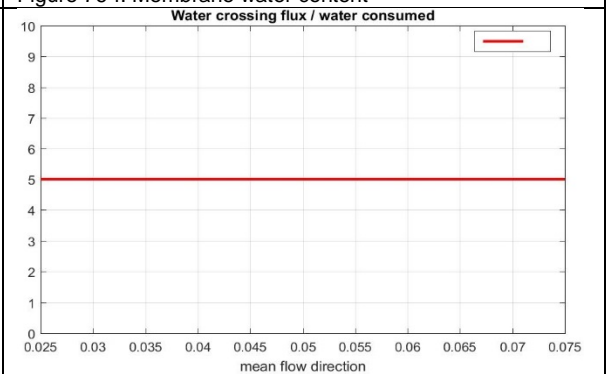


Figure 76-h: water crossing flux / water consumed.

FREE DISTRIBUTION

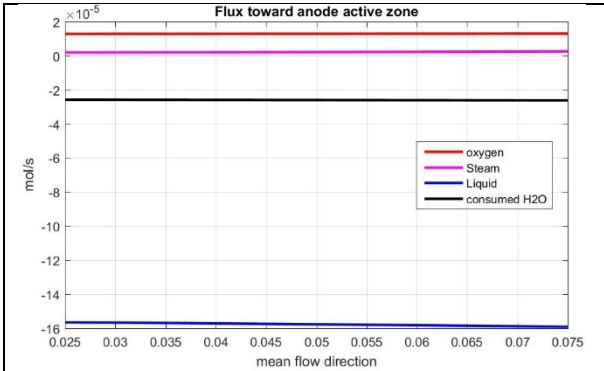


Figure 76-i: molar flux through the sinter (<0 when oriented from mesh to the anode)

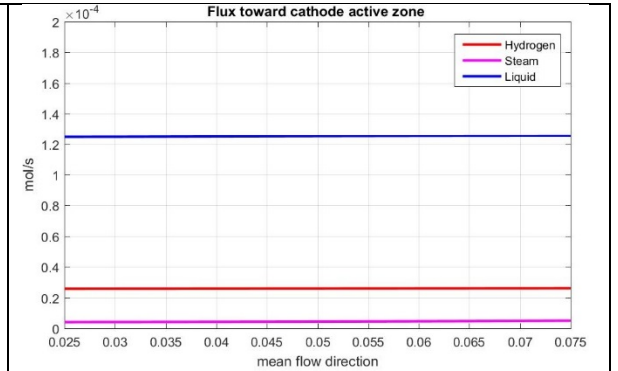


Figure 76-j: molar flux through the sinter (>0 when oriented from cathode to the mesh)

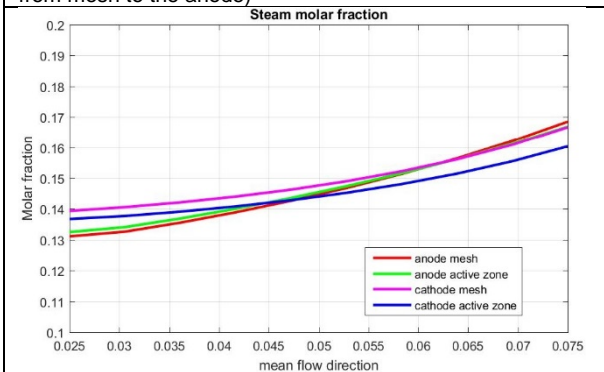


Figure 76-k: steam concentration profiles

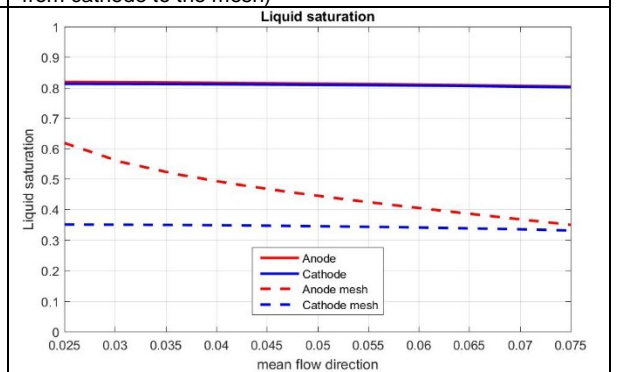


Figure 76-l: spatial evolution of liquid saturation (fraction)

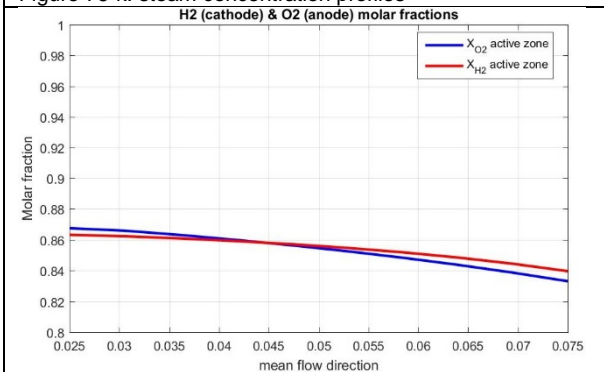


Figure 76-m: oxygen molar fraction profile in the anode and hydrogen molar fraction profile in the cathode.

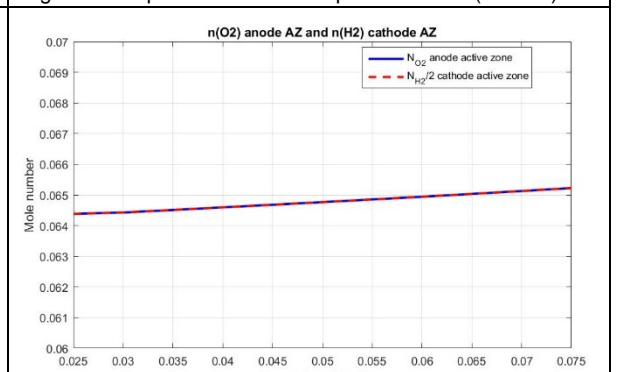


Figure 76-n: profile of number of moles along the electrodes

Figure 73: spatial evolution of mean variables along the mean flow direction (Y axis)

FREE DISTRIBUTION

7. CONCLUSION

ITM has provided cell components (MEA, meshes, sinters) to CEA, FRAUNHOFER and SINTEF which have characterized their properties and used them in small single cells to study their behavior in laboratory conditions. The obtained results have been used both to analyze the cell performances depending on the operating conditions and components properties and to develop physical and electrochemical models to be used in the simulation codes developed by the partners.

The electrical resistances of the flow distributors (mesh) and the porous transport layer (PTL) (sinter) have been measured as function of the clamping pressure by CEA, FRAUNHOFER and SINTEF, providing coherent values. Mesh and PTL bulk resistances are negligible compared to contact resistances. Soft contact resistances (PTL against MPL and/or GDL) dominates hard contact resistances. Coating of the PTL also influences the PTL contact resistances at beginning of life, and its evolution during aging is currently studied in another work package. The order of magnitude of this total contact resistance is found to be around $100\text{m}\Omega\cdot\text{cm}^2$ which is a not negligible contribution to the total ohmic resistance: around 55% at 80°C and 40% at 40°C . Decreasing this contribution would clearly increase the cell performances.

The geometrical properties of the meshes and the sinters microstructures have been studied using various complementary techniques. The knowledge of these geometrical properties can be related to the flow properties of these two components which have also been characterized. As already reported in the literature, the pore sizes inside the sinter have a direct impact on both the capillary pressure and the permeability. This dependency has been here determined for microstructures typical of PTL used in PEMWE. Information regarding the dependence of these properties to the microstructure is capital, especially when the cell is running at high current density, because these two properties characterize the capability of the PTL to provide enough liquid water to the reactive zone on the anode side. Capillary and permeability laws have been determined from this characterization work and have then be used as input parameters in the simulation codes.

ITM key components have then be studied in-situ in small single cells in the different institutes. The cell performances have been characterized using both polarization curves and electrochemical impedance spectra for various temperatures, pressures and anode inlet water flow rate. Different cells configuration have been studied to analyze the impact of the sinter and of the meshes. These results provide information about the variation of performances depending both on the operating conditions (temperature, pressure, inlet water flow rate) and on the cell components: relative position of the meshes and sinter structure. Without considering the aging effect, the tendencies are the following. Increasing the temperature increases the cell performance, as well known in the literature. The effect of increasing pressure, which is to slightly increase the cell potential but also to reduce the overpotential induced by mass transfer limitation at high current, is also recovered. More interestingly, we

FREE DISTRIBUTION

were able to analyze the impact of two sinters with different microstructures. Sinter 3 with larger pores leads to better performances at low current densities than sinter 4 (with smaller pores), but the mass transfer limitation is reached for moderate current densities (around 2 A/cm²) while this limit is shifted to higher current densities for sinter 4 (at least above 2.4 A/cm²). These results have also been used to develop and validate a semi-empirical electrochemical law that is used in the system code.

Two-phase flow simulations inside an anodic channel geometry have been performed at SINTEF and successfully validated against experimental data obtained using visualizations techniques. However, this simulation work in “open” geometry cannot be directly transposed to the new anodic mesh geometry proposed by ITM in the course of the project, which is porous. Nevertheless, CFD single-phase flow simulations have been performed on the real ITM distributor design for various meshes configurations. The obtained results allows to discriminate between different ITM's design strategy and can also be used as reference results for the validation of the pressure drop of the coarser multi-physics codes.

The properties of ITM's key components have now been implemented in the stack code developed by CEA (PS++ code) and the code has been validated successfully against experimental results obtained at single-cell level. The code provides information on the physical properties in the different components such as the flow in the meshes, the sinter and also the water flux through the membrane, the electrochemical response to a given current and to the internal flows. This code allows to analyze the effect of several parameters on the PEMWE performance including the geometry and the operating conditions. It will be used to perform sensitivity studies to these various parameters at the MW stack scale.

FREE DISTRIBUTION

8. NOMENCLATURE

Acronyms

GDL: Gas Diffusion Layer
 MEA: Membrane Electrode Assembly
 MPL: Micro-Porous Layer

Symbols

A: channel section (m^2)
 A_0 : activation energy (J/mol)
 a: activity (-)
 a_{eo} : electro-osmotic drag coefficient (-)
 C_f : pressure drop coefficient (-)
 D_H : hydraulic diameter (m)
 D_λ : diffusion coefficient in the membrane (-)
 E_{rev} : reversible potential (V)
 EW: membrane equivalent weight (kg)
 e: thickness (m)
 F: Faraday constant ($C \cdot mol^{-1}$)
 i_0 : exchange current density (A/m^2)
 J: current density (A/m^2)
 k_0 : rate parameters per unit surface of the reactions ($mol/K/s/m^2$)
 K: permeability (m^2)
 L: length (m)
 n: number of electron involved in a reaction
 P_j : partial pressure for the j species (Pa)
 P_c : capillary pressure (bar)
 ΔP : pressure difference (Pa)
 P_w : wetted perimeter (m)
 R: perfect gas constant (J/K/mol)
 Re: Reynolds number (-)
 R_i : resistance of the element i (Ω)
 R_m : membrane resistance ($\Omega \cdot m^2$)
 R_Ω : ohmic resistance ($\Omega \cdot m^2$)
 R_p : pores radius (m)
 S: electrode surface (m^2)
 ΔS : entropy variation (J/K)
 s: liquid water fraction (-)
 T: temperature (K)
 U: cell potential (V)
 V: velocities (m/s)

θ : contact angle (rad)

ρ_{sec} : density of the membrane in a dry state ($kg \cdot m^{-3}$)

σ : conductivity (S/m)

Subscripts

a: anode
 c: cathode
 C: contact
 m: membrane
 M: mesh
 S: sinter
 vap: vaporization

Greek letters

α : charge transfer coefficient
 β : semi-empirical electrochemical reaction coefficients (-)
 ε : porosity (-)
 γ : surface tension (N/m)
 γ_A, γ_C : rugosity factors (-)
 λ : water content inside the membrane (-)
 μ : dynamic viscosity (Pa.s).
 η : over potential (V)
 ρ : density ($kg \cdot m^{-3}$)

9. REFERENCES

- Chandesris M, Serre G., Bai W., Bromberger, K. and Ojong, E. M. 2015. Technical Report RT/DEHT/2015/026, "D2.1 Coupling and up-scaling strategies for the development of multi-scale and multi-physic PEMWE performance models".
- Robin, C., Gerard, M., d Arbigny, J., Schott, P., Jabbour, L., Bultel, Y., 2015. Development and experimental validation of a PEM fuel cell 2D-model to study heterogeneities effects along large-area cell surface. *Int. J. Hydrogen Energy* 40, 10211–10230.
- Serre G., 2016, Technical Report RT/DEHT/2016-007, "PEM Water Electrolysis, project MEGASTACK - D2.2 PEMWE model".
- Springer T.E., Zawodzinski T.A., Wilson M.S., Gottesfeld S., 1996. Characterization of Polymer Electrolyte Fuel Cells Using AC Impedance Spectroscopy. *Journal of The Electrochemical Society* 143, 587–599.
- Washburn E. W., 1921, The Dynamics of Capillary Flow, *Physical Review* 17 (3): 273
- Zawodzinski T.A., Davey J., Valerio J., Gottesfeld S., 1995. The water content dependence of electro-osmotic drag in proton-conducting polymer electrolytes. *Electrochimica Acta* 40, 297–302.
- Zawodzinski T.A., Neeman M., Sillerud L.O., Gottesfeld S., 1991. Determination of water diffusion coefficients in perfluorosulfonate ionomeric membranes. *J. Phys. Chem.* 95, 6040–6044.

FREE DISTRIBUTION

APPENDICES

10. APPENDIX: LINK BETWEEN PERMEABILITY AND HYDRAULIC DIAMETER

The Poiseuil law for laminar flow head loss writes:

$$\frac{\Delta P}{L} = \frac{1}{2} C_f \frac{\rho V^2}{D_H}$$

$$C_f = \frac{64}{Re} : \text{for laminar flow, } Re < 2000$$

$$Re = \rho \frac{V D_H}{\mu}$$

The Darcy law writes:

$$\frac{\Delta P}{L} = \frac{\mu}{K} V$$

Assuming these two laws give the same pressure gradient in laminar flow, we obtain a relationship between the permeability and the head loss coefficient:

$$\frac{1}{2} C_f \frac{\rho V^2}{D_H} = \frac{\mu}{K} V$$

Thus we obtain an *estimation* of the permeability:

$$K = \frac{D_H^2}{32}$$

The hydraulic diameter is calculated thanks to the following formula: $D_H = 4 \frac{A}{P_w}$